Electrochemical prototype reactions in 2D confined space

Surface-specific molecular insights

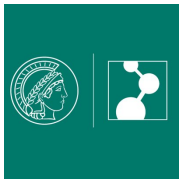

Daniel Ohm
geboren in Rüdesheim am Rhein

Dissertation zur Erlangung des Grades eines
'Doctor rerum naturalium (Dr. rer. nat.)'
des Fachbereichs
09 - Chemie, Pharmazie, Geographie und Geowissenschaften
der Johannes Gutenberg-Universitaet Mainz

Max Planck Institute for Polymer Research

Mainz, March 2023

1. Gutachterin:
2. Gutachter:
Tag der muendlichen Pruefung: 23.06.2023

Abstract:

The development of new catalysts with special attention to the optimization of mass activity for the ecological and economical production of efficient electrocatalysts requires detailed research in the field of two-dimensionally confined catalysts. Reducing expensive and rare catalyst materials while preserving the catalytic activity is one of the challenges whose solution can contribute to the transition from fossil fuels to renewable energy. However, the improvement of existing catalysts requires fundamental research in the field of confinement of catalytically active substructures to understand how the reduction of catalyst metal by confinement to nanostructures affects the activity of the catalyst. In addition, mechanisms leading to the loss of catalytic activity need to be elucidated and understood in order to avoid them in energy conversion processes.

In this PhD thesis, the preparation of a bimetallic 2D nano-confined catalyst with islands of a platinum group metal (PGM) on a Au surface is presented and investigated as a catalyst system for the prototype electrochemical reactions hydrogen evolution reaction (HER) and formic acid oxidation (FAO). It is shown that the restriction of PGM to nanoislands has an impact on the catalytic activity with respect to HER, and optimization of the island parameters size and distribution by changing the parameters during the fabrication of the islands via Cu underpotential deposition allows optimization of the activity. Furthermore, the results show that, with respect to the catalytic activity, an optimal island size of 13 nm with an island spacing of 5 nm exists.

By the use of electrochemical methods, we demonstrate that a mechanism leading to the poisoning of the catalyst during FAO cannot be neglected and, using tip-enhanced Raman spectroscopy (EC-TERS), we can identify the poisoning species as CO, which is formed intermediately during FAO. We demonstrate that avoiding the (partial) oxidation of the Pd-based catalyst used in this study is essential for the effective operation of Pd based direct formic acid fuel cells, since the oxidation of Pd promotes the formation of CO as an intermediate during FAO.

Using electrochemical fluorescence microscopy (EC-FM), we confirm the assumption that protons can accumulate at the interface between an electrode and the electrolyte despite a bulk alkaline solution. We demonstrate the detection of the pH-dependent fluorescence signal of a dye by protonation at the surface of the electrode with applied potential. This measurement is used to calculate an effective surface pH, which is in the acidic range despite alkaline solution when the electrode potential is low enough.

Zusammenfassung:

Die Entwicklung neuer Katalysatoren mit besonderem Augenmerk auf die Optimierung der Massenaktivität zur ökologischen und ökonomischen Herstellung effizienter Elektrokatalysatoren erfordert detaillierte Forschung auf dem Gebiet der zweidimensional beschränkten Katalysatoren. Die Reduktion teurer und seltener Katalysatormaterialien unter Erhalt der katalytischen Aktivität ist eine der Herausforderungen, deren Lösung zum Wandel von fossilen Brennstoffen hin zu erneuerbaren Energien beitragen kann. Dafür ist jedoch grundlegende Forschung im Bereich der Beschränkung der katalytisch aktiven Teilstrukturen notwendig, um zu verstehen, wie sich die Reduktion des Katalysatormetalls durch Beschränkung in Nanostrukturen auf die Aktivität des Katalysators auswirkt. Außerdem müssen Mechanismen, welche zum Verlust der katalytischen Aktivität führen, aufgeklärt und verstanden werden, um diese in Energieumwandlungsprozessen zu vermeiden.

In der vorliegenden Doktorarbeit wird die Darstellung eines bimetallischen 2D nanobeschränkten Katalysators mit Inseln eines Platingruppenmetalls (PGM) auf einer Goldoberfläche präsentiert und als Katalysatorsystem für die elektrochemischen Prototypreaktionen Wasserstoffentwicklungsreaktion (HER) und Ameisensäureoxidation (FAO) untersucht. Es wird gezeigt, dass die Beschränkung der PGM auf Nanoinseln Einfluss auf die katalytische Aktivität bezüglich der HER hat und eine Optimierung der Inselparameter Größe und Verteilung durch Änderung der Parameter während der Herstellung der Inseln via Cu Unterpotentialabscheidung eine Optimierung der Aktivität erlaubt. Des Weiteren zeigen die Ergebnisse, dass eine, im Bezug auf die katalytische Aktivität, optimale Inselgröße von 13 nm mit einem Inselabstand von 5 nm existiert.

Weiterhin zeigen wir mittels elektrochemischer Methoden auf, dass ein Mechanismus, welcher zur Vergiftung des Katalysators während der FAO führt, nicht vernachlässigt werden kann und können mit Hilfe von spitzenverstaerkter Raman Spektroskopie (EC-TERS) die vergiftende Spezies als CO, welches intermediär während der FAO entsteht, identifizieren. Wir zeigen auf, dass eine Vermeidung der (teilweisen) Oxidation des verwendeten Pd basierten Katalysators essentiell für den effektiven Betrieb von direkten Ameisensäure Brennstoffzellen ist, da die Oxidation des Pd die Bildung von CO als Zwischenprodukt der FAO begünstigt.

Mit Hilfe von elektrochemischer Fluoreszenzmikroskopie (EC-FM) zeigen wir eine Bestätigung der Annahme, dass sich Protonen an der Grenzfläche zwischen einer Elektrode und dem Elektrolyten trotz einer alkalischen Lösung ansammeln können. Wir demonstrieren die Detektion des pH abhängigen Fluoreszenzsignals eines Farbstoffs durch Protonierung an der Oberfläche der Elektrode bei angelegtem Potential. Diese Messung wird genutzt, um einen effektiven Oberflächen pH zu berechnen, welcher trotz alkalischer Lösung im sauren Bereich liegt, wenn das Elektrodenpotential niedrig genug ist.

Contents

Part I

Introduction

1

Background and Motivation

The first chapter introduces the concept of catalysis and surface specific reactions.

Contents

1.1 Introduction

The generation of mankind living at this decade faces a continuously growing problem of increasing energy consumption world wide, that is, at present, mostly secured by energy generation out of fossil fuels. Not only the run out of fossil fuels that can easily be mined will become a future problem but also the impact on the environment is huge and leads to further problems. The limited availability of fossil fuels and, moreover, the strongly uneven distribution of such fossil fuels and the resulting dependency on fossil fuel mining states has the potential for conflicts, either political or economical. Also, the demand for climate neutral energy resources is rising in the face of the climate change debate and rising sea levels as result of global warming. All these discussions show the need and high demand for 'green' and renewable energy conversion methods to solve at least part of the problems.

The field of electrochemistry could play a huge role in finding a solution for the transition to a green economy. One concept to increase the role of renewable energy sources is the electrocatalytic water splitting and formation of molecular hydrogen as energy carrier. Not only fossil fuels are unevenly distributed all over the world, but also the sun does not shine equally everywhere, neither does the wind blow equally strong all over the planet. This leads to the rise of another the challenge: The energy can not always be generated where it is needed. The capacity for energy conversion by use of the sun or wind to satisfy the growing need of energy can be reached, but the transport of the energy to where it is needed is a big problem. By electrochemical water splitting to molecular hydrogen in electrolyzers at places with huge availability of renewable energy sources, this problem could be solved. Molecular hydrogen, as a gas, can be compressed and transported without major losses and can be converted to electrical energy everywhere it is needed by the use of fuel cells.
Both critical devices in this concept, the electrolyzer that transform electrical to chemical energy, and the fuel cells, that retransform the chemical energy to electricity, make use of electrocatalytic materials to improve the outcome of the devices in terms of efficiency. The electrocatalyst lead to a lowering of the energy barrier of the given reaction (by a change in the reaction pathway) and thus speed up the reaction and increase the activity and efficiency of the device. Current research in the field of electrochemistry therefor aims to improving electrocatalysts to make electrochemical energy conversion a real possible solution for the power supply problems in the world.

The demands on new catalytic materials are widespread. The material needs to allow for highest specific activity for an electrochemical reaction and high stability but should be as cheap as possible and preferably available in huge amounts. The rational design

of electrocatalysts is challenging and introduces a new field of research, focusing on the surface properties of materials and the related electrochemical properties. The improvement of established electrocatalysts requires knowledge about reactive surface sites, reaction intermediates and also the exact knowledge about the conditions in the working cell.
Reactive surface sites, most often defect sites such as kink sites, step-edges, adatoms or even larger structures like islands, are of different natures and the detection of the most active defect sites requires tools that allow for surface sensitive detection of reaction intermediates with chemical specificity and high spatial resolution.[Ban+14] The mechanistic understanding of reactions together with the knowledge about the most active sites of a catalytic material for possibly different pathways, including different reaction intermediates, can provide possibilities to improve existing electrocatalysts.[Mis+16]

The general understanding of the nature of a catalyst surface can be provided by scanning probe microscopy techniques such as scanning tunneling microscopy (STM), combined with electrochemical (EC) control. While electrochemical techniques like cyclic voltammetry (CV) provide information averaged over the whole exposed catalyst surface, STM gives information about the surface structure with high spatial resolution. In the combination of the techniques, direct information about the quality of the electrocatalyst for a given electrochemical reaction can be obtained and related to its surface structure. For a tune able system this allows for adjusting of the catalyst properties to maximize the activity of the system. However, this technique does not provide any chemical information specifically for different surface sites, so that the reaction mechanism can not be part of the considerations for design adjustments.
Spectroscopic techniques such as Raman and infrared (IR) spectroscopy can provide the chemical information that are needed to identify reaction products and intermediates and gain mechanistic insights into an electrocatalytic reaction. One key technique to provide such information with high spatial resolution and surface specificy is EC tip-enhanced Raman spectroscopy (EC-TERS), a technique that was first shown under ambient conditions in the early 2000s[And00; Hay+00] and later improved to be used under operando conditions.[Zen+15; KMV15; Mar+17] The first works on operando EC-TERS could already show the outstanding capabilities of the method to show the chemical behavior on the molecular level under electrochemical control. Later, the direct correlation between surface chemistry and surface topography was shown in EC-TERS mapping experiments of the electrooxidation of Au surfaces.[Pfi+19; Pfi19]

Besides direct reaction related considerations like mechanism, reaction pathways and reactive sites, the conditions within the electrochemical cell need to be matter of the efforts to improve existing electrocatalysts. One key property that has influence on electrocatalytic reaction is the pH. The effect of the electrolyte pH on the reaction pathway and kinetics of reactions used in fuel cells is subject of many studies. Methanol

and ethanol oxidation reactions show an increase of current density with a change from acidic to alkaline pH.[Bay+10; Tri+02] In case of the hydrogen evolution reaction (HER), the pH dependence of the reaction has influence on the energy level of hydrogen adsorption to the metal electrode, the proton source, i.e. H_3O^+ and H_2O in acidic and alkaline media, respectively, and the specific adsorption of ions from the electrolyte, such as hydroxide ions.[Mar+96; GMR95; TK13] However, the studies focus on the bulk pH of the electrolyte solution and do not include the effect of changes in the local surface pH of the electrode. More recent studies however have recognized the effect of changes in the local surface pH and its influence in the electrocatalytic reduction of CO_2 reduction[GGM06; Rac+18; Sin+16]. Also, microkinetic models recently incorporated the effects of local pH changes in the description of hydrogen and oxygen involving electrochemical reactions.[Mar18]

1.2 Thesis outline

The aim of this thesis is to highlight methods to gain insight into the electrode surface related properties that have great influence on the outcome of an electrochemical cell.

In chapter 3 we show the tunability of platinum group metal (PGM) islands on a Au subsurface and investigate the influence of the island parameters, such as island distribution and island size, on the activity of the catalyst for HER. The methods that were used in this study are (EC-)STM and electrochemical methods such as CV. We make use of the highly controllable copper underpotential deposition (Cu UPD) to control the island parameters. The effect of the island size and distribution on the HER is studied in terms of mass activity of the PGM catalyst, the effect of the number of rim sites and the spacing between the islands.

Chapter 4 has focus on the electrochemical oxidation of formic acid (FAO) as model system for the catalyst developed in chapter 3. Unlike many studies, that conclude the absence of significant poisoning of bulk Pd electrodes in FAO, we found severe loss in activity of our Pd island catalyst during FAO. The chemical nature of this poisoning is studied with the use of EC-TERS, a method that is perfectly suited to obtain insight into the nature of long-live reaction intermediates by providing chemical information correlated with the surface topography with superior spatial resolution.

In chapter 5 we introduce a new technique that has the potential to direct measure the local surface pH of an electrode as function of the applied potential. We combine cyclic voltammetry and fluorescence microscopy to measure the potential dependent

response of a pH sensitive dye in a system at equilibrium and out of equilibrium during HER.

Part II

Fundamentals and Techniques

2

Fundamentals and Techniques

The chapter introduces theoretical fundamentals about the techniques used in the work that is described in this thesis

Contents

2.1 Fundamentals

2.1.1 Thermodynamics in Electrochemistry

The electrochemical equilibrium can be quantitatively described by thermodynamics. The electrochemical equilibrium, which is formed directly when two electrodes are immersed in solution that contains conducting species, is characterized by the open circuit potential (OCP). At the electrochemical equilibrium, the electrochemical potentials $\tilde{\mu}_{sol}$ at the solid interface and $\tilde{\mu}_{liq}$ at the liquid interface are equal. The electrochemical potential $\tilde{\mu}$ can be written as:

$$\tilde{\mu} = \mu_0 + RT \cdot ln(a) + nF\varphi \tag{2.1}$$

The electrochemical potential is a function of the standard chemical potential μ_0. R is the gas constant, T is the temperature, a is the activity, n is the number of moles of the considered component, F is the Faraday constant and φ is the electrostatic potential. The electrochemical potential can be divided into a chemical potential term, $\mu = \mu_0 + RT \cdot ln(a)$ and an electrostatic potential term $nF\varphi$. The chemical potential term describes the chemical interactions between molecular species while the electrostatic potential term originates from the electrostatic interactions between the considered molecules. Considering the electrochemical equilibrium condition, the Nernst equation, a fundamental equation of electrochemistry, can be derived. The Nernst equation describes the relationship between the equilibrium potential of the electrode and the concentration of the reactants involved at a given temperature. From the Nernst equation it can be read that a change in the electrode potential causes a change in the equilibrium concentrations of the species involved, which is satisfied by concentration changes at the electrochemical double layer (EDL) associated with the flow of electrical charge. The general form of the Nernst equation can be written as:[BF01]

$$E_{eq} = E_0^{'} + \frac{RT}{nF} \cdot ln(\prod (C_i)^{v_i}) \tag{2.2}$$

The equation allows the usage of concentrations C_i rather than activities of the involved species, that are most often unknown. The activity coefficient is incorporated in the formal potential $E_0^{'}$. v_i is the stoichometric coefficient of substance i.

2.1.2 Kinetics in Electrochemistry

In the previous section, a system in the equilibrium state was cosidered. In the following, we willl take a closer look at an electrochemical cell in which a reaction takes place and thus an electrical current flows. An electrochemical reaction is, besides others, characterized by the reaction rate, i.e. how fast the reactants are transformed. The reaction rate is composed of several substeps, which all run on their own timescales. Different reaction steps for an electrochemical reaction are shown schematically in figure 2.1.[NCL19].

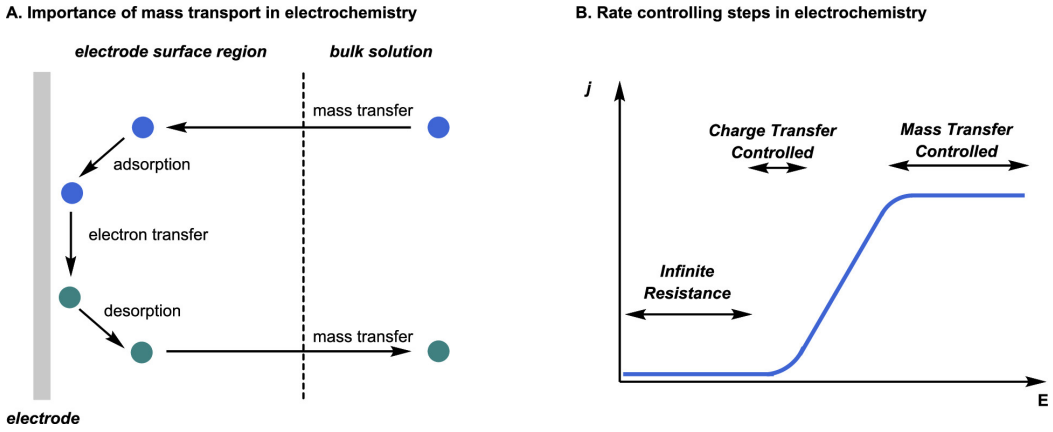

Figure 2.1.: Schematic representation of the steps of electrochemical reactions (A) and the current resulting as function of the applied potential in the charge-transfer and mass transport controlled regimes. Image reprinted from [NCL19] under CC license (CC-BY-NC-ND)

.

The steps involve the mass transport of reactants to and from the electrode, the ad-/desorption and the electron transfer at the electrode-electrolyte interface. The slowest of these steps, called the rate determining step, is decisive for the overall reaction rate, that is a function of the applied electrode potential. The Butler-Volmer equation correlates the current flowing during an electrochemical reaction with the potential difference $E - E_{eq}$. The difference between the required potential E and the equilibrium potential E_{eq} is called the overpotential η for a given electrochemical reaction. The Butler-Volmer Equation can be written as:[BF01]

$$i = i_0[\frac{C_X(0,t)}{C_X^*} \cdot exp\frac{-\alpha F\eta}{RT} - \frac{C_Y(0,t)}{C_y^*} \cdot exp\frac{(1-\alpha)F\eta}{RT}] \tag{2.3}$$

with the exchange current density i_0, the bulk concentrations of X and Y, $C^*_{X/Y}$ and the diffusion rate controlled and thus time-dependent surface concentrations of X and Y, $C_{X/Y}(0,t)$ and the transfer coefficient α, that describes the energy barrier symmetry between the species X and Y. The rate of an electrochemical reaction and its turnover frequency are crucial for reactions driven in any electrochemical application, thus electrocatalysis plays an important role for improving electrochemical applications

by increasing the activity of electrodes towards electrochemical reactions and thus, increasing the rate constants. Higher rate constants for a reaction require lower applied overpotentials at constant current densities.

2.1.3 Frumkin Effect

Frumkin observed that the current of the hydrogen reduction reaction from dilute acid is independent of the concentration of the acid at a constant overpotential. He attributed this observation to a change of H^+ concentration at the reaction site in the EDL, together with a shift in equilibrium potential for the reaction. This behavior is generally applicable for electrochemical reactions at solid-liquid interfaces and is called the Frumkin effect. It describes the possible difference of concentrations of reactive species between the EDL and bulk solution at potentials negative of the potential of zero charge (pzc). This effect is of great importance for electrochemical reactions at interfaces, because it greatly influences the reaction kinetics [Fru33]. The reduction rate of protons at a metal electrode, for example, is proportional to the concentration of H^+ in the EDL, which can differ significantly from the proton concentration in the bulk, and, therefore, can lead to unexpected experimental results if this concentration difference is not considered. In chapter 5 we present an approach to directly probe this concentration difference of protons by electrochemical fluorescence microscopy.

2.1.4 Electrochemical Double Layer

Generally speaking, the electrochemical double layer (EDL) is the phase boundary between an electron conductor and an ion conductor. In the case of solid electrodes and liquid electrolyte, as relevant for the work in this thesis, the EDL is formed at the solid-liquid interface between the metal electrode and the electrolyte. The EDL consists of charged ions and solvent molecules, which accumulate in close proximity to the electrode surface and form a layer that neutralizes the electrical charge of the electrode and forms an electrostatic equilibrium between the charged species in the electrolyte and the electrode. Figure 2.2 shows schematically the EDL between a solid electrode and liquid electrolyte. The electrode (left, gray layer) and the electrolyte, consisting of solvated ions, specifically adsorbed ions without a hydration shell and other solvent molecules (right, white layer) build up the EDL. The inner layer, closest to the electrode surface is referred to as the Inner Helmholtz Plane (IHP). It contains solvent molecules and specifically adsorbed ions that are not hydrated. The second layer is the Outer Helmholtz Plane (OHP). Both form the compact layer of charges (CL) that is strongly associated with the charged metal electrode. The next plane is the diffuse layer, in which solvated ions and solvent molecules can diffuse freely.

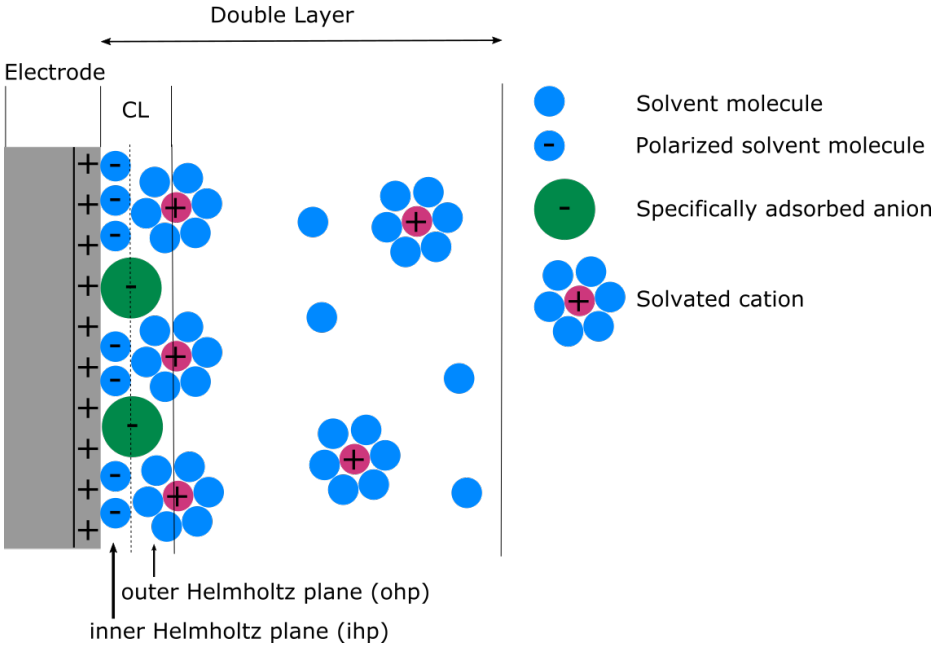

Figure 2.2.: Schematic representation of the EDL. The compact layer is presented in magenta color, consisting of the IHP and OHP. Image adapted from [MFC17]

.

Electrochemical processes at the electrolyte-electrode interface can be influenced by the presence of specifically adsorbed ions in the EDL, thus, the study and knowledge about the conditions in the EDL are important to understand electrochemical reactions.[Col+16] In our work, the specific adsorption of solvent molecules, i.e. (bi-) sulfate is detectable in TERS and influence the specific adsorption of CO as reaction intermediate during FAO as discussed in chapter 3.

2.1.5 Electrochemical Prototype Reactions

Electrochemical prototype reactions are simple reactions of small molecules driven by the force of an applied potential in an electrochemical cell. Prototype reactions are used in fundamental science to study reaction mechanisms of the reactions themselves or to study systems that are used to run the reaction, such as heterogeneous catalysts in form of the nature of the WE in electrochemical experiments. The prototype reactions should be easy to understand and should not lead to numerous side reactions to be able to assign experimental findings to specific steps of the reaction. Nonetheless, reactions that are supposedly easy to understand such as HER or FAO are not yet fully understood in all facets and still subject of fundamental research in the field of electrochemistry.

2.1.5.1 Hydrogen Evolution Reaction

The HER is one of the most studied electrochemical prototype reactions. It describes the splitting of water and production of hydrogen during water electrolysis in an electrochemical cell. The HER is a cathodic reaction that occur at low potentials on metal electrodes. The potential at which the HER occur is the lower limit of the potential window in aqueous media. On a Pt electrode, the HER can be run with an applied overpotential close to 0.[Eft17] Nonetheless, PGMs are expensive and/or rare materials that cause the production of hydrogen in fuel cells to be uneconomic. The demands in 'clean' and 'sustainable' hydrogen are growing and need to be satisfied by the development of cheaper electrocatalysts. The HER mechanism can be split into two steps. The first step of HER is the adsorption of H on the electrode surface. This step, referred to as the Volmer step[Eft17], is most often rate-determining. The second step is the reaction of adsorbed hydrogen with either H^+ from the electrolyte (Heyrowski step) or with a second adsorbed H (Tafel step) to form molecular H_2.[GC98; Eft17]

$$H_2O + e^- \leftrightarrow H_{ads} + OH^-(\text{Volmer}) \tag{2.4}$$

$$H_{ads} + H_2O + e^- \leftrightarrow H_{2g} + OH^-(\text{Heyrowski}) \tag{2.5}$$

$$H_{ads} + H_{ads} \leftrightarrow H_{2g}(\text{Tafel}) \tag{2.6}$$

As the rate of the H adsorption is the rate-determining step of the HER, the focus in catalyst development is on finding catalysts that provide the best possible fit for metal-substrate interactions that are strong enough to effectively adsorb hydrogen, yet not too strong, to still be able to catalyze the Tafel and Heyrowski steps, following Sabatier's principle.[Rot08] Pt, as the best known bulk metal catalyst for HER, has an adsorption free energy for hydrogen close to 0, providing effective adsorption of hydrogen and catalysis of the following Heyrowski or Tafel step. The underlying mechanism of HER for a given catalyst can be experimentally predicted by analyzing the Tafel slopes for the HER. Conway and Tilak proposed a model to correlate the experimentally accessible Tafel slope with the three HER steps.[CT02]
In chapter 3 of this work, we examine the catalytic activity of a bimetallic catalyst for HER as function of PGM adlayer properties, which is a way to reduce the amount of PGM needed without loosing the outstanding performance for the catalysis of the HER of such PG metals.

2.1.5.2 Formic Acid Oxidation Reaction

Another well studied electrochemical reaction of a small molecule is the electrochemically induced oxidation of formic acid (FAO). The reaction is of major importance in the field of green energy as it is the underlying reaction in direct formic acid fuel

cells (DFAFC). The reaction mechanism of FAO has been studied for a long time[CP73; PV88; Mar+95]. The first formic acid driven fuel cell was reported in 1996.[Web+96] Today, the accepted mechanism of FAO follows one or a combination of three possible reaction pathways[YP08], that are shown in figure 2.3 and detailed in figure 2.4.

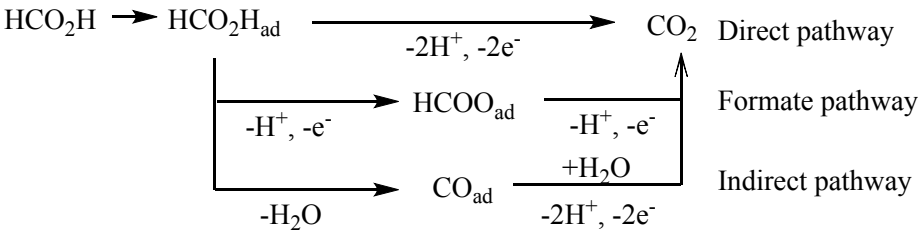

Figure 2.3.: Possible reaction pathways of formic acid oxidation. The direct pathway lead to the formation of CO_2 via direct dehydrogenation of formic acid. The formate pathway has adsorbed formate as reaction intermediate, while the indirect pathway proceeds via dehydration of formic acid and adsorbed CO as reaction intermediate to CO_2. Image adapted from [Ohm+23]

The direct pathway of FAO occurs via dehydrogenation of formic acid and leads directly to CO_2 as product without the formation of CO as intermediate. The formate pathway leads to the intermediate formation of adsorbed formate prior to the formation of the product CO_2. The third pathway forms adsorbed CO as intermediate product by dehydration of formic acid. Figure 2.4 shows the details of the FAO mechanism. Starting from formic acid (marked with a green circle), the mechanism can proceed by orientation of formic acid with H or O down to the catalyst surface (up and left), deprotonation of formic acid (down) or adsorption of formic acid (right, red circle). Once adsorbed, the formic acid molecule gets deprotonated and can reorient to be adsorbed via one or two O atoms (top left, bottom left) or via the C atom (top right). A subsequent reduction step leads to CO_2 in all three cases via the formate pathway. The reaction pathway on the upper side starting from the red circle shows the indirect pathway via dehydrogenation of adsorbed formic acid to intermediate CO. In fuel cells and other catalyzed FAO applications, the direct pathway is desired, because the intermediate formation of CO may lead to significant poisoning of the active sites of the catalyst and the loss of its catalytic activity towards FAO. This issue of FAO is addressed in chapter 4 of this thesis, where the poisoning of Pd modified Au(111) is probed with CV and EC-TERS.

The presence of CO as main poisoning species during FAO is widely accepted in the field and was studied used various spectroscopy and electrochemical techniques.[Wan+18b; BBL83] The occurrence of a poisoning agent during the operation of a fuel cell or other FAO applications is undesirable and thus the indirect pathway needs to be avoided. This fact devalues some catalysts as they lead to a significant shift of the mechanism towards the indirect pathway, like bulk Pt catalysts.[Cue+12] The requirements of a FAO catalyst material for use in technical applications are therefore the lowest possible cost, i.e. high mass activity, high electrocatalytic activity, safety in use, high tolerance to possible poisoning agents and high stability under electrochemical conditions.[Wan+18a; Don+18]

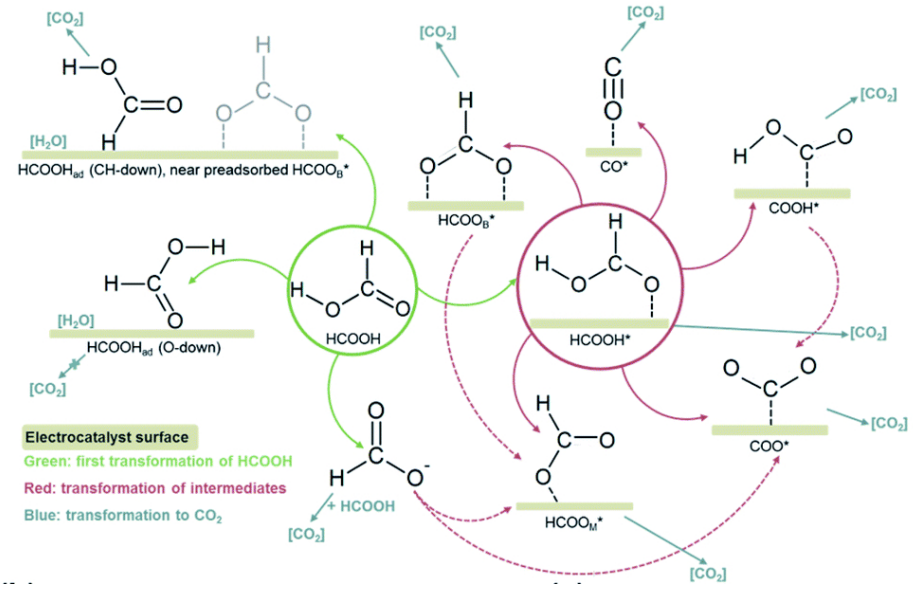

Figure 2.4.: Possible reaction pathways of FAO in detail. Image reprinted from [FC21] under CC license (CC BY-NC 3.0)

2.1.6 Catalysis in Confined Space

The field of catalysis has attracted enormous interest in the current discussion of global warming and dependency on fossil fuels. With the possibility of using highly active, highly specific and selective catalysts, many reactions that are cost-intensive or uneconomical can be driven more economically. As of today, many catalytic systems are based on 'traditional' heterogeneous catalysts, like bulk metals, alloys or metal oxides.[Zha+20] One field of research in the improvement of catalysts in terms of specificity, selectivity and mass-activity is the confinement of such catalysts, to make use of so-called confinement effects. The term confinement in the sense of catalysis expands to confinement of the crystal lattice, 2D material confinement or interfacial confinement.[Zha20]

Confined-space catalysts stand out by the surrounding of catalytically active sites on the nanometer scale that can lead to modulation of the electronic and geometric structure of the active sites. Moreover, the high reactive-site density of the catalytic material by introducing a high number of defect sites on the nanometer regime can directly improve the catalytic activity.[Zha20; Yan+18; Xin+18]

Next to concepts like metal organic frameworks (MOF), covalent organic frameworks (COF) or microporous catalysts, one method to achieve nano confinement of a catalytic system is to introduce two dimensional, island-like structures of a catalytically active material on a supporting material. This concept is widely facilitated and most-often studied in form of PGM islands on supporting materials like Au[SP18], Pt[LKA10; HCS58] or ignoble supporting materials like Al[Wol+98] or Ce[Ben+96].

2.1.7 PGM Nanoislands

The origin of the effect of nanoislands on the catalytic activity are twofold. The environment of the islands, i.e. the underlying supporting material, exhibits its own catalytic activity for a given (part of a) reaction. The phenomenon of spillover in catalysis describes the migration of adsorbed species between different surface sites, i.e. between the PGM islands and their supporting metal.[XGQ21] This spillover effect can increase the catalytic activity because one metal site can be better in adsorption and splitting of the reactant while the other metal site can more easily react with the intermediate. The concept is shown schematically in figure 2.5.

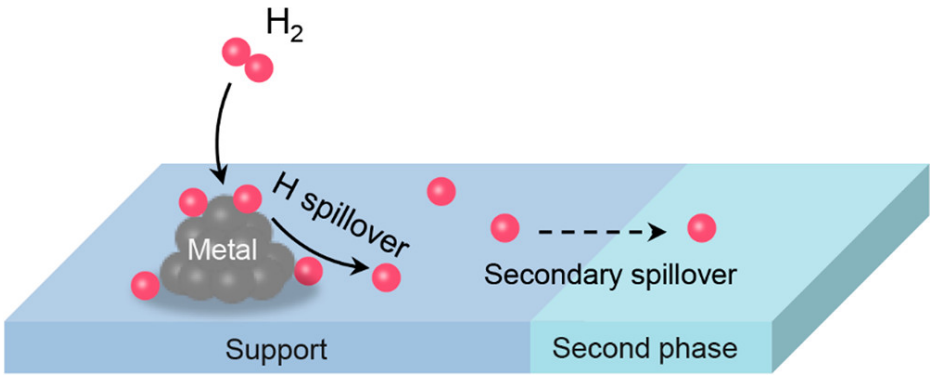

Figure 2.5.: Illustration of the hydrogen spillover after adsorption and splitting on a island-like metal overlayer structure onto the underlying supporting metal. Image reprinted from [XGQ21]. Copyright 2021, with the permission from American Chemical Society

In case of molecular hydrogen, the reactant can be effectively dissociated on PG metals[GAS13] and then spill over to the supporting material, where a secondary reaction can be catalyzed. Yin et al. used STM-based TERS to probe the hydrogen spillover of Pd islands on a Au support by means of the hydrogenation of chlornitrobenzenethiol (CNBT) to chloroaminobenzenethiol (CABT).[Yin+20] They found that the decomposition of molecular hydrogen happened at the Pd sites, whereas the hydrogenation of CNBT to CABT happened on the Au sites of the catalyst.

The second effect of the island-like 2D confinement of a catalyst is the change in the electronic properties and lattice parameters, induced by the strain of the underlying material.

Several methods to achieve 2D admetal islands have been reported. Throughout this thesis, the route via UPD and subsequent galvanic displacement of the UPD metal with the PGM target was used for preparation of the islands. UPD is a very-well studied technique that has been used for decades to deposit metal layers on a supporting electrode.[DKS76; HZK95] The advantage of the UPD route is the controllable island outcome, that is influenced by the parameters of deposition duration and potential, as described in detail in chapter 3. In the subsequent displacement, the UPD metal atoms are replaced by the target PGM atoms with charge dependent stoichometry. Another

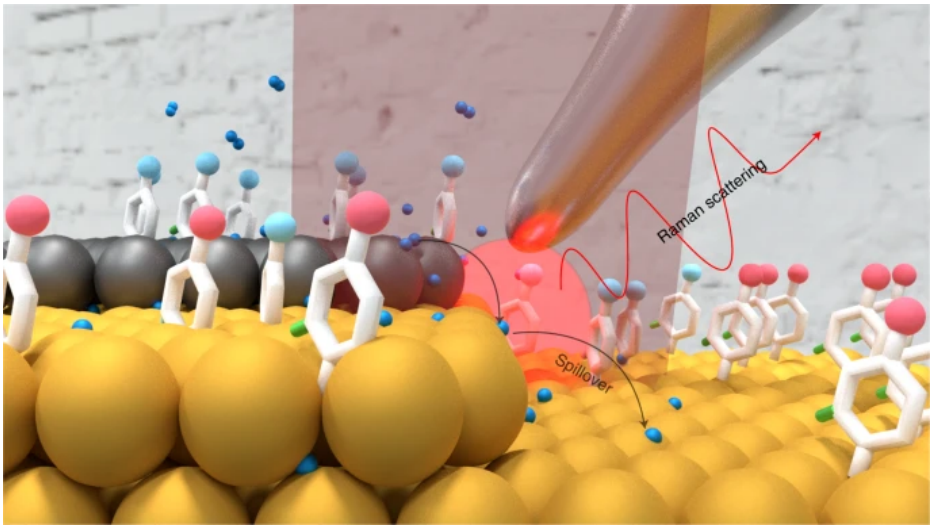

Figure 2.6.: Illustration of the hydrogen spillover after adsorption and splitting on a Pd island and subsequent reaction on the Au site. Image reprinted from [Yin+20]. Copyright 2020, with permission from Springer Nature

route is the direct electrochemical deposition of the target PGM on the supporting material. This route provides an easy way to obtain a controllable amount of the admetal, forming mono- to multilayers. The irregularity of the resulting islands or layers is the weak point of that route.[Kib+99; Tan+05]

2.1.8 Vibrational Spectroscopy

Optical spectroscopy is a method to study the interaction between electromagnetic radiation in the optical spectrum with matter. It allows to measure the intensity of electromagnetic radiation as a function of its wavelength after the interaction of an incident optical beam with the material of interest. The nature of interaction between the exciting light and the material can be manifold. In optical absorption spectroscopy, the absorption of the incident light is measured as function of frequency. The method is based on the excitement of a molecule's energy level from a ground level S_0 to an excited, higher energy level S_1 by an incident photon of the energy $\hbar\omega$. In order to excite the molecule, the transition needs to be dipole-allowed, which means that the photon can energetically couple to the described transition of energy levels.[Hol04] Absorption spectroscopy is sensitive to the electronic and molecular composition of a material[Hol04]. The excitation of the absorbing material depends on the energy of the exciting light. In IR absorption spectroscopy, a molecule is excited to a higher vibrational or rotational level within an electronic level, that allows probing the vibrational modes of molecules that has dipole-allowed transitions. In UV/Vis absorption spectroscopy, a molecule's energy level is excited to a higher energy level, that makes it a tool for probing the electronic states of the material of interest.[Hol04]

A second nature of optical interaction is the stimulated emission of light by a material after its interaction with an incident electromagnetic wave. In case of fluorescence spectroscopy, the material absorbs a photon of specific energy $\hbar\omega$ and gets excited from its electronic ground state to a vibrational mode of an excited state, according to the absorption spectroscopy described above. Subsequently, the molecule can loose energy by non-radiative transmission, i.e. vibrational relaxation, in which the molecule looses its energy to the surrounding until the lowest vibrational state of the excited state is reached. From the vibrational ground state of the excited state, the molecule can loose energy by the emission of a photon of the energy that corresponds to the energy difference between the vibrational ground state of the excited state and some vibrational state of the ground state.[Hol04] The emitted photon is measured in fluorescence spectroscopy as function of the wavelength. The principle of fluorescence is described in more detail in section 2.1.10.
A third nature of interaction between matter and incident light is inelastic light scattering. In inelastic light scattering in the sense of optical spectroscopy, the energy of an incident photon is either partially transferred to the the interacting material or, part of the energy of the material is transferred to the photon, increasing its energy. These processes are studied in Raman spectroscopy experiments, which are the basis of TERS and described in detail in the following section.

2.1.9 Raman Scattering

Raman scattering describes the inelastic scattering process of photons by matter. The process of inelastic scattering involves both, a change in the energy of the incident photons as well as a change in the traveling direction of the photon, both caused by the interaction with a material of interest. This process is shown in figure 2.7 in form of a Feynman diagram.[Jal+06]

The incident photon of an energy $\hbar\omega_{\mathrm{P}}$ is inelastically scattered under the loss of a phonon of the energy $\hbar\omega_{\mathrm{V}}$. The scatterd photon energy is redshifted compared to the incident photon to the lower energy $\hbar\omega_{\mathrm{S}}$. This process is called Stokes Raman scattering. The process in which the photon energy blueshifts through the absorption of a phonon with the energy $\hbar\omega_{\mathrm{V}}$ is called anti-Stokes Raman scattering. As can be seen from the diagram, Raman scattering describes a simultaneous occurring instantaneous absorption and emission of photons of different energy due to light-matter interaction.[Hol04]
In the classical view[LE09; Hol04; Lon02], which is discussed briefly in the following paragraph, the Raman scattering process can be described as the radiation by an oscillating dipole induced by an incident electromagnetic wave. The incident electromagnetic field $\overrightarrow{E}$ induces a dipole moment $\overrightarrow{\mu}$ upon interaction with a molecule with a proportionality factor α that describes the tendency of the molecules electron density

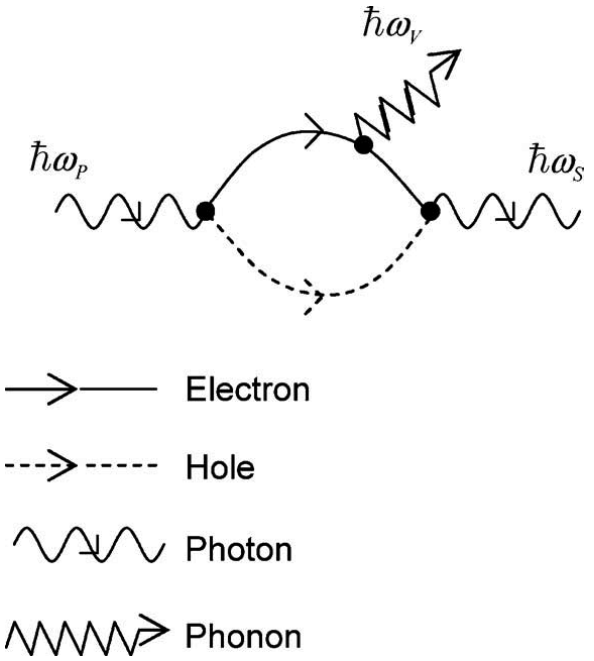

Figure 2.7.: Feynman diagram of the inelastic scattering process in Raman scattering (Stokes Raman scattering). An incident photon of energy $\hbar\omega_{\mathrm{P}}$ is scattered at matter under the loss of a phonon of the energy $\hbar\omega_{\mathrm{V}}$. A photon of the lower energy $\hbar\omega_{\mathrm{S}}$ than the incident photon is scatterd. Image reprinted with permission from [Jal+06]. Copyright 2006, with the permission from IEEE.

to be distorted by the incident field and is called polarizability tensor.

$$\overrightarrow{\mu} = \alpha \cdot \overrightarrow{E} \tag{2.7}$$

The polarizability tensor is not a molecular constant but changes with the oscillations of the molecule by small changes in the molecular structure through nuclear motion. α can be expressed with respect to the coordinates of the normal mode, which are associated with the respective molecular vibrational frequencies ω_{k} and ω_{l}, in a Taylor expansion as follows:

$$\alpha_k = \alpha_0 + \sum_k (\frac{\partial \alpha}{\partial Q_k})_0 \cdot Q_k + \frac{1}{2} \sum_{k,t} (\frac{\partial^2 \alpha}{\partial Q_k \partial Q_l})_0 Q_k Q_l + ... \tag{2.8}$$

with the polarizability tensor at equilibrium α_0 and the normal mode coordinates $\mathrm{Q_k}$ and $\mathrm{Q_l}$. Quadratic and higher terms of the Taylor series can be neglected under the condition that only very small perturbations of the polarizability occur. With that, equation 2.8 can be rewritten for a specific normal mode k:

$$\alpha = \alpha_0 + \frac{\partial \alpha}{\partial Q_k})_0 \cdot Q_k \tag{2.9}$$

If we further approximate the vibration coordinate $\mathrm{Q_k}$ oscillation around the equilibrium

position to be harmonic

$$Q_k = Q_k^0 \cdot cos(\omega_k \cdot t) \tag{2.10}$$

and an incident electric field that can be described as:

$$\overrightarrow{E} = \overrightarrow{E_0} \cdot cos(\omega_0 \cdot t) \tag{2.11}$$

we can introduce the equations 2.9, 2.10 and 2.11 into equation 2.7, to obtain equation 2.12:

$$\overrightarrow{\mu} = [\alpha_0 + \alpha_k^{'} Q_k^0 \cdot cos(\omega_k \cdot t)] \cdot \overrightarrow{E_0} \cdot cos(\omega_0 \cdot t) \tag{2.12}$$

with $\alpha_{\mathrm{t}}^{'}$ being the derived polarizability tensor $\frac{\partial \alpha}{\partial \mathrm{Q_k}}$. Equation 2.12 can be further rewritten with the use of trigonometric relations to obtain a sum of three terms to express the induced dipole moment under the influence of an external electromagnetic field:

$$\begin{aligned} \overrightarrow{\mu} = & \underbrace{\alpha_0 \cdot \overrightarrow{E_0} \cdot cos(\omega_o \cdot t)}_{\text{Rayleigh term}} \\ & + \underbrace{\frac{1}{2} \alpha_k^{'} Q_k^0 \overrightarrow{E_0} \cdot cos[(\omega_0 - \omega_k) \cdot t]}_{Stokes\ Raman\ term} \\ & + \underbrace{\frac{1}{2} \alpha_k^{'} Q_k^0 \overrightarrow{E_0} \cdot cos[(\omega_0 + \omega_k) \cdot t]}_{anti-Stokes\ Raman\ term} \end{aligned} \tag{2.13}$$

Equation 2.13 describes three terms that represent different components of scattered light.[LE09; Hol04; Lon02] The first term is the Rayleigh term, that describes the elastic scattering that radiates at the same frequency (ω_0) as the incident wave.
The second term is the Stokes Raman term, that describes the inelastic scattering that results in radiation with lower frequency than the incident field, whereas the anti-Stokes Raman term describes inelastic scattering resulting in scattered light with higher frequency. The three types of scattering are depicted in the Jablonski diagram in figure 2.8.[Dey22] Even though the classical view of Raman scattering is simplified and does not take into account all aspects that a quantum mechanical description can provide, it gives a good approximation of the scattering process. With equation 2.13 we can see, that if the polarizabilty tensor changes upon vibration, i.e. $\alpha_{\mathrm{k}}^{'} \neq 0$, the mode is Raman active and leads to Raman scattering. If the polarizability tensor does not change upon vibration, the Stokes and anti-Stokes Raman terms vanish and the mode is Raman inactive. The quantum mechanical discussion of Raman scattering is beyond the scope of this thesis. The interested reader is referred to the work of E. Le Ru[LE09] for a detailed review about the quantum mechanics of Raman scattering.
Raman active modes, i.e. modes that undergo a change in polarizability, transform with the same symmetry as the quadratic forms that are found in the character tables of the point group of the respective molecules.
Changes in the chemical environment or orientation of a molecule affect the interatomic bonding energies within the molecule, resulting in a change in the energy difference

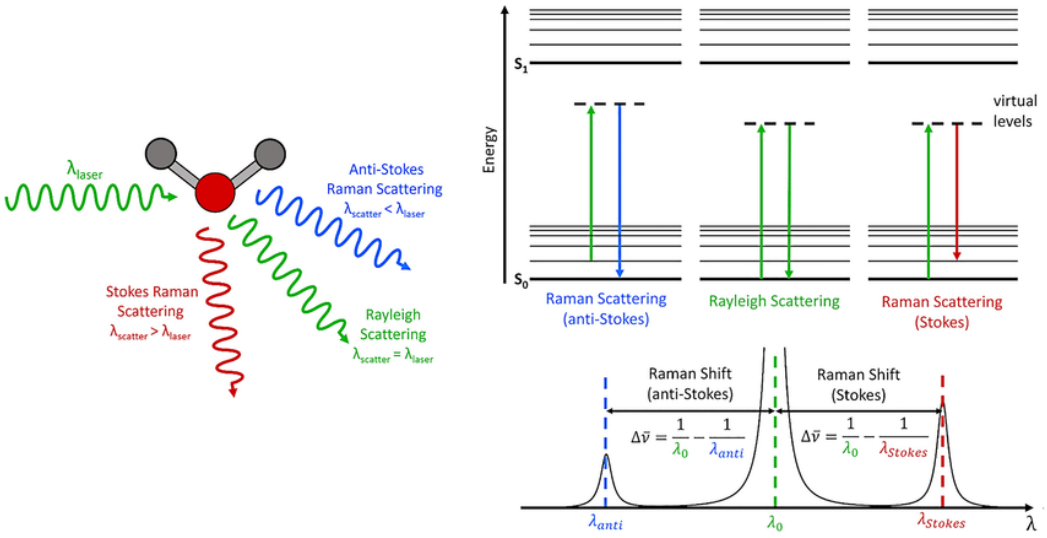

Figure 2.8.: Schematic representation of the three types of scattering encountered during Raman experiments. The Rayleigh scattering describes scattered light at the same frequency as the incident wave. Anti-Stokes Raman scattering with low intensity is scattering of radiation of higher frequency than the incident electromagnetic wave, whereas Stokes Raman scattering describes radiation after inelastic scattering with lower frequency than the incident wave. Image reprinted from [Dey22], Copyright 2022 with the permission of Springer Nature.

between the exciting and emitted photon. This characteristic energy difference, the Raman shift, allows the characterization of chemical samples by their Raman signature like a chemical fingerprint. For example, in case of CO, whose Raman response is discussed in chapter 4, the gas phase Raman shift $\Delta\overline{\nu}$, which is the difference between the excitation and scattered photon frequency[Hol04], is in the range of 2140 cm^{-1}[Pet+19]. The CO Raman shift of CO adsorbed to a transition metal surface can, however, vary significantly from the gas phase value by influencing the bonding strengths and thus, the vibration frequencies. The Raman shift of CO_{ads}@Pt is, for example, in the range of 2070 cm^{-1}[Li+15], while CO adsorbed to island like PdOx species is reported in this thesis to be in the range of 2190 cm^{-1}. Generally, in a simplified model, the molecule vibration can be considered as an oscillating spring and described in a classical approach[Van13]: The oscillation of a spring with the spring constant k follows:

$$\nu = \sqrt{\frac{k}{m}} \tag{2.14}$$

with the mass m, connected via the spring constant k to an infinite mass. From that equation it can be seen, that the involved atomic masses as well as the interaction strength, i.e. bond strength, play a role in the resulting Raman shift. Higher masses lead toward lower wavenumbers, whereas stronger bonds, i.e. double or triple bonds, lead to higher wavenumbers in Raman experiments.

The Raman signals are broadened to a band with a certain full-width at half maximum (FWHM). One factor (amongs others such as Doppler broadening, thermal or collisional effects) that results in band broadening are the non-infinite lifetimes of the excited

vibrational states.[LE09] Due to this, the energy of the states is not always equal and the photon energy of the scattered photons is distributed around a value ν_{R}. More ordered structures, i.e. higher crystallinity, results in more narrow bands, whereas more amorphous or impure structures exhibit broader bands.
The strength of the Raman signal is usually weak, because of very low Raman cross sections (the ratio between incident and scattered power $\sigma = \frac{\mathrm{P_s}}{\mathrm{P_i}}$) in the order of 10^{-29} to 10^{-31}.[LE09] However, if the probed molecules' virtual states equals an electronic transition, the probed molecule is in resonance with the exciting wavelength and the Raman intensity is increased. This phenomenon is referred to as resonance Raman scattering and can often be encountered when probing large molecules that act (partially) as chromophore, such as malachite green isothiocyanate, whose TERR fingerprint (tip-enhanced resonance Raman) was reported to be identifiable at surface coverages $\leq$0.7 pmol/cm^2.[DZP06] Crucial for obtaining a high Raman signal strength is also the choice of the excitation wavelength, as the Raman scattering efficiency is proportional to $\lambda_{\mathrm{ex}}^{-4}$. That means, excitation with monochromatic light of 532 nm wavelength is about 4.7 times more effective than excitation with a wavelength of 1064 nm.[Lar11]
The low Raman scattering cross-sections of non-resonant molecules makes Raman spectroscopy an intrinsic low-sensitivity technique. One way to overcome this disadvantage is to make use of the interactions of localized surface plasmons at metal surfaces with the electromagnetic field to enhance the Raman signal in enhanced Raman techniques such as TERS, which is discussed in detail in the techniques section, and SERS.

2.1.10 Fluorescence

Fluorescence describes the spontaneous radiation of light after the emitting matter was excited by an incident electromagnetic wave on timescales of 10^{-8} s. Moreover, it describes the allowed transition of an excited electronic state to a vibrational level of the electronic ground state.[SHE10]. According to Kasha's rule, that was proposed in the year 1950 by Michael Kasha, and the Franck-Condon principle, the transition always occurs from the vibrational ground state of the lowest excited state S_1, because excitation in energetically higher excited states will relax radiationless by inner conversion to the lowest excited state. The inner conversion process is about four orders of magnitude faster than fluorescence and much faster than phosphorescence. The probability for a radioationless transition is higher for transitions with small energetic difference, and thus, more likely to happen between energetically short distanced energy levels than between the lowest excited state and the ground state, whose energy difference is large.[Kas50; KW09] Kasha's rule is empiric and by today, there are exceptions from the rule, for example if the energetic difference between the two excited states S_1 and S_2 is big enough to significantly slow down the internal conversion so that fluorescence from the higher excited state S_2 is observable, which is the case in some thioketones.[WTS98] Figure 2.9 shows the Jablonski diagram for adsorption, followed

by radiationless relaxation processes to the energetically lowest excited state S_1 with subsequent radiation by fluorescence. According to the figure, the emitted photons

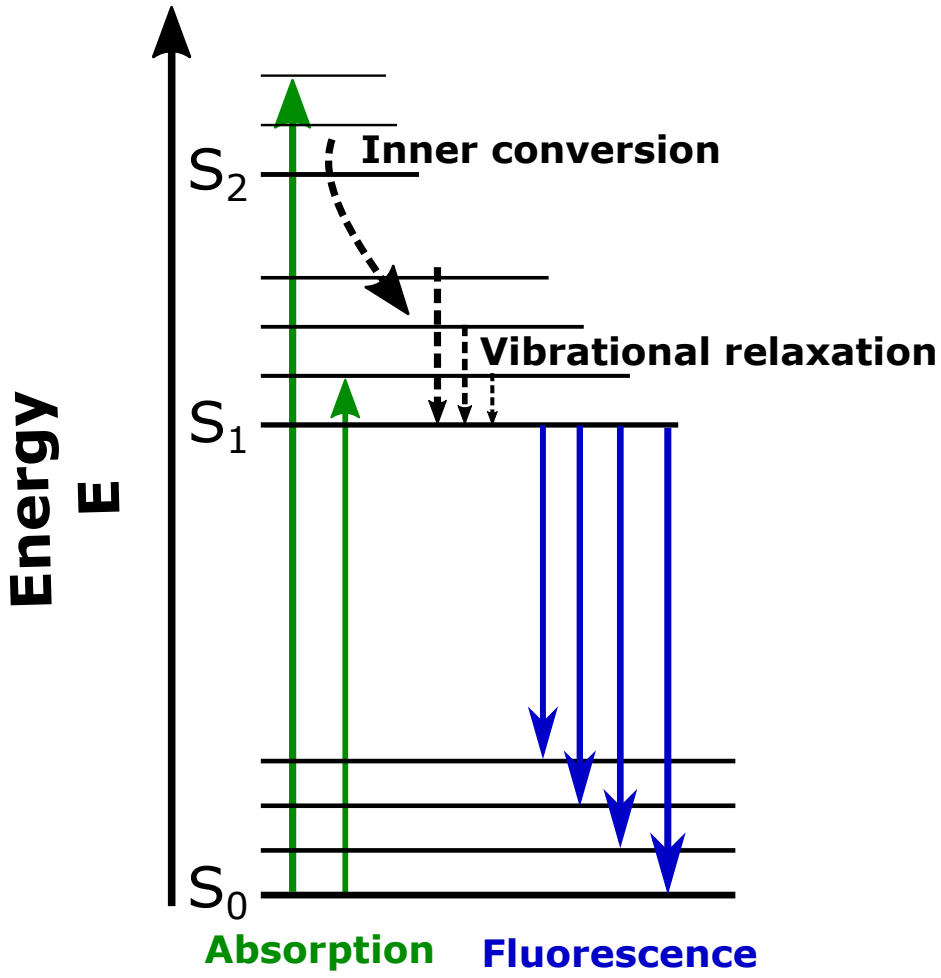

Figure 2.9.: Jablonski diagram for the process of absorption and subsequent fluorescence, after radiationless relaxation by inner conversion to the energetically lowest excited state.

by fluorescence normally have lower energy than the incident light, because of the radiationless relaxation of vibrational states, either after absorption or after fluorescence in higher vibrational states of the ground state, which is referred to as Stokes shift.
The lifetime of fluorescence, i.e. the duration in that the fluorophor is in its excited state before it relaxes into the ground state, is typically in the range of 1 to 100 ns. The lifetime is result of the spin allowed nature of the transition from the excited singlet state to the singlet ground state ($S_1 \rightarrow S_0$) that can happen without reversal of the spin of the involved electron.[WTS98] The other light emitting process, the phosphorescence from an excited triplet state on the other hand, needs reversal of the spin to relax into the the singlet ground state and is therefor a slow and unlikely process with lifetimes that can reach from seconds to days.
In the presence of suitable materials, the fluorescence can be quenched by radiationless deactivation of the excited fluorophor. Fluorescence quenching does not destroy the fluorescent nature of the fluorphor, but causes a decrease of the observed fluorescence

intensity. There are multiple mechanisms of fluorescence quenching. In the following, two processes are described that are of relevance for the work presented in chapter 5. The first mechanism of fluorescence quenching is dynamic quenching, in which the excited fluorophor is quenched by collision with a quencher molecule. If the fluorphor and the quencher molecule collide, the energy of the excited state is transmitted to the quencher without emission of a photon. It has been shown in many studies that the presence of oxygen leads to efficient quenching of the fluorescence.[LW73; Ber12] The process of dynamic quenching can be described by the Stern-Volmer-Relation that relates the decrease of fluorescence intensity, or fluorescence quantum yield, with the concentration of quenching molecules. The Stern-Volmer constant can be written as:

$$K_{SV} = \tau_0 \cdot k_q \tag{2.15}$$

with the fluorescence lifetime τ of the undisturbed fluorophor and the bimolecular quenching constant $\mathrm{k_q}$, that is related to the quencher concentration [Q] and the lifetimes of the disturbed and undisturbed fluorophors:

$$k_q = \frac{1}{[Q]} \cdot (\frac{1}{\tau} - \frac{1}{\tau_0}) \tag{2.16}$$

The fraction of the undisturbed fluorescence intensity $\mathrm{F_0}$ and the quenched fluorescence intensity F can then be described as:

$$\frac{F_0}{F} = 1 + K_{SV} \cdot [Q] \tag{2.17}$$

which is the Stern-Volmer relation.[Lak07]
The probability of quenching depends on the fluorescence lifetime of the fluorophor. The longer the lifetime, the higher the probability of a collision with a quencher molecule and thus, the higher the probability of quenching of the fluorescence. Furthermore, the concentration of the quencher is proportional to the probability of quenching. A higher temperature also leads to a higher quenching rate, because of faster molecular diffusion. This effect is incorporated in higher values of $\mathrm{K_{SV}}$ at higher temperatures.
The second way of quenching that is relevant for the experiments discussed in this thesis is fluorescence quenching by energy transfer to a metal, which has been subject to numerous studies.[RB80; CPS78; ZL07; Xu+04] The distance dependency of the quenching of fluorophores close to a Ag metal surface is shown in figure 2.11. The decay rate of pyrazine fluorophores increases dramatically with decreasing distance to a continuous Ag film. The authors attribute this dependency to the radiationless energy transfer between the excited fluorophor and the free electron gas in the metal.[RB80] The localized surface plasmons can couple with the electromagnetic wave of the emitter at sufficiently close distance to effectively quench the fluorescence.[CPS78] Approaching a metal surface closely can not only lead to quenching of the fluorescence, reports also suggests significant enhancement of the fluorescence intensity by metal surfaces in close proximity to fluorophores with a similar concept like SERS or TERS.[ZL07;

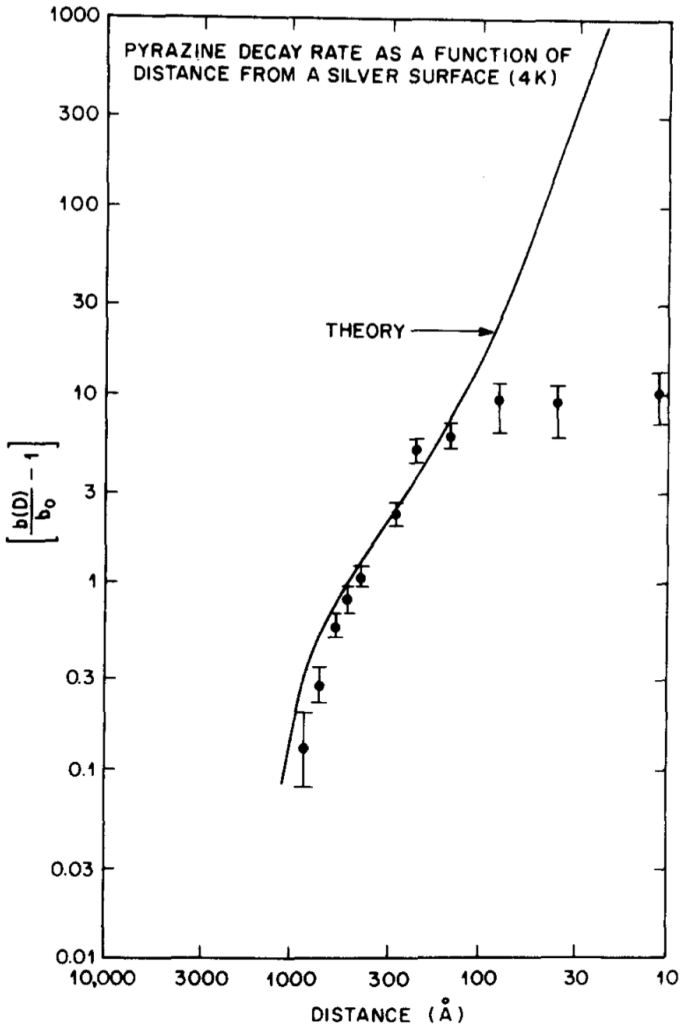

Figure 2.10.: Decay rate of pyrazine fluorescence as a function of distance to a continuous Ag film at 4 K. Image reprinted from [RB80]. Copyright 1980, with the permission of AIP Publishing

Wei+82; RB81; Xu+04] The enhancement factor of fluorescence close to Au is strongly dependent on the gold thickness layer, with an experimental maximum enhancement of about 6.5.[ZL07].

In this work, we make use of the pH dependent fluorescence of a fluorophor to measure the potential depndent surface pH of a Au(poly) electrode. The assumption of a difference in bulk pH and surface pH in an electrochemical cell is based on the Frumkin effect, that describes concentration differences of reactive species in an electrochemical cell during operation between bulk electrolyte and the EDL.

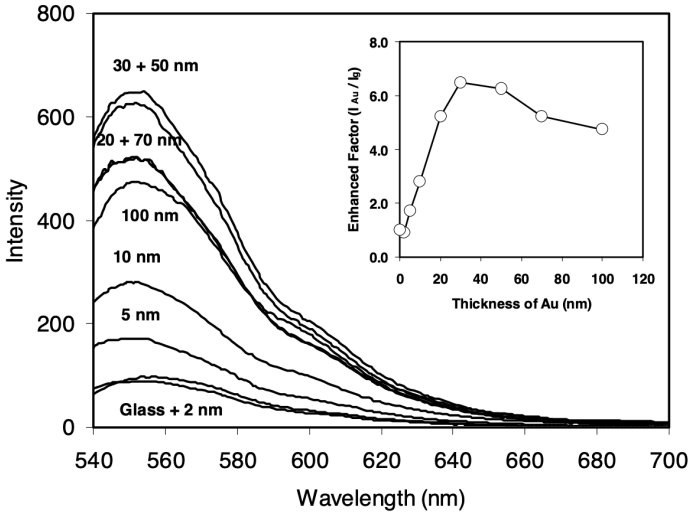

Figure 2.11.: Enhancement of the fluorescence intensity of Alexa Fluor 555 labeled anti-Rabbit igG on gold layers of varying thickness. Image reprintend from [ZL07]. Copyright 2007, with the permission from Optica Publishing Group

2.1.11 Fluorophores

A fluorophor is a molecule that has energy levels that can be excited by absorption of light and relax under emission of fluorescence photons. The absorption maxima can range from UV into the visible spectrum. The fluorescence energies are most often lower than the absorption energy and are in the visible to near infrared spectrum (Stokes shift). A characteristic absorption/emission spectrum of a fluorophor is shown in figure 2.12.

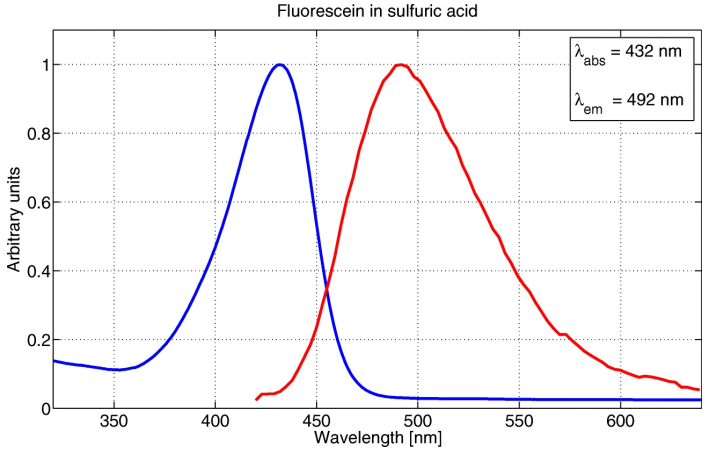

Figure 2.12.: Excitation and emission spectra of fluorescein, showing the Stokes shift of the wavelength between excitation (maximum at 432 nm) and emission (maximum at 492 nm). Image reprinted from [Kri+18] under CC license (CC BY).

The Stokes shift of the fluorescence allows the elimination of the excitation wavelength

by spectral filtering, so that only fluorescence emission photons can be detected. Typically, the structure of small organic fluorophores contains aromatic groups or have several π-bonds within the molecular structure, to allow excitation and emission in the UV/Vis/nearIR spectrum. The pH dependency of the fluorescence is provided through side groups that are sensitive to proton concentration, such as amino groups. In case of fluorescein, one of the most studied fluorophors due to its wide use in life science fluorescence microscopy[Gas+01; BK65; SNK95; The+14], the pH sensitivity of the fluorescence originates from different absorption properties of the brightly fluorescent di-anionic, deprotonated form and the non-fluorescent cationic form at low pH values.[Le +20] BODIPY fluorophores with pH responsive side-groups also show pH sensitivity in their fluorescence behaviour. Figure 2.13 shows the HOMOs and LUMOs of 2-substituted benzimidazole-BODIPY (BDP-BIM) in their neutral and protonated form.

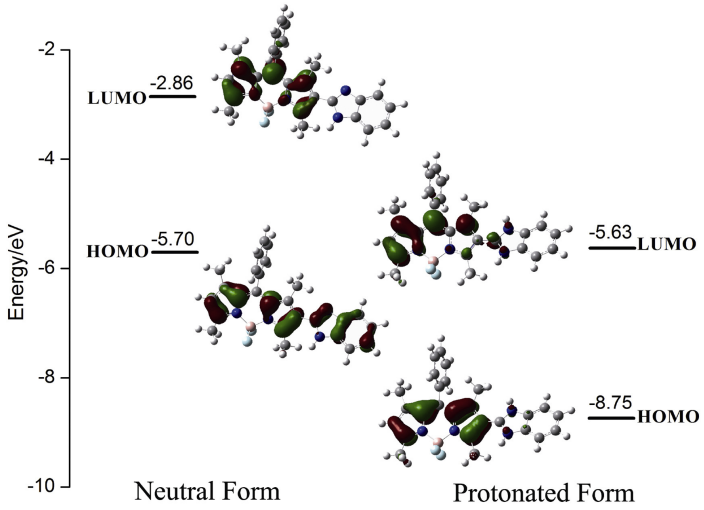

Figure 2.13.: Molecular orbital energy levels of BDP-BIM in neutral and protonated form. The HOMO of the protonated form shows contributions from both, the BODIPY core and the bezimidazole side group, in contrast to both, HOMOs and LUMOs of the protonated form, demonstrating the excistence of photoinduced electron transfer in the neutral state that leads to the bright fluorescence of the fluorophor. Image reprinted from [Li+16b]. Copyright 2016, with the permission from Elsevier.

BDP-BIM shows bright fluorescence in neutral to alkaline environments, whereas the fluorescence in acidic media is quenched. The DFT calculations of HOMO and LUMO show strong contribution of the BODIPY core in the LUMO of the neutral form and HOMO and LUMO of the protonated form, whereas the HOMO of the neutral form show contribution of the BODIPY core and the benzimidazole side group, demonstrating the quenching of fluorescence in the protonating form originating from the loss of photoinduced electron transfer between core and side group.[Li+16b]

The pH sensitivity of fluorophores can be used to measure the local pH of environments that are otherwise hard to access, like cell organelles or to measure the local pH in a small probing volume provided by the focus volume of a fluorescence microscope.

2.2 Techniques

2.2.1 Voltammetry

In cyclic voltammetry (CV) the current flowing per unit time through an electrode namely working electrode (WE) is measured as function of the applied WE potential. The applied potential is ramped up and down linearly in each cycle in a sawtooth pattern. When the potential is ramped in only one direction, either up or down, the technique is called linear sweep voltammetry (LSV). The current that is measured during the potential ramps is an average over the whole electrode area that is in direct contact with the electrolyte, i.e. the whole electrode-electrolyte interface. To be able to compare currents flowing in a reaction, the current is normalized to the exposed electrode area and reported as current density. Typically the CV of a RedOx couple shows two peaks, forming a 'Duck-shaped' CV response, schematically shown in figure 2.14a. The flat regime in the CV corresponds to the charging of the double layer and is non-Faradaic current. The positive peak is, according to IUPAC nomenclature, a result of the oxidation of the RedOx species and the associated charge transfer on the electrode-electrolyte interface, occurring during the anodic scan (positive potential scan direction). The peak current is reached after the mass diffusion to the electrode becomes the rate limiting step of the reaction. On further potential increase, the diffusion layer increases in size and causes a depletion of reactants in front of the electrode, resulting in a decrease of the observed current.

The change of the ramp direction, after the turning point of the CV, leads, given a reversible reaction, to a reduction of the oxidized form of the RedOx couple, leading to a negative current peak in the anodic scan direction. The two maxima in the CV are separated due to diffusion of the analyte to and from the electrode. The difference between the anodic and cathodic peak potential depends on the chemical and electrochemical reversibility of the reaction taking place. A fully reversible reaction shows a peak to peak separation of 57 mV at 25 °C, according to the Nernst equation. The separation increases with higher electron transfer barriers and therefore greater irreversibility of the electrochemical process.[Elg+18]

Most often for common electrochemistry experiments, a three-electrode setup is used for CV experiments. The three electrodes used are the working electrode (WE), the counter electrode (CE) and the reference electrode (RE). The current flows between the WE and CE, while the potential is applied to the WE in reference to the RE potential. Crucial for the use as RE is a highly stable potential and inert electrode material as well as non-polarizability and high impedance.[Elg+18] The CE enables the current flow by closing the electrical circle. The CE needs to be chemically stable

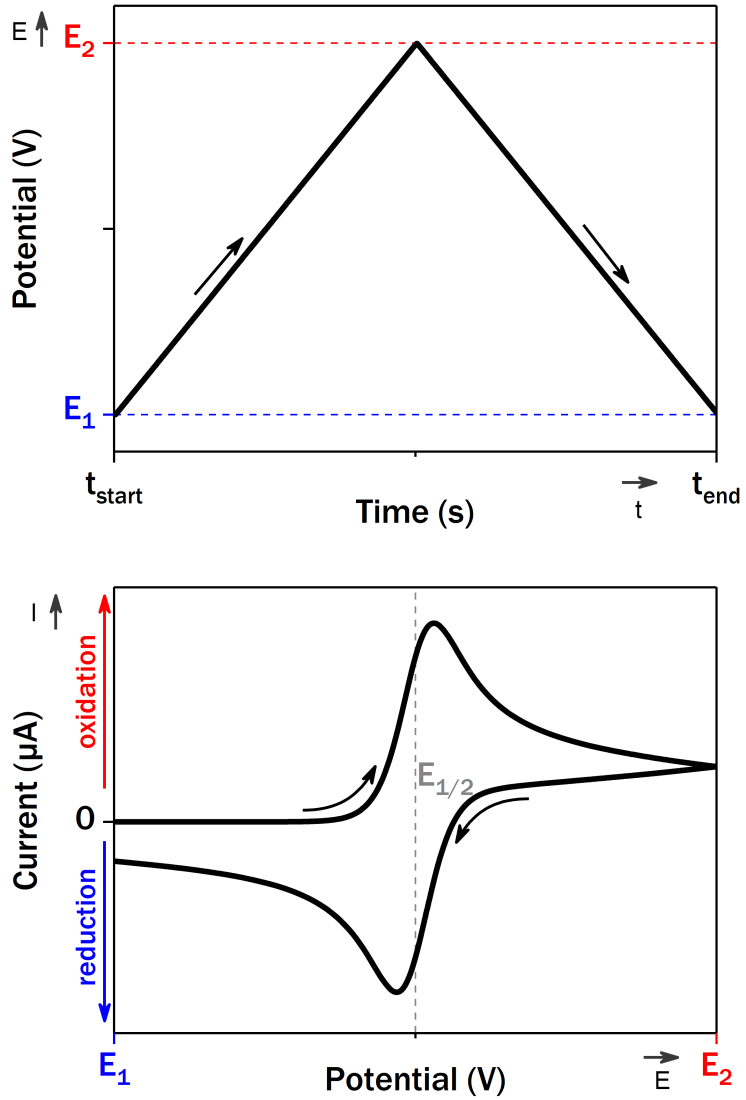

Figure 2.14.: (top) Sawtooth potential applied during cyclic voltammetry versus time during one cycle. The potential is ramped in the anodic scan direction until the CV turning potential is reached. Afterwards the potential is scanned in the cathodic direction until the start potential is reached. (bottom) Schematic CV of an electrochemically and chemically reversible RedOx reaction taking place upon potential scanning up and down in a CV experiment. Image reprinted from [23]. Copyright 2023

.

and positioned in a way to minimize interference with the processes taking place at the WE. As the reaction of interest occurs at the WE, the WE surface needs to be extremely clean and well-defined. The WE should be placed as close as possible to the RE to minimize the Ohmic drop (iR drop) across the electrolyte solution between WE and RE. Many different REs exist for aqueous media that is used in the experiments discussed in this thesis. The applied potentials are reported versus the RE used in the experiment or calculated to refer to a standard RE such as the reversible hydrogen electrode (RHE) or standard hydrogen electrode (SHE). The SHE reference potential is pH independent,

whereas the RHE potential depends on the pH of the electrolyte solution according to $RHE = SHE - 59mV \cdot pH$. In our experiments, we use a PdH reference electrode that consists of a Pd wire loaded with hydrogen prior to the experiment by applying a voltage high enough for hydrogen evolution. The produced hydrogen is incorporated into the Pd lattice and provides a stable reference potential, that equals the SHE reference potential at pH = 1, as (mostly) used in our experiments.

Electrochemical voltammetry methods are employed throughout this thesis for various tasks, such as the reduction and deposition of material on the WE (chapter 3) and the reaction of species triggered by the applied potential (chapter 3 and 4), and are used to investigate changes in the interfacial concentration of species differing from the bulk (chapter 5).

A picture taken of the electrochemical setup is shown in 2.15.

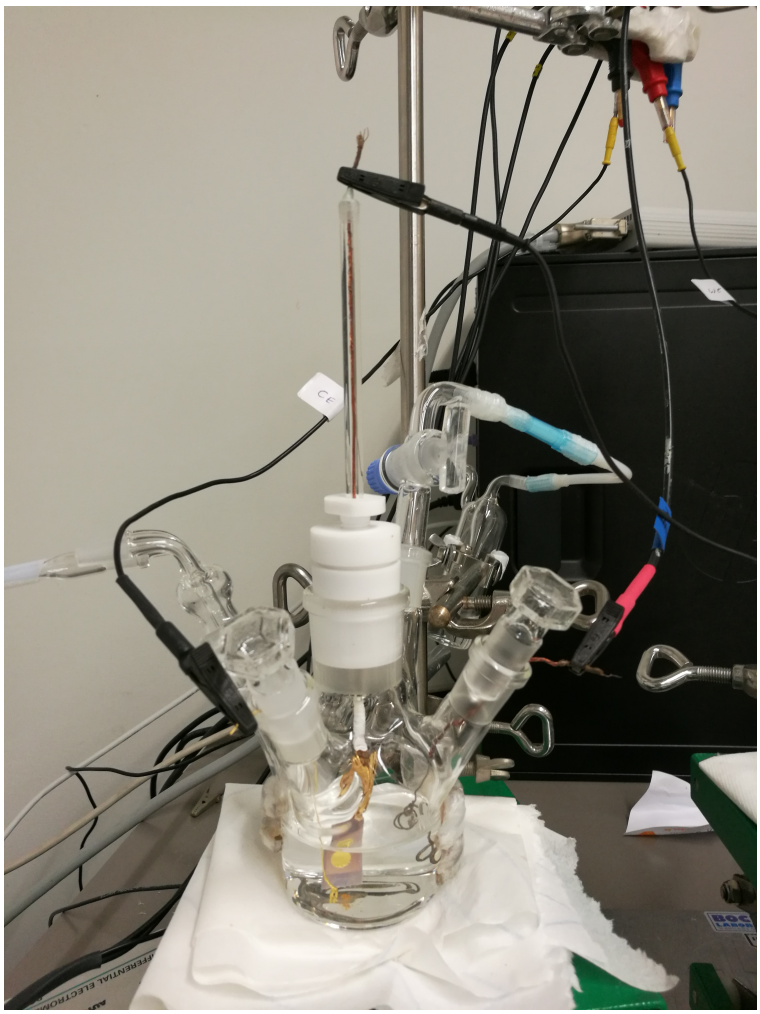

Figure 2.15.: Image of the electrochemical cell equipped with RE, CE and a gold sample on a glass slide covered with teflon tape that was used as WE.

.

The electrochemical experiments were performed using a Metrohm Autolab Potentiostat (PGSTAT 30) equipped with a Autolab Differential Electrometer Amplifier. The

three-electrode setup was set up in a glass cell (50 mL electrolyte capacity) with arms for the electrodes and gas in- and outlet. A sample holder was used to place the sample (Cr/Au on glass or a Au single crystal (10 mm diameter) in the center of the glass cell. The RE and CE were inserted through side arms in a way that the space between the WE and RE was minimized. A hydrogen-loaded Pd wire was used as RE, a Au-wire (0.5 mm diameter, 99.995% metal basis, Alfa Aesar) was used as CE after flame-annealing in a bunsen flame and rinsing with MilliQ. The RE was H_2-loaded in 0.1 M H_2SO_4 by applying a potential of 10 V between the Pd wire and a Au wire until the amount of hydrogen evolution corresponded roughly to the amount of oxygen bubbles formed at the Au wire.

2.2.2 Copper Underpotential Deposition

Underpotential deposition (UPD) describes the process of depositing a metal on an electrode material at a less negative potential than the Nernst potential for depositing the metal on a surface of the same material.[Ovi+16] Metals for which underpotential deposition has been observed show higher thermodynamic stability when deposited on a foreign material, as expressed by the more positive deposition potential. The underpotential deposition of a metal therefore leads to a maximum coverage of one monolayer. Further deposition of the metal requires a more negative potential to allow deposition of the metal onto itself. The bulk deposition accordingly requires a potential which is more negative than the theoretical Nernst potential. The cause of underpotential deposition is the magnitude of the metal-substrate binding energy compared to the binding energy between the metal and itself. This difference is influenced by differences in the lateral and vertical binding energy of atoms of the metal in nanostructures on the one hand and atoms of the metal with substrate atoms on the other hand as well as energetic influences of local defect structures on the substrate.[Ovi+16]

Figure 2.16 shows the CV of a Cu UPD on a gold surface. The CV shows three characteristic cathodic peaks. The first, at a potential of 0.52 V vs SHE, results from the reduction of Cu_2^+ and formation of a third monolayer on the gold substrate.[May+19] Reducing the potential to 0.34 V results in the deposition of the remaining 2/3 of the monolayer.[May+19] The cathodic peak at 0.34 V is, for high quality gold surfaces with a maximum mismatch of 0.5 °[Sol+08], split into two peaks. This is the result of the energetic difference between deposition on gold step sites (0.36 V) and terrace structures (0.34 V). A further decrease of the deposition potential leads to bulk deposition of copper and the formation of a copper multilayer. In the anodic scan direction, the first peak at 0.4 V shows oxidation of the first 2/3 monolayer of copper. The second peak, at a potential of 0.54 V, results from the oxidation of the remaining 1/3 monolayer. The lines in Figure 2.16 show the deposition potentials used in this work, which both result in a maximum coverage of one-third, but have differences in kinetics that are used to

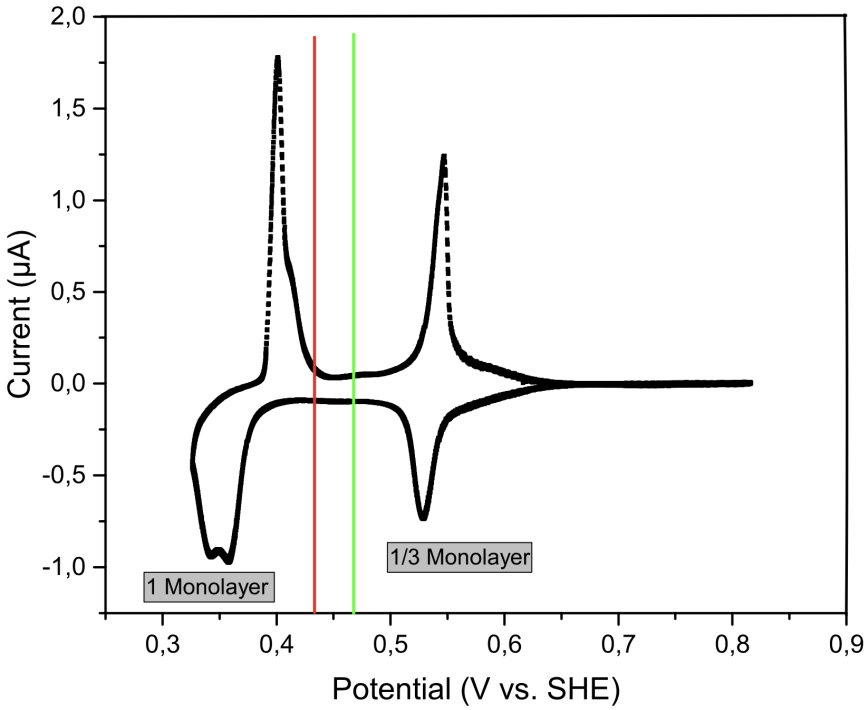

Figure 2.16.: CV of a Cu UPD from $CuSO_4$ on a Au(111) single crystal. The lines indicate the deposition potentials used in the work of this thesis

.

control the resulting submonolayer. This is explained in detail in the chapter 3. The occupation of different surface structures with the foreign metal when the potential is lowered is shown in Figure 2.17.

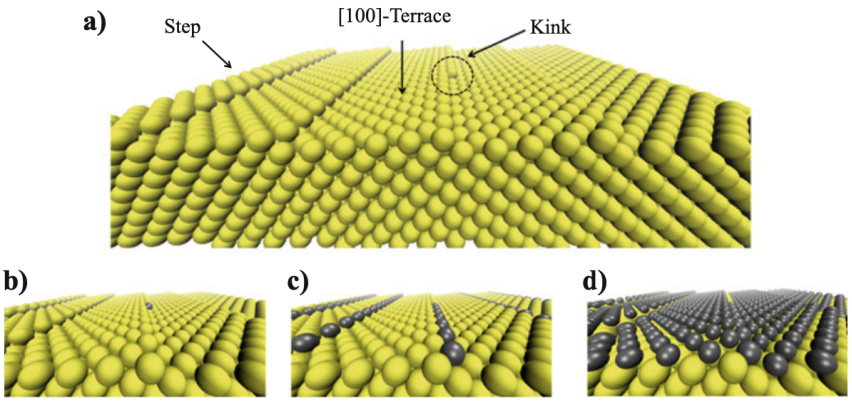

Figure 2.17.: Schematic representation of the underpotential deposition of a foreign metal (gray) on a defective substrate (yellow) upon potential decrease. Image reprinted from [Ovi+16]. Copyright 2016, with permission from Springer Nature.

.

2.2.3 Galvanic Displacement

Galvanic displacement occurs when a less noble metal gets in contact with the cation of a more noble metal. The displacement is a thermodynamic process in which it is more favorable to reduce the noble metal cation and oxidize the less noble metal, according to their standard redox potentials. The ignoble metal is oxidized and replaced by the more noble metal in the sense of a RedOx reaction. The process is schematically shown in figure 2.18 on the example of the replacement of metallic Cu with Pd originating from a Pd salt in solution.

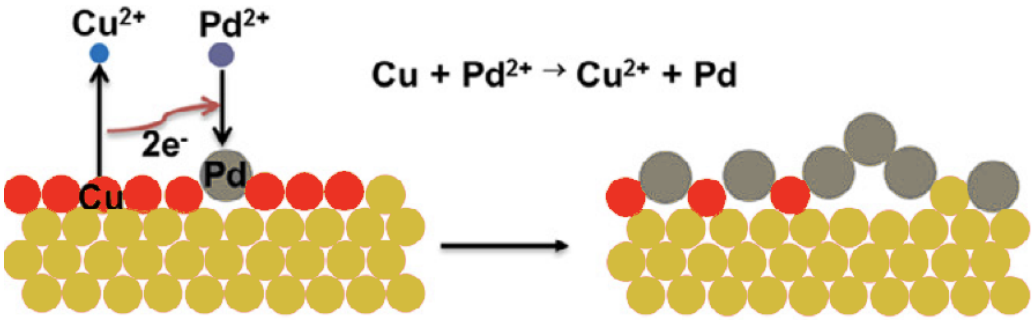

Figure 2.18.: Schematic presentation of the galvanic displacement of Cu with Pd_2^+. Image adapted from [Zha+17]. Copyright 2017, with the permission from Elsevier.

.

The galvanic displacement process is an electroless method that starts spontaneously because of the thermodynamics of the system. The advantage of this method over the direct deposition of noble metals is the controllability of the deposition of the ignoble metal prior to the displacement and, therefore, the controlled structure of the metal overlayer after the displacement, as the ignoble metal is replaced according to the ionic charge. The replacement reaction can be written as:

$$H_2M_a^{II}L_{4(aq)} + M_b^0 \rightarrow M_a^0 + 4L^- + 2H^+ + M_{b(aq)}^{II} \tag{2.18}$$

In this work, the galvanic displacement process is used to displace a metallic Cu overlayer on a Au electrode, produced by copper underpotential deposition by platinum group metals (PGM) that are more noble than Cu and therefore are spontaneously reduced and replace the metallic Cu overlayer.

2.2.4 Scanning Tunneling Microscopy

In scanning tunneling microscopy (STM), and generally applicable to scanning probe microscopy (SPM) methods, a probe is scanned over a surface of interest and local

sample properties that depend on the SPM technique, are measured with extraordinary resolution down to the atomic level.[Ryb15] The STM method was invented in 1982 at IBM by Binning and Rohrer.[BR82] A scheme of an STM is shown in figure 2.19.
The measurand in an STM experiment is the position of the tip relative to the sample surface on the z axis in constant current mode, or the tunnelling current in constant height mode.
The technique is based on the ability of an electron to cross a potential barrier of finite height between two conducting materials due to its wave properties, which is called 'tunnelling'. In quantum mechanical terms, the residence probability of the wave in the region of the potential barrier does not vanish, but decreases exponentially with the width of the barrier. After crossing the barrier, the wave can propagate again. Corresponding to the exponential decay of the wave function in the potential barrier, the measurable tunnel current is exponentially dependent on the distance between the two conducting materials, in the STM experiment these are sample and STM tip.[GW91] Typically, the tip-sample distance in STM experiments is in the order of a few nanometers to satisfy the tunneling conditions.[PLW12] Since the Fermi energies of the metallic sample and of the tip are equalized, so that no electrons can tunnel from higher occupied states into energetically lower unoccupied states, a voltage must be applied between the sample and tip. This bias voltage causes electrons to follow the gradient between the Fermi levels and a measurable tunnelling current is generated. In addition to the distance, the tunnelling current depends on the local density of states (LDOS) of the sample at the Fermi level, which indicates how many states exist in a given energy interval.[Voi15] In the case of metals, the local change in the density of states is very small due to the distribution of electrons. Therefore, the resulting signal in constant current mode, which follows the contour of the LDOS, can often be safely interpreted as a topography image of the sample.[PLW12]
In constant current mode, the measured tunnelling current is compared to a set target value and, using a control loop that controls the z position of the tip relative to the sample, is kept constant. The control loop compares the measured value of the tunnelling current with the setpoint. A fast response to changes in tunnelling current can be achieved by changing the distance proportional to the current change. A small change in the measured tunnelling current thus leads to a small change in the distance between the tip and the sample. This type of reaction to changes in the tunnelling current leads to a permanent control error, which can be eliminated by integrating the error signal over a period t and taking it into account in the control value. The two feedback mechanisms are called proportional and integral gain. When the feedback mechanism is set, the current image recorded in addition to the topography image corresponds to the error image of the control loop.[GW91]
In constant height mode, the tip is scanned over the sample at a fixed distance and the resulting tunnel current is recorded. The control loop is only used to compensate for a possible slope of the sample. Accordingly, the topography image provides no contrast in this mode. Instead, any change in sample topography is recorded as a change in tunnelling current that provides information about the topography. This mode is fast

and therefore less influenced by drift effects compared to the constant current mode, since no control loop is used, but can only be used with atomically flat samples.[GW91]

The movement of the tip in x,y,z directions is precisely controlled by piezoelectric actuators on the (sub-)nanometer level that can react to minimal deviations in the measured tunnelling current, which is in the order of pA to nA and measured by a highly sensitive preamplifier.[PLW12]
With STM, resolutions down to 0.1 nm in the lateral x,y directions can be reached. In the vertical direction, the achievable resolution is down to 0.01 nm because of the exponential distance dependence of the tunnelling current.[PLW12]

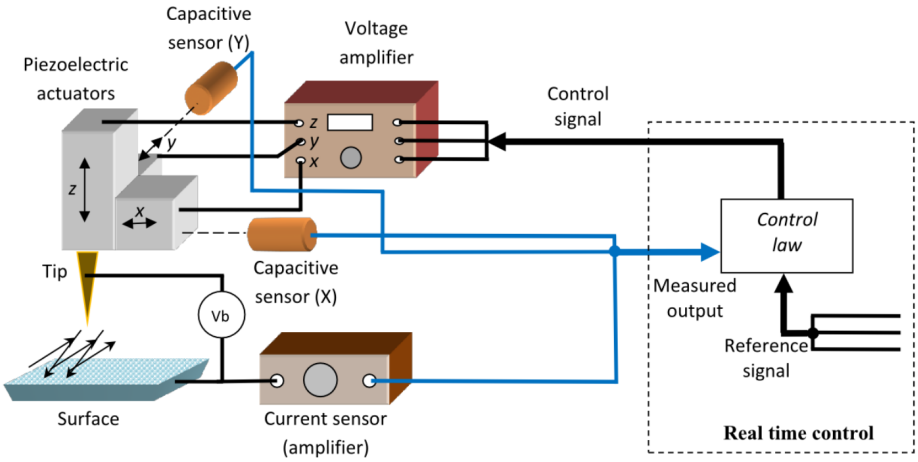

Figure 2.19.: Scheme of an STM setup. Piezoelectric actuators are used to move the probe in x,y,z direction. A bias voltage is applied between the tip and the conductive sample. The piezo position is controlled by a feedback system that processes the information gained from the current sensor. Image reprinted from [Ryb15] under CC license.

An STM can be operated in an electrochemical environment. It is then referred to as electrochemical STM (EC-STM), which is a crucial part of the TERS system that is used and discussed in chapter 4 of this thesis.

2.2.5 Electrochemical STM

Electrochemical scanning tunneling microscopy (EC-STM) is the application of STM in an electrochemical system. The EC-STM method was first presented by Liu[Liu+86]. The application of STM to electrochemical environments allowed the study of electrified solid-liquid interfaces in situ with atomic resolution in real space.[GN97; Ita98]
EC-STM experiments are performed in cells that expose the sample surface and the tip apex to the working electrolyte in a four-electrode setup, with the tip and sample as two independent WE, a CE and RE connected to a bipotentiostat that can independently control the WE and tip potentials.
The independent control of the potentials of the two WE by the bipotentiostat allows

the application of a bias to enable tunnelling current and electrochemical reactions to occur. Therefore, it is important to keep the potential applied to the tip in a range where the tip is electrochemically inert to obtain reproducible results and not to destroy the tip. The functions of CE and RE are analogous to the three electrode setup described in the section about cyclic voltammetry.
The measured tunnelling current between tip and sample is superimposed by an electrochemical, (non)faradaic current I_E, so that an accurate measurement is only possible if I_E is minimized. This is possible by electrically insulating the tip from the electrolyte so that only the tip apex remains conductive. Optimally, the remaining surface area of the tip in contact with the electrolyte is in the range of 10^{-8} cm^2. This reduces I_E, the leakage current, to values in the range of few pA.[PLW12] Thus, I_E is smaller than the tunnelling current, which is of the order of a few nA.
The setup used for the work discussed in this thesis is part of the EC-TERS setup and is therefore subject to limitations in size and positioning of parts of the setup. The EC-STM (Keysight Technologies GmbH STM 5420) is equipped with a bipotentiostat to control the WE and the tip independently during the experiment under electrochemical control. The STM scanner (N9700C) was modified with an extended tip holder to be able to hold the long Au tips (1 to 1.5 cm) that are used in our experiments. The relatively long tip size is needed because of the space restrictions of the EC-TERS setup and the resulting large distance between scanner and sample surface. The EC-STM is placed on an x-y stage (Steinmeyer Mechatronik GmbH) that provides a step precision of 3 nm at a maximum range of 10 mm. The system is located on an optical air table (Technical Manufacturing Corporation) to provide stability of the system. The EC-STM experiment is run in a cell designed for EC-TERS experiments that is described in detail in section 2.2.6. The cell made of Kel-F® holds a sample with a diameter of 10 mm (4 mm height) and provides holes to attach a CE and a RE to the cell. The Au tips are electrochemically etched prior to the experiment to provide TERS enhancement and a well-defined tip apex to obtain good quality STM capability. A high (EC-)STM resolution requires an atomically sharp tip, since unevenness of the sample would allow tunnelling over different atoms of the tip, depending on its surface structure, which would lead to artifacts in the imaging. For the etching, a Au wire of 1.5 cm length is brought vertically through the center of a ring-shaped Au wire counter electrode into a 1:1 solution of fuming HCl and EtOH, so that the tip is immersed by about 2 mm into the solution. The tip is etched by the application of a voltage of 2.4 V between the tip and the ring-shaped electrode. After the etching process, the tips are coated in Zapon wax (Clou) for electronic isolation. The tip is pulled vertically through a Zapon-covered gold wire bent into a U-shape so that the wire is covered with Zapon wax but the tip apex remains free. The experiments are performed in electrolyte with a hydrogen-loaded Pd wire (0.5 mm diameter, 99.95% metal basis, Mateck) RE (Pd/H). A Au wire (0.5 mm diameter, 99.995% metal basis, Alfa Aesar) is employed as CE. Both electrodes were washed in MilliQ and flame-annealed in a bunsen flame prior to the experiment. The EC-STM setup is controlled by PicoView software (Keysight Technologies GmbH).

2.2.6 Tip-enhanced Raman spectroscopy

The idea of scanning an Ag nanoparticle, which serves as an optical antenna to amplify an optical Raman signal, over a sample was proposed by Wessel in 1985. He wanted to overcome the limitations of surface-enhanced Raman spectroscopy (SERS) that relies on the amplification of a Raman signal by hotspots localized on the surface of a roughened metal sample. To control the sample-to-tip distance, he proposed to raster a metal tip in the sense of an STM at tunneling distance over the sample, where it would serve as a field amplifier.[Wes85] The idea was not realized until 15 years later, in 2000, by Zenobi and others.[Sto+00; And00; Hay+00]
TERS makes use of a metallic (or metal-coated) tip that is illuminated with a monochromatic laser beam and acts as an optical antenna to enhance and localize the incident electromagnetic field.

The combination of SPM with Raman spectroscopy provides the possibility of simultaneous collection of chemical and topographic information of a surface area with exceptionally high resolution and surface specific sensitivity. In TERS, a sharp metallic SPM tip is placed close above a sample. A laser is focused on the apex of the tip. The electromagnetic field is enhanced and localized in a small area, allowing the detection of a few molecules by an enhanced Raman signal.
The detection of molecules on the surface (adsorbates) requires an enhancement of the Raman signal. Two different mechanisms of different strength lead to an overall amplification of the Raman signal. The first, and stronger, mechanism is the enhancement of the electromagnetic (EM) field. This mechanism contributes in the order of up to 10^7 - 10^{10} to the overall enhancement of the Raman signal and is based on the excitation of localized surface plasmons (LSP) by the electromagnetic radiation in the visible spectrum.[LE09]
The second and weaker effect is the chemical enhancement by charge transfer (CT), which increases the total enhancement by one to two orders of magnitude.[DZP06; LE09]

In the following, we will take a closer look at the stronger effect of the EM enhancement. As written before, EM enhancement is based on resonant excitation of LSP. Plasmons are quasi-particles that represent the collective periodic oscillation of the free electron gas (plasma) in a metal. LSP are plasmons confined to a small part of the interface between a metal and a material with positive dielectric constant.[AH12]
The resonant excitation of surface plasmons is subject to limitations, which will be discussed in the following.
To resonantly excite LSP, an incident wave with a frequency corresponding to the frequency of the LSP is required. For the case of a metallic tip, only the LSP of the coinage metals silver and gold can be resonantly excited in the visible spectrum.[Hua+15] The exact resonant frequency depends not only on the material of the tip, but also on its

tip radius. Figure 2.20 shows the larger EM enhancement at smaller tip radius for a system with gold tip and gold sample.[Hua+15]

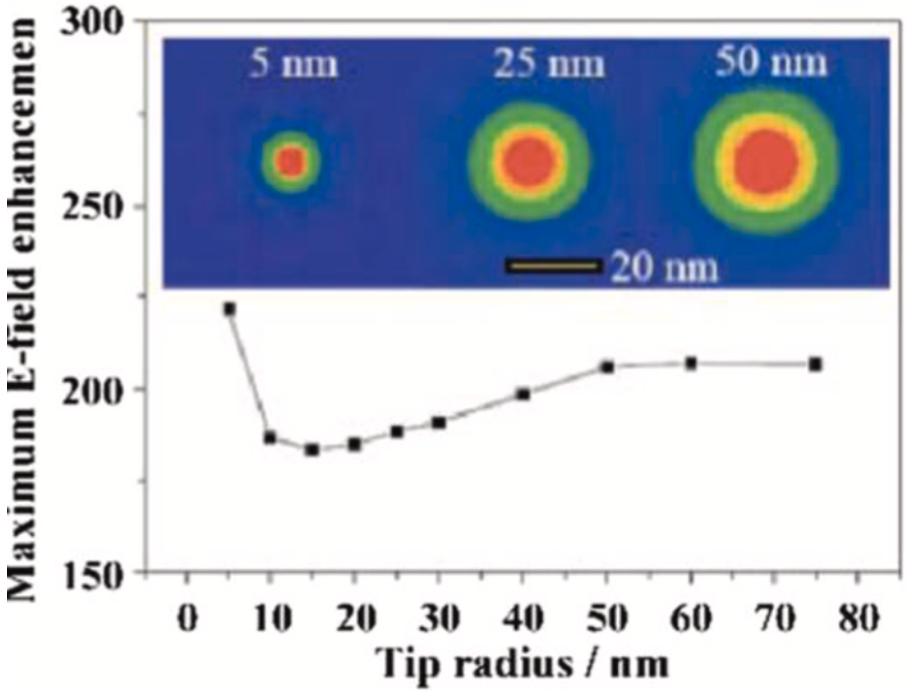

Figure 2.20.: Effect of the tip radius of a Au tip closely approached to a Au surface and illuminated with a laser focused on the tip apex on the enhancement of the EM field. Image reprinted from [Hua+15]. Copyright 2015, with permission from Springer Nature.

Besides the required matching frequency of the incident light, the excitation of the LSP requires momentum conservation. Simultaneous energy and momentum conservation is impossible in the case of smooth, finite metal surfaces.

Figure 2.21 shows the missing intersection between the linear energy momentum relation of light (black) and the distribution of surface plasmons (dashed purple). The localization of LSP to a restricted geometry provides the required momentum and thus allows the coupling of an external EM wave.[AH12] The additional momentum results in a set of LSP modes that can couple with the incident light, which is shown in figure 2.21 as a red dot with a dashed line. Nanostructures that allow excitation of LSP by light are called optical antennas. In the case of TERS, the metallic tip is an optical antenna that allows transformation of electric radiation from far-field to near-field. The enhancement of the EM field occurs only in a very small range in the order of a few nm as it decays exponentially with increasing distance. The enhancement factor $\mathrm{g_{inc}}$ of the incident light can be expressed as $\mathrm{g_{inc}} = \mathrm{E_l}/\mathrm{E_i}$, with the field strength of the local EM field $\mathrm{E_l}$ and the field strength of the incident EM field $\mathrm{E_i}$. Beside the incident light, also the EM field of the scattered light is enhanced. Assuming that the wavelengths of the incident laser and Raman scattering are similar, the total enhancement factor (EF) of the TERS signal compared to the conventional Raman scattering signal can be expressed as $\mathrm{EF} = \mathrm{g_{inc}^2} \cdot \mathrm{g_{sc}^2} = \mathrm{g^4}$.[NH11; MH14]

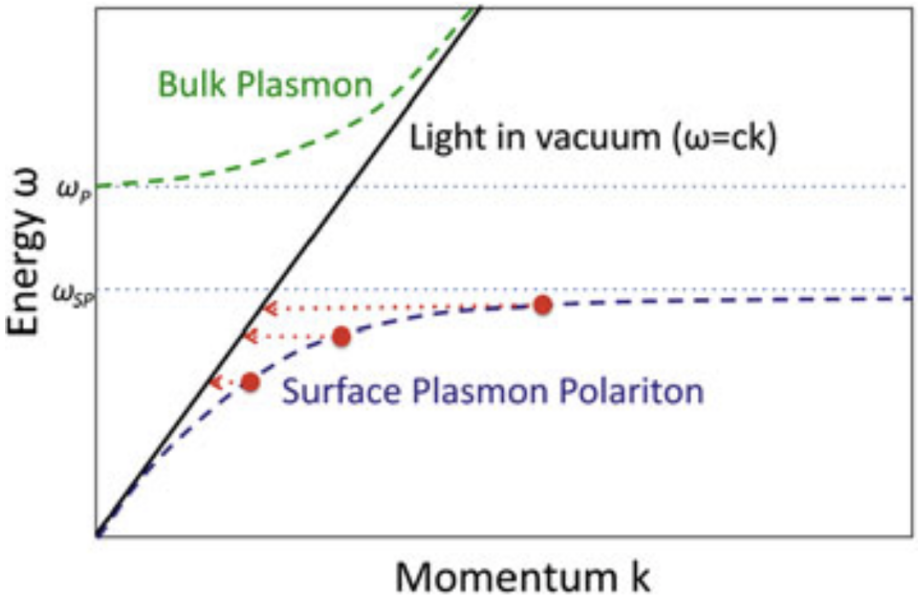

Figure 2.21.: Dispersion curves of the bulk (green dashed line) and surface plasmons (purple dashed line). The line of light in vacuum is represented as black line. The red dots and dashed lines show the additional of momentum that would allow for coupling of the incident light with the surface plasmon. Image reprinted from [AH12]. Copyright 2012, with permission from Springer Nature.

With the possibility to move the TERS tip over the probed surface with use of STM control, nm chemical spatial resolution and atomic topographic resolution can be achieved with high spectral resolution over a wide range of a surface.[DP10; Kur16] The lateral and vertical resolution is discussed in detail in the following section. As a Raman spectroscopy method, TERS is chemically sensitive and the combination with STM allows to simultaneously probe for topographic surface information. Moreover, the combination with EC-STM allows for studying not only surfaces in vacuum and ambient conditions, but also under *operando* conditions in an electrochemical cell (EC-TERS).[Sch+09; Zen+15; KMV15; Mar+17]

2.2.6.1 Spatial Resolution of TERS

In general, the lateral resolution is the minimum distance between two objects that can be distinguished from each other. The lateral resolution of conventional optical far-field microscopes is limited by the diffraction limit of the light used and was described by Ernst Abbe in 1873 and is called the Abbe limit. The Abbe limit gives the minimum distance between two resolved points as $\mathrm{d} = \lambda/2\mathrm{NA}$, with the numerical aperture NA and the wavelength of the used light λ.[Cre11] In the case of self-luminous points, as in classical fluorescence microscopy, the Rayleigh criterion gives the resolution limit of $\mathrm{d} = 0.61\lambda/\mathrm{NA}$, with the wavelength of the emitted light λ and the numerical aperture

NA.[Cre11] The Rayleigh criterion is fulfilled if the maximum of the intensity of one diffraction disc of the self-luminous points falls into the minimum of the other one. With that, conventional far-field optical microscopy cannot overcome a resolution limit of approximately 200 nm in the visible spectrum.
In contrast to far-field optics, near-field optics offer a much higher theoretical lateral resolution. TERS, as a near-field Raman spectroscopy technique allows to overcome the classical resolution limit of the far-field. The lateral resolution of TERS is determined by the extent of the near field on the sample surface. In the simplest approximation of the field distribution by means of a Heaviside function (a function which for x<0 has the value 0, for x≥0 the value 1) results in $\mathrm{r_{TERS}} = \mathrm{r_{EM}} = \mathrm{r_{tip}}$, with the lateral resolution of TERS $\mathrm{r_{TERS}}$, the lateral expansion of the EM field $\mathrm{r_{EM}}$ and the radius of the used tip $\mathrm{r_{tip}}$.[Pet+05] The more realistic assumption of a Gaussian distribution of the field that does not end sharply, gives a lateral resolution of $\mathrm{r_{TERS}} = \frac{1}{2} \cdot \mathrm{r_{tip}}$.[Pet+05] Assuming a peak radius of 20 nm, as seen in earlier SEM experiments[Pfi19], this results in a lateral resolution of 10 nm.[Pet+05] Experimental results show that a lateral resolution of 10 nm or better has been obtained in numerous studies under ambient conditions as well as under *operando* conditions (EC-TERS).[Ric+17; SSZ10; SP08; Pfi+19] In addition, studies have shown exceptionally high resolutions <5 nm in the gap-mode configuration, i.e. with a metallic tip and metallic substrate.[Zha+13; Lee+19] In the gap mode configuration, the tip is moved very close (approx. 1 nm) to the sample. Laser excitation induces a dipole in the tip, which forms a mirror dipole in the metallic surface.[Hay01] The superposition of the field components of the dipoles leads to an amplification and further confinement of the EM field, which leads to an increase of the possible resolution of TERS.[Hay01; Dom06; Shi+17] Thus, TERS is able to provide chemical and topographic information combined during the experiment with a chemical resolution in the range of a few nanometers and down to atomic topographic resolution under UHV and ambient conditions as well as under *operando* conditions with potential control.[Ric+17; SSZ10; SP08]

The vertical TERS resolution is determined by the vertical extent of the near field. Studies have shown a vertical distance dependence inversely proportional to s^{10}, with distance s between the tip and a 2D sample surface.[Pet+05] The strength of the EM field enhancement of an oscillating dipole decreases inversely proportional with the 3rd power of the distance s to the dipole.[KB82] As described before, the total enhancement of the TERS signal is proportional to the 4th power of field enhancement. Thus, after integration over the observed surface, the distance dependence is inversely proportional to the 10th power of the distance between the tip and the sample surface.[Dom06; Pet+07; Pet+09; Max+12]

2.2.6.2 EC-TERS

To run EC-TERS, a bipotentiostat is needed to control the tip potential independently of the WE potential, as described previously for EC-STM (2.2.5). The EC-TERS cell design that is used throughout the TERS experiments in this thesis is shown in figure 2.22. The cell is made out of Kel-F® to avoid chemical interactions with the probed

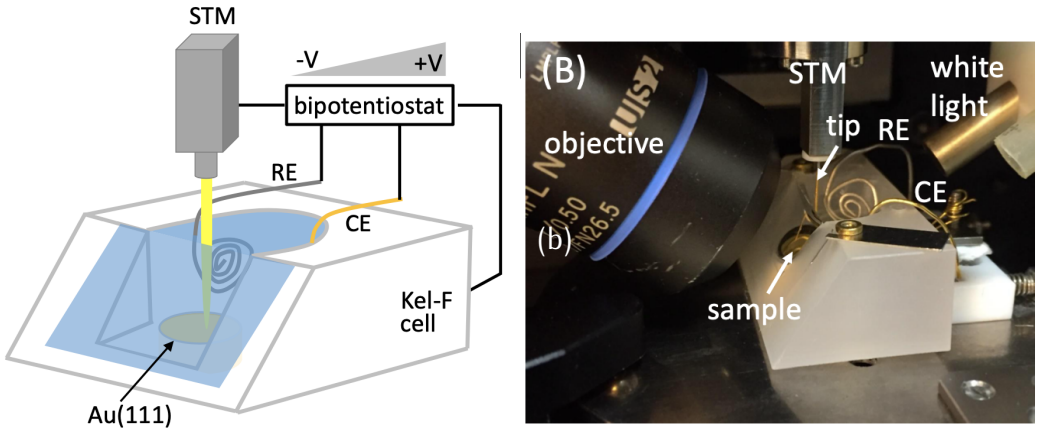

Figure 2.22.: In-house designed (EC-)TERS cell made out Kel-F®. The cell allows for holding of a CE and RE, together with a round, single crystal WE (Diameter: 1 cm). The glass window on one side allows for side illumination at 55°angle. Images adapted from [Pfi19]

material. The cell holds CE and RE wire electrodes and a cylindrical single crystal WE of 1 cm diameter. One side of the cell is closed with a glass window (thickness 170 µm) at an angle of 55° for side illumination of the sample. The glass window is glued to the Kel-F® body with UV glue (Loctite 3321). After each experiment, the glass slide is removed by boiling in acetone and is exchanged by a new glass slide. The cell is open at the top so that the tip can approach the sample surface.
The EC-TERS setup that is utilized in the experiments throughout this thesis is STM-based and home-built. The specifications of the EC-STM (Keysight Technologies GmbH) were described previously in the EC-STM section (Section 2.2.5). A red HeNe Laser (Research Electro Optics Inc. REO LSPR 3501, 632.8 nm, maximum output power: 35 mW, p-polarized beam) is focused onto the Au-tip apex, after reducing the power to approx. 5-8 mW with gray filters (Filter wheel FW212C, Thorlabs), which is then additionally lowered to about 2 mW due to optical abberations at the glass/electrolyte interface. The laser is focused through a 50x long working distance objective (Olympus, working distance: 10.6 mm, NA: 0.5) at an angle of 55° relative to the surface normal. The TER scattered light is collected through the same objective in backscattering configuration. The detection path involves a dichroic long-pass beam splitter (RazorEdge Dichroic LPD02-633RU-25, Semrock) and subsequently a long-pass filter (RazorEdge ultra long-pass edge filter LP02-633RE-25, Semrock) with cut-off values of 156 and 79 cm^{-1}, respectively, to filter out the elastic scattering. The low filter cut-off value allows to record TER spectra in a wide spectral range

between 156 and 4000 cm^{-1}. A spectrograph (Horiba iHR 550) equipped with three gratings (600, 1200, 1800 lines/mm) and a liquid nitrogen cooled CCD camera (Horiba Symphony II) is used for detection of the TER scattered light. To obtain maximum spectral resolution, the 600 lines/mm grating is used in the experiments reported throughout this thesis.
To allow for focusing, the STM is placed on an x,y piezo stage, while the objective can be moved in z-direction. Moreover, a CMOS camera (Mikrotron MC 1362) can be (temporarily) used by introducing a beam splitter into the beam path with white light illumination to follow the focusing of the laser in the white light image.
The tip-sample distance is controlled with the STM by applying a current setpoint and tip-sample bias voltage, chosen in a way to obtain TERS enhancement and STM imaging with low noise level.
In this thesis, EC-TERS is used to show the presence of a poisoning species during the electrooxidation of formic acid on a Pd@Au(111) system under *operando* conditions (Chapter 4).

2.2.7 Fluorescence Microscopy

In most cases, fluorescence microscopy methods make use of the fluorescence of dye molecules to obtain contrast and produce images of the fluorescence labeled specimen. The specimen is illuminated by an intense and monochromatic light source (eg. a laser) through an objective. The incident light is absorbed by the fluorophor and induces emmitance of photons due to fluorescence relaxation of the excited states. The emitted photons show a Stokes shift compared to the incident photon frequency and are measured by a detector to produce the fluorescence image.
Most conventional fluorescence microscopy setups are wide-field epifluorescence microscopes. In this configuration, the specimen is illuminated over the entire focal plane and the resolution is limited by the Abbe limit. The excitation and collection of emitted photons uses the same objective. Figure 2.23 shows the schematic of a epifluorescence microscope.

After being focused to the detector by the objective, the emitted light passes the dichroic mirror. The remaining photons with excitation wavelength are filtered before the emitted photons reach the detector.

Many methods have been developed to overcome the resolution limit of fluorescence microscopes, such as confocal microscopy, total-internal reflection microscopy, stimulated mission depletion microscopy and others. In the work presented in this thesis, a conventional epifluorescence microscope is used to obtain wide-field images of the sample.

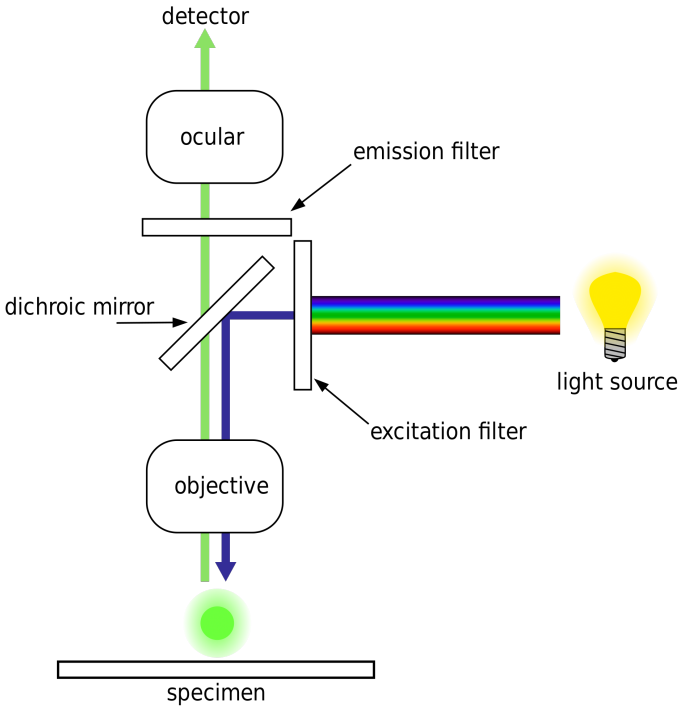

Figure 2.23.: Scheme of a conventional epifluorescence wide-field microscope. The excitation light illuminates the specimen through an objective. The fluorescence light is collected in reflectance through the same objective. The emitted light passes a dichroic mirror, is filtered from the excitation light by a filter and measured on a detector. Image reprinted from [Com] under CC license.

Part III

Hydrogen Evolution Reaction on confined space catalysts

3

Hydrogen Evolution Reaction on confined-space catalysts

The chapter is about the studies on Hydrogen Evolution Reaction on 2D confined platinum group metal nanoislands on Au(111)

Contents

This chapter is reproduced from the publication 'Daniel Ohm, Katrin F. Domke, *Controlled deposition of 2D-confined Pd or Ir nanoislands on Au(111) following Cu UPD, and their HER activity*, J. Electroanal. Chem., 896, **2021**, p. 115285'.[OD21]

The rational design of electrocatalysts with the aim to achieve highest catalytic activity for specific reactions is a major task in the field of electrochemistry today. One aspect of this rational design is to achieve high mass activity of a catalyst to reduce material of cost-expensive and rare metals such as the metals of the platinum group (PGMs). Here, we introduce a two step mechanism to produce 2D-confined PGM nanoislands on a supportive Au(111) layer via Cu UPD and subsequent galvanic displacement of Cu by the desired PGM, in our case Pd and Ir, respectively. We probe the island properties such as island size, inter-island distance and border length of the islands as functions of the applied potential during Cu UPD and the duration of the applied potential during Cu UPD. We observe a strong dependence of the island properties on both Cu UPD parameters that were varied in this study. Even though there is a maximum overall PGM surface coverage of 0.33 ML at the potentials that were applied, the island distribution and size increases with UPD duration and also with potential. The applied potential during Cu UPD has great influence on the number of nuclei formed in the early phase of the UPD. The transferred current during the duration of Cu UPD leads to growth of these nuclei to islands.
The following chapter focuses on the influence of the island properties on the catalytic activity of the catalysts for Hydrogen Evolution Reaction (HER) catalysis.

3.1 Introduction

The challenge to run electrochemical energy conversion reactions at low cost and high efficiency requires advanced catalyst materials. The requirements to these materials are availability, low costs and high activity. For reactions such as hydrogen evolution/reduction (HER/HRR) or oxygen evolution/reduction (OER/ORR) reactions, platinum group metals (PGMs), i.e. Pd, Ir or Pt, are well established catalyst materials.[EC11; Rak+18; CJ15] One key for cost and material efficiency of catalysts is to maximize the mass activity, which is defined by the the specific catalytic activity of a material for a given (electro)catalytic reaction normalized to the surface area, and, in turn, normalized to the amount (mass) of a catalytically active material.[Li+16a] One way to increase the mass activity of a catalyst is to find a submonolayer of catalytically active material on a supporting material that has high activity for a given reaction. Here, we study Pd and Ir nanoislands on a Au(111) layer. Pd submonolayer deposited on Au(111) are one of the most widely studied systems.[SP18] Different ways for Pd submonolayer deposition from solution onto Au(111) has been reported. One way to produce Pd nanoislands is direct underpotential deposition from Pd-salt solution. The resulting islands grow to irregularly shaped triangles at underpotential prior to forming

multilayers at overpotential.[Kib+99; Tan+05] Another method is the spontaneous deposition of Pd from salts, that also lead to island-like structures.[Smi+12] The group of Feliu found a correlation between the activity of such island-like catalysts and the way they were prepared.[Mel+18] They found that specifics such as applied potential or the presence of hydrogen atmosphere play a crucial role during the Pd deposition towards the resulting catalytic activity. Besides the preparation method, the number of Pd sites influences the activity of the catalyst. Pandelov and Stimming showed that, counter intuitively, the activity of a Pd submonolayer catalyst increases with decreasing number of Pd islands on the surface and decreasing layer thickness.[PS07] They found that the rate of HER is enhanced by up to two orders of magnitude by Pd submonolayers with an island size down to <5 nm for partial Pd coverages down to 0.035 ML. They explain this effect by a spillover of intermediates onto the Au(111) surface. Bulk protons diffuse to the Pd layer where they get adsorbed and discharged, which is a fast step on Pd. On a full Pd monolayer, the rate determining step of HER is the hydrogen recombination and desorption. On Pd islands, adsorbed and discharged H_{ads} is spilled over onto the Au(111) surface where it recombines to form molecular hydrogen. A dependence of the number of Pd edge sites versus terrace sites on the current density of HER could not be found. Nørskov and co-workers however found the importance of Pd rim sites on the catalytic activity in their work on the influence of Pd surface coverage on HER.[Bjö+11]

Here, we focus on a two step routine to form Pd and Ir islands on Au(111). Our route toward 2D nanoislands bases on Cu UPD and subsequent galvanic displacement from Pd or Ir salt solution. This method is similar to the method published by Adžić and co-workers.[BWA01] Cu UPD is a well-established technique to form regularly distributed Cu islands on bulk metal electrodes at underpotential.[Mag+90; HMB95; UHW98; HBA01; Her+99] The primary advantage of this two step route is the separation of island formation (via Cu UPD) and displacement with the target metal. In principle, with our method, it is possible to displace the Cu islands with any more noble metal. Therefore, no special route for each desired target metal needs to be developed. Moreover, islands prepared in the same way during Cu UPD can later be displaced by various other noble metals so that a comparison of the catalyst materials independent of the island properties is possible. With the two step pathway it is possible to tune the island size between 2 and 40 nm diameter by the choice of Cu UPD potential and duration. The resulting Pd/Au(111) and Ir/Au(111) catalysts are evaluated with respect to their activity to catalyze the HER.

3.2 Experimental details

The PGM island catalysts were prepared on Au(111) thin films on glass slides. The Au thin films were prepared by thermal evaporation of Au beads (4N) on N-LaSF9 glass slides that were covered by a 5-10 nm thick Cr layer to increase the adhesion of the Au layer. The evaporation was performed with an Edwards FL 400 evaporator. The evaporation rate was 0.05 nm/s at a pressure of $<5 \cdot 10^{-6}$ mbar. The thickness of the Au layer is 150-200 nm. The Au/glass slides were cleaned before use by rinsing with MilliQ water (Millipore, 18.2 MΩ, 3 ppb TOC), immersion in 40% HNO_3 (Suprapur, Merck) for 2 minutes and subsequent rinsing in MilliQ. The glass slides were flame-annealed prior to the use in the electrochemical cell. The slides were glowed to red multiple times for few seconds with a Bunsen burner flame to avoid melting of the Au layer or the glass slide. After the annealing, the sample was carefully rinsed with MilliQ water. After the rinsing, a Au wire (Merck, diameter: 0.5 mm, 99.997% trace metal basis) was attached to the sample for contacting. A teflon tape (Hightech-flon, thickness: 0.13 mm) with a hole (diameter 6 mm) was sticked onto the sample to provide a well-defined surface area of the electrode.

Cyclic voltammetry measurements were performed with a Metrohm Autolab PGSTAT30 Potentiostat with a Metrohm Autolab Differential Electrometer Amplifier attached. NOVA (Version 2.1, Windows 7) was used as software for the electrochemical measurements. The samples were attached as working electrodes in a three-electrode configuration in a H-Cell with an electrolyte volume of 50 mL. An Au wire was used as counter electrode. The reference electrode was prepared by hydrogen loading of a Pd wire (0.5 mm diameter, MaTecK, 99.95% metals basis). The loading of the reference electrode was carried out in 0.1 M H_2SO_4 (Suprapur, Merck) and 10 V of applied potential between the Pd wire and an Au counter electrode until the gas evolution of hydrogen evolution at the Pd electrode corresponded roughly to the oxygen evolution at the counter electrode. If not noted otherwise, the potentials in this study are converted to and reported versus SHE.

Cu UPD was carried out from freshly prepared 1 mM $CuSO_4$ solution in 0.1 M H_2SO_4 that was used as electrolyte. All Cu UPD experiments were done using the same experimental conditions, besides from varying the applied potential or duration of the UPD. Prior to the start of the experiment, Ar (6.0 Westfalen) was bubbled through the electrolyte for at least 10 minutes. During the experiment, the electrolyte was blanketed with Ar. The immersion potential of 0.5 V vs Cu/Cu^{2+} was held for 15 s prior to jumping to the UPD potential in all experiments. After the system reached equilibrium, the target potential of 0.12 or 0.15 V Cu/Cu^{2+} (0.44 and 0.47 V vs SHE) was set for the desired duration before switching to open circuit potential. The cell was shut off, the

sample was removed and briefly rinsed in MilliQ water before the galvanic displacement.

10 mM aqueous solutions form $PdCl_2$ (99%, Merck) and H_2IrCl_6 (99.8% trace metals basis, Merck) in 10 mM HCl were used for galvanic displacement. The samples were rinsed in MilliQ after the Cu UPD, then directly immersed into the respective solution for 10 s and subsequently rinsed carefully with MilliQ water.

Tafel plots were derived from polarization curves in a potential window from -0.2 V to +0.2 V vs SHE. The curves were recorded at a scan speed of 25 mV/s versus a H_2-loaded Pd reference electrode and an Au wire counter electrode. log|j| was plotted versus the overpotential in the linear regime of the polarization curve and linearly fitted to obtain the Tafel constant (HER onset potential) and Tafel slope.

3.3 Experimental results

3.3.1 Platinum group metal deposition via Cu UPD

Figure 3.1a shows a typical current-time trace recorded during the Cu UPD on Au(111) probes. The current density decreases strongly at short time scale. At the very beginning of the underpotential deposition, a current density of -400 $\mu A/cm^2$ is measured. After a short period of 1s, the current density decreased to -50 $\mu A/cm^2$. With longer deposition duration, the current density converges to 0 $\mu A/cm^2$.

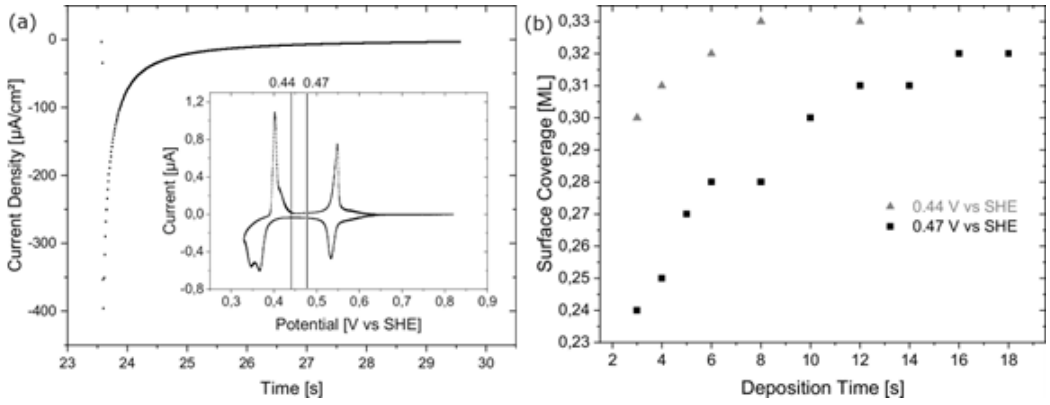

Figure 3.1.: (a) Typical current-time trace recorded during Cu UPD. The first 23.5 s, the potential is set to 0.85 V vs SHE to equilibrate the system. Inset: Cu UPD on Au(111). The lines indicate the chosen potentials for Cu UPD experiments. Both potentials are less positive than the first reduction peak but more positive than the second reduction peak. (b) Calculated surface coverage as function of the Cu UPD duration for both potentials. The surface coverage was calculated from the respective current-time traces for each sample. Image reprinted from [OD21] under CC license.

The surface coverage shown in figure 3.1b was calculated from the integrated current density during the underpotential deposition. The charge that is needed to deposit one monolayer (ML) Cu onto a Au(111) surface was calculated by integration of the current density of the UPD peaks shown in the inset of figure 3.2a to be 0.45 μmC/cm^2. The values reported in literature are in a range between 0.35[Shi+95] and 0.46 μmC/cm^2.[HHI91] At lowest Cu UPD durations, a minimum Cu surface coverage of 0.24 ML (deposition at 0.47 V vs SHE) and 0.30 ML (deposition at 0.44 V vs SHE) is obtained, respectively. The surface coverage increases independently from the UPD potential and reaches a plateau after 16 s (0.47 V) and 8 s (0.44). The plateau value for depositions at 0.47 V is reached at 0.32 ML, whereas the deposition at lower potentials of 0.44 V leads to a maximum coverage of 0.33 ML, which is in agreement with the maximum theoretical value of Cu surface coverage at given potentials derived from the Cu UPD peak ratio.[Zei+87]

The coverage difference resulting from the two deposition potentials is high at short deposition durations. At 3 s, the difference between 0.47 V and 0.44 V vs SHE is 0.06 ML (20%). To reach a surface coverage of 0.30 ML at a potential of 0.47 V vs SHE, a deposition duration of 10 s is needed. The results show that the dependence of the surface coverage on the deposition potential is much greater than the one on the deposition duration. This fact can be understood based on the current-time trace shown in 3.1a. The initial current density, which is potential controlled (among other properties like surface condition that are not part of this study), vanishes quickly with time and reaches values of less than 25% of the initial current density after 1 s. At 3 s, which corresponds to the first datapoint in 3.1b, the initial current density has lowered to a value of less than 5% of the initial current density. Deposition durations longer than 3 s contribute with small charge densities to the total transferred charge, compared to the initial 3 s.

Similar to their effect on the total PGM surface coverage, Cu UPD potential and duration also play a role to control the resulting island size and distribution. Figure 3.2 shows two current-time traces recorded during Cu UPD at 0.44 and 0.47 vs SHE, respectively. The initial current density at a potential of 0.44 vs SHE is $-9.8 \cdot 10^{-5}$ μA/cm^2. At a more positive deposition potential of 0.47 V vs SHE, the initial current density is only $-7.8 \cdot 10^{-5}$ μA/cm^2, 20.4% less than at 0.44 V Cu UPD potential.

The current density decay with time is a little larger at more positive potential compared to the lower deposition potential. After the first 0.5 s of deposition, the current density decays to $-1 \cdot 10^{-5}$ μA/cm^2 at 0.47 V. At 0.44 V, the current density after 0.5 s decayed less to $-1.5 \cdot 10^{-5}$ μA/cm^2. After 2 s, the current density is equal at both potentials. These findings show, that at the initial time of the Cu UPD, at lower potentials, more charge is transferred into the system, leading to a significant higher surface coverage. At longer durations of the Cu UPD, the transferred charge for both potentials equalizes. That means that the island growth rate at longer durations is equal for both potentials that were subject of this study.

An important aspect of island fabrication following a two-step route via Cu UPD and subsequent displacement is the stability of the intermediate Cu islands after Cu

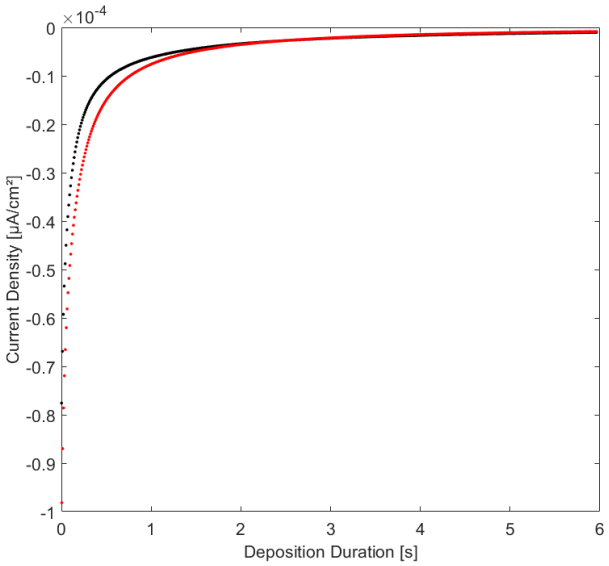

Figure 3.2.: Two typical current time traces for Cu UPD potentials of 0.44 V and 0.47 V vs SHE, respectively. The black curve shows the trace recorded at 0.47 V vs SHE. It has a maximum current density of $-7.8 \cdot 10^{-5}$ µA/cm^2 which quickly decays to $1 \cdot 10^{-5}$ µA/cm^2 after 1 s. Red curve shows the current-time trace at 0.44 V vs SHE. The maximum current density at the initiation of the deposition is $-9.8 \cdot 10^{-5}$ µA/cm^2.

UPD in air and after rinsing with water. Figure 3.3 shows ambient STM images of Cu islands without rinsing with MilliQ (3.3a) and after rinsing in MilliQ (3.3b). The images do not show significant differences in island shape, distribution and size after the two procedures and imaging under ambient conditions.

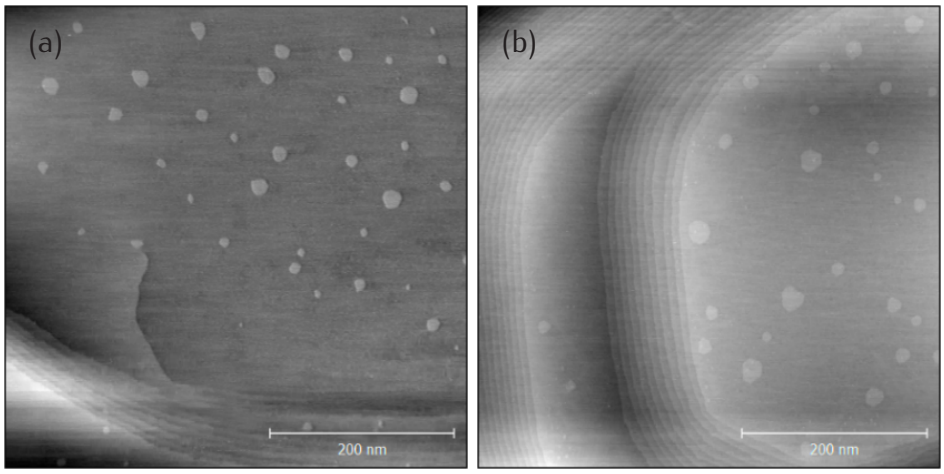

Figure 3.3.: Ambient STM images of Cu islands on Au(111) recorded after Cu UPD at the same conditions. Image (a) shows a sample that was not rinsed in MilliQ after the UPD. Sample (b) was rinsed carefully in MilliQ prior to imaging. Image reprinted from [OD21] under CC license.

Potential leftovers of Cu after the galvanic displacement process as well as the presence of Pd and Ir, respectively, was monitored by X-ray photoelectron spectroscopy (XPS). Figure 3.4a shows the full range (0-1200 eV) XP spectrum of a Pd/Au(111)

sample. It shows peaks at 58 and 84 eV that can be assigned to the Au-5p3 and Au-4f7 electrons.[ST] Furthermore peaks at 88.2, 285 and 337 eV are found. These are assigned to the Pd4s electrons, carbon and Pd3d, respectively.[ST] Figure 3.4b show the XP spectrum in the Cu2p3 range from 900 to 960 eV, where no peak can be found, which is in accordance with a complete displacement of the Cu with the respective PGMs during the galvanic displacement process.

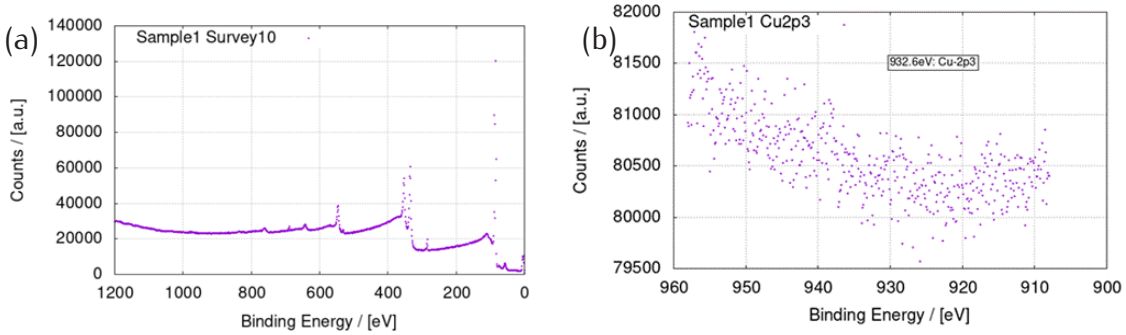

Figure 3.4.: (a) XP spectrum of Pd/Au(111) in the full range of 0 to 1200 eV. Peaks can be found at 58, 84, 88, 285 and 337 eV. (b) Small range XP spectrum in the Cu2p3 region from 900 to 960 eV. Image reprinted from [OD21] under CC license.

Figure 3.5 shows XP spectra recorded in the ranges of (a) 45-75 eV, (b) 70-95 eV, (c) 270-300 eV and (d) 320-350 eV. Figure 3.5a shows one clear peak at 57 eV associated with the Au5p3 electrons. Peaks at 84 and 88 eV that are assigned to the Au4f7 and Au4f5 electrons[ST], respectively, are found in (b). 3.5c and d show two peaks at 285 (C1s) and 337 eV (Pd3d), respectively.[ST] The XP spectra show no residues of Cu left on the samples within the detection limits of the XPS experiment Typical detection limits for XPS experiments are within 0.1 to 1 atomic percent.[Sha14] Moreover, Pd specific peaks are visible in the spectra at 337 eV. Figure 3.5e shows the XP spectrum of Ir/Au(111) from 45 to 75 eV. Compared to the Pd/Au(111) spectrum in 3.5c, 2 additional peaks at 62 and 64 eV are found and assigned to the presence of Ir (Ir4s and Ir4f5, respectively) on the sample.[ST]

The effect of the applied Cu UPD potential on the island properties is also evident in the STM images of the surface after Cu UPD and subsequent galvanic displacement of the Cu submonolayer with a PGM. Figure 3.6 shows ambient STM images recorded on a Au(111) surface after Cu UPD and subsequent galvanic displacement for 6 s at 0.44 V (a) and 0.47 V vs SHE (b), respectively.

The resulting submonolayer has the form of island-like structures. The Pd islands resulting from Cu UPD at 0.44 V are equally distributed and have an average island diameter of 3.4±0.5 nm. Figure 3.6b shows less uniform island distribution and larger islands with average diameter of 13.8±3.8 nm grown at a Cu UPD potential of 0.47 V vs SHE. The total PGM surface coverages at these Cu UPD settings are 0.32 ML (0.44 V) and 0.28 ML (0.47 V). Note that the CVs indicate a coverage between 0.24 and 0.33 ML for all experiments dependent on the respective applied deposition potential and duration while STM images only provide information over a small observation area,

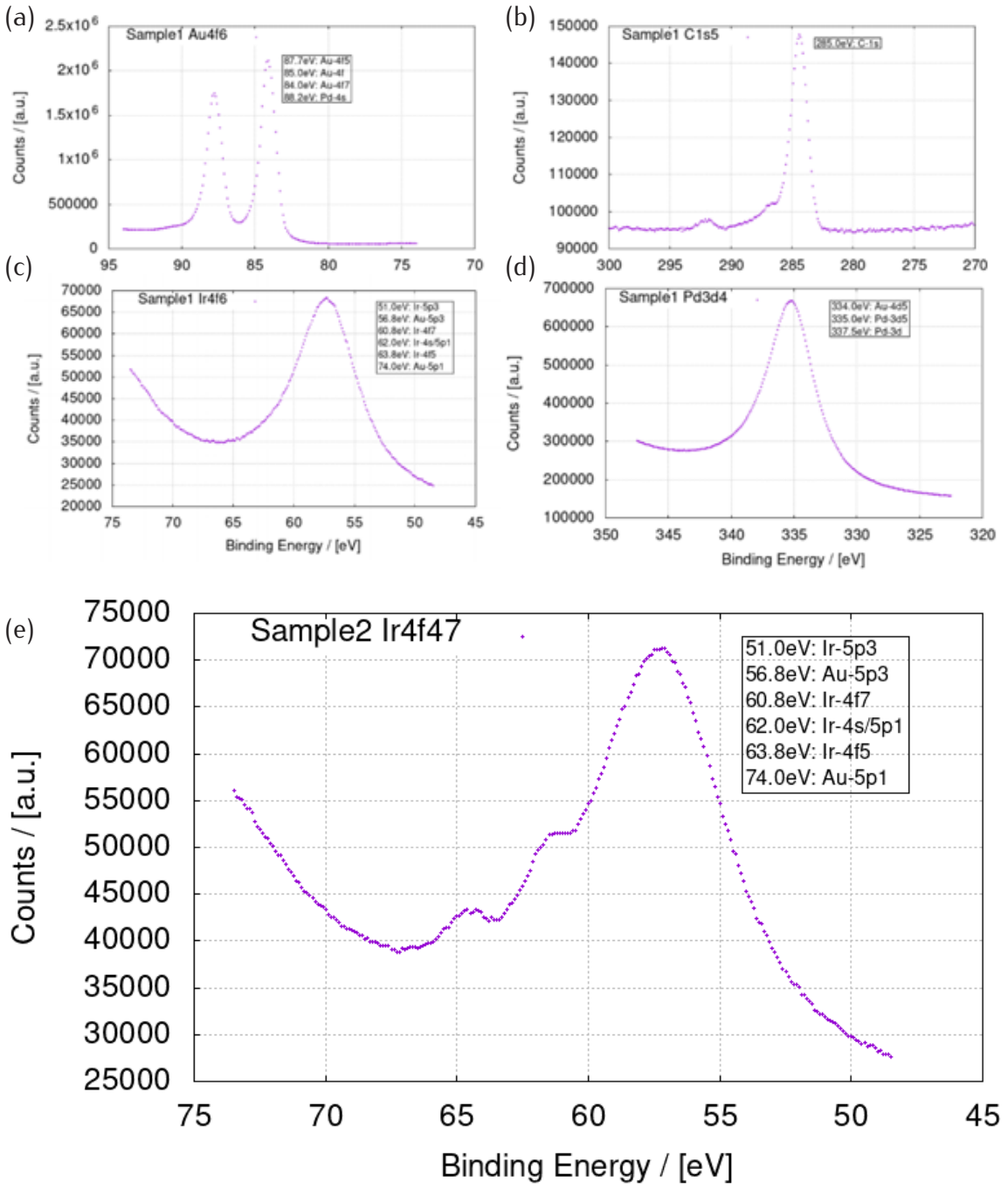

Figure 3.5.: Small range XP spectra of Pd/Au(111). Insets indicate relevant assignments for possible peaks in the range. (e) XP spectrum of Ir/Au(111) with additional peaks at 62 and 64 eV, that indicates the presence of Ir on the surface. Image reprinted from [OD21] under CC license.

which causes a variance in surface coverage that reaches from less than 5% to 65%, thus reaching values much higher than the theoretical maximum of 33%.

Figure 3.7 shows the Pd island size as a function of deposition duration applied during Cu UPD for both used potentials. The sizes were measured from STM images and show average values of multiple islands measured on different samples.

The trend shows an increase in island size with longer deposition durations. At

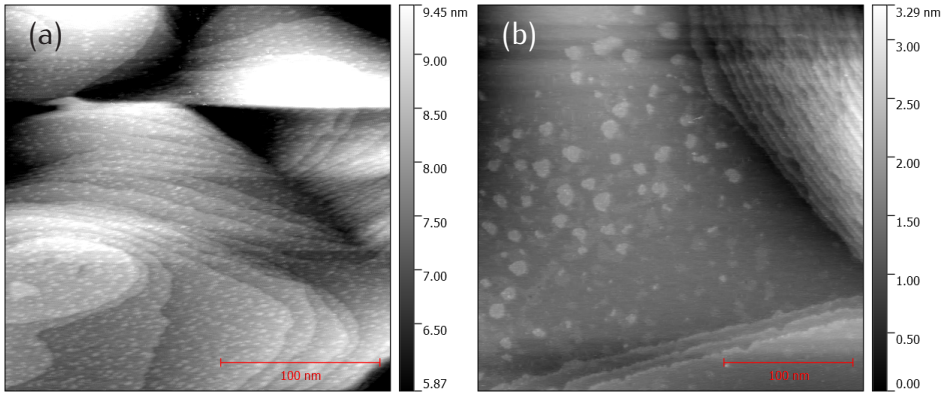

Figure 3.6.: Ambient STM images of Pd/Au(111). The Cu UPD potentials were chosen to be 0.44 V vs SHE (a) and 0.47 V vs SHE (b), respectively. With less positive deposition potential, the islands are distributed more uniformly and are smaller compared to deposition at a more positive deposition potential. Image reprinted from [OD21] under CC license.

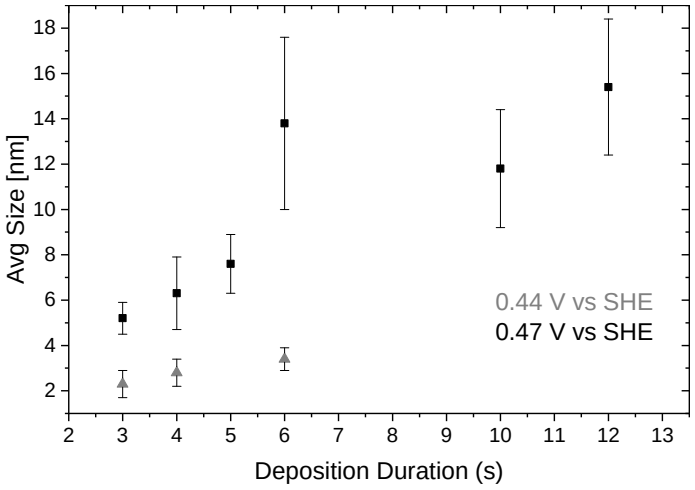

Figure 3.7.: Pd island size as a function of Cu UPD duration and potential. The average island sizes where obtained from STM image analysis. The average size increases with Cu UPD duration until it reaches a plateau after 6 s at 0.47 V vs SHE (black dots). The island size at 0.44 V increases linearly from 3 s to 6 s (grey triangles). Image reprinted from [OD21] under CC license.

short durations of 3 s, the STM images show average island sizes of 2.3±0.6 nm at 0.44 V and 5.2±0.7 nm at 0.47 V. The size increases for both potentials up to a deposition duration of 6 s, reaching sizes of 3.4±0.5 nm (0.44 V) and 13.8±3.8 nm (0.47 V), respectively. At a deposition potential of 0.47 V, the island size reaches a plateau after 6 s. It is evident that the size deviation is much smaller for smaller island sizes at lower Cu UPD durations and also smaller for the less positive deposition potential of 0.44 V vs SHE. At 0.44 V, the size deviation is small for all durations with standard deviations (SD) from the mean island size of less than 1 nm. At 0.47 V, however, the size deviation increases with deposition duration, leading to islands that are less uniform in size. At 3 s, the SD at 0.47 V is only 0.7 nm, comparable to the SDs at 0.44 V. After 6 s deposition, the island size SD is 3.8 nm for 0.47 V. The

island height is not influenced by the deposition duration. The sub-monolayer of Cu is always replaced by mono-atomically high PGM islands. The height of the islands is 0.33 nm, close to the atomic diameter of Pd of 0.34 nm.[80] For some samples, we also observe islands with smaller diameter compared to the surrounding islands with heights of about 0.1 nm. The height of Ir islands found to be 0.37 nm, which is slightly higher than the Ir atomic diameter of 0.36 nm.[80]

Another intrinsic property of a 2D confined island-like catalyst is the inter-island distance. This property can be extracted from STM images. The inter-island distances for Pd islands on Au(111) resulting from different Cu UPD conditions are listed in table 3.1.

Table 3.1.: Inter island distances and boundary lengths as functions of the Cu UPD deposition properties of resulting Pd islands on Au(111).

Deposition potential [V]	Deposition duration [s]	Inter island distance [nm]	Relative boundary length [$\mu m/\mu m^2$]	Island diameter [nm]
0.47	3	6.1	102.4	5.2
0.47	4	6.8	49.3	6.3
0.47	5	5.1	160.4	5.1
0.47	6	4.8	102.5	13.8
0.47	10	5.1	86.1	11.8
0.44	6	1.5	227.1	3.4

It can be noted that the inter-island distance resulting from a deposition potential of 0.47 V is in the range between 4.8 and 6.8 nm. At 0.44 V after a deposition time of 6 s, the inter-island distance is only 1.5 nm, which is less than half of the average distance of samples prepared at 0.47 V. At high deposition durations, the inter-island distance cannot be measured anymore, because the islands start to grow into each other and merge to larger islands, which can be seen in the average island diameter of a sample prepared over 14 s of Cu UPD, which is extraordinary large with a value of 68 nm. The relative length of boundaries per area strongly depends on the spot at which the STM image was recorded. In principal, the relative boundary length should be proportional to the island diameter at equal surface coverages. Depending on the spot on the surface, the surface coverage that is measured in the image differs dramatically in a range between 4.3% and 65%, which makes the boundary length not fully comparable.

3.3.2 Island size and distribution effect on the HER activity

We evaluate the 2D island catalysts by their ability to catalyze the hydrogen evolution reaction (HER). We measured the transferred charge at -0.2 V vs SHE, ie. at sufficient overpotential for HER, the HER onset potential, i.e. the overpotential of HER and the

Tafel slopes of each catalyst as function of the island properties. We use a pristine Au(111) electrode as reference for the improved catalytic activity after Cu UPD and PGM displacement. The onset potential of HER was measured to be -0.13 V vs SHE under the given experimental conditions. Literature values of -0.02 V have been measured with a rotating-disc electrode[Str+13; ACH90] and are therefore not fully comparable to our system that is not corrected for diffusion limitations at the static electrode. The charge densities were measured by integration of the current density from the HER onset to -0.2 V vs SHE. For Au(111), a value of 1.67 $\mu Q/cm^2$ was found between -0.13 V and -0.2 V vs SHE. Figure 3.8 shows the respective HER charge densities for Pd/Au(111) (●) and Ir/Au(111) (■) as function of the deposition duration of Cu UPD at 0.47 V vs SHE.

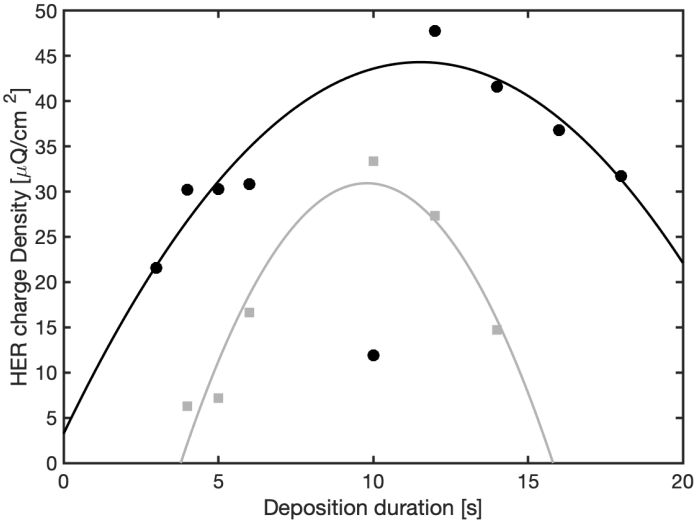

Figure 3.8.: HER charge density of Pd/Au(111) (●) and Ir/Au(111) (■) as function of the deposition duration during Cu UPD at 0.47 V vs SHE. The lines are guides to the eye to indicate the increase and decrease of catalytic activity for HER. Image reprinted from [OD21] under CC license.

The data show an initial increase of the charge density for Pd/Au(111) from a deposition duration of 3 s (21.6 $\mu Q/cm^2$) to a maximum of 47.7 $\mu Q/cm^2$ at 12 s. After reaching the maximum, the HER charge density decreases to 31.7 $\mu Q/cm^2$ at 18 s of deposition time. The trend is shown in the figure as a black line which serves as guide to the eye. Ir/Au(111) shows a similar trend as Pd/Au(111). At a short deposition duration of 4 s, a HER charge density of 6.31 $\mu Q/cm^2$ is measured. The charge density maximum of 33.4 $\mu Q/cm^2$ is found at a deposition duration of 10 s, which is at shorter deposition durations than the Pd based catalyst. At a deposition duration of 14 s, the charge density decreases to 14.7 $\mu Q/cm^2$. The dependence of the island size on the deposition duration is shown in Figure 3.7. The HER charge density increases with increasing island size for both, Pd and Ir catalysts before it reaches a maximum at an island diameter of ca. 15 and 13 nm, respectively. At longer deposition durations, the islands begin to merge and the total boundary length decreases. The HER charge density follows this trend.

Pd/Au(111) prepared at 0.44 V vs SHE during Cu UPD shows significant higher charge densities compared to samples prepared at 0.47 V. The charge density of a Pd catalyst prepared with 3 s deposition duration during Cu UPD at 0.44 V is 114.2 $\mu Q/cm^2$, 528% higher than the same sample prepared at 0.47 V vs SHE (21.6 $\mu Q/cm^2$). The sample prepared at 0.44 V for 6 s shows a HER charge density of 196.8 $\mu Q/cm^2$.

The HER onset potential is found to be independent of the properties of the islands, i.e. independent of the island size, spacing or PGM coverage. In case of Pd/Au(111), the HER onset potential is -0.06 V vs SHE. The HER onset for Ir/Au(111) is found to be -0.10 V vs SHE. The overpotential of HER for Pd and Ir islands on Au(111) thus is 70 mV and 30 mV smaller compared to Au(111).

The Tafel slope of a catalyst for a given catalyzed reaction shows the efficiency of the catalyst to produce current on changes of the applied potential, i.e. how much overpotential needs to be applied to increase the current. The Tafel slopes of Pd/Au(111) (▲: 0.44 V, ■: 0.47 V) and Ir/Au(111) (●) as function of Cu UPD deposition duration, i.e. island size are shown in Figure 3.9.

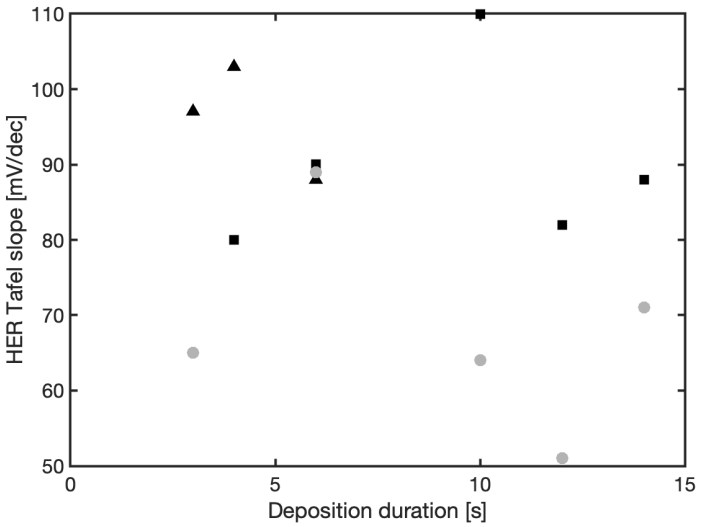

Figure 3.9.: Tafel slopes of Pd/Au(111) (▲: 0.44 V, ■: 0.47 V) and Ir/Au(111) (●) as function of Cu UPD deposition duration, i.e. island size. Image reprinted from [OD21] under CC license.

The data show that the Tafel slopes are in general higher for the Pd based catalysts than for the Ir based ones. For Pd/Au(111) prepared at 0.47 V vs SHE, the average Tafel slope is 86±5 mV/dec. The slope is independent of the deposition time. The value at 10 s is an outlier that is also visible in the island size of that particular sample. The Tafel slope of Pd/Au(111) prepared at 0.44 V is 96±7.5 mV/dec, which is 10 mV/dec higher than the one of 0.47 V samples. Ir/Au(111) has an average Tafel slope of 68±14 mV/dec, thus 18 mV/dec lower than Pd/Au(111) prepared at the same Cu UPD potential.

3.3.3 2D island stability under *operando* conditions

Figure 3.10a shows the maximum HER current density for Pd/Au(111) (black) and Ir/Au(111) (grey) as function of the number of CV cycles in a potential range of -0.2 V to 0.5 V vs SHE. The loss of maximum HER current density is about 1% and 5% after 50 CV cycles for Pd and Ir island catalysts, respectively. It can be noted, that in case of Pd/Au(111), the HER activity increases and decreases in a wavy pattern with an activity maximum every 4-5 cycles.

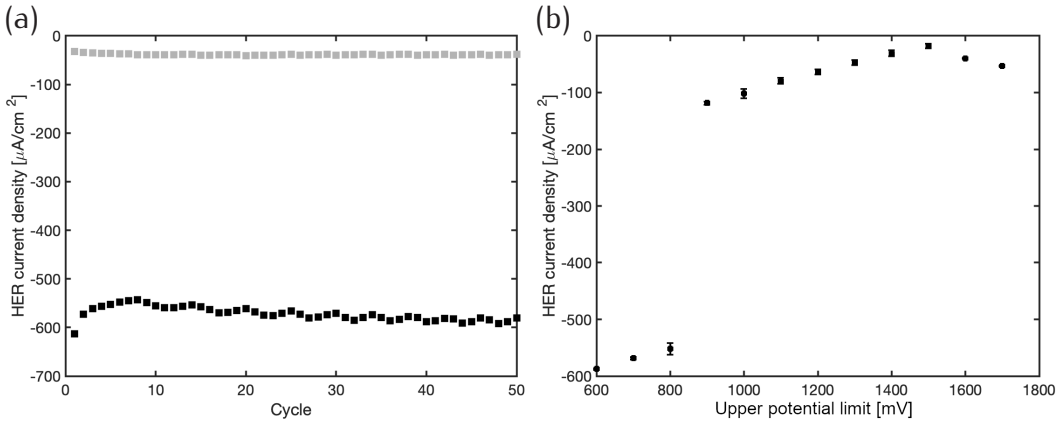

Figure 3.10.: (a) Long-term stability of Pd/Au(111) (black) and Ir/Au(111) (grey) showed as maximum HER current density as function of the number of cyclovoltammetric cycles n a range between -0.2 V and 0.5 V vs SHE. (b) Maximum HER current density of Pd/Au(111) as function of the upper potential limit of consecutive CV scans. Image reprinted from [OD21] under CC license.

The stability of the Pd/Au(111) system was also probed in a wider potential range to determine the potential onset of HER activity loss in line with the oxidation of the Pd islands. The HER current density is shown in Figure 3.10b as function of the upper potential limit of respective CVs over three cycles. The HER current density decreases linearly from -588 μA/cm^2 to -552 μA/cm^2 in the potential range from 0.6 to 0.8 V. Further increase of the upper potential limit to 0.9 V leads to a sharp decrease of catalytic activity and a HER current density of only -118 μA/cm^2. After this potential, the HER current density decreases further to a minimum of -17 μA/cm^2 at 1.5 V vs SHE. Due to the onset of Au oxidation, the HER activity raises to -53 μA/cm^2 at 1.7 V vs SHE.

3.4 Influence of Cu UPD properties on island characteristics

The deposition potential of Cu UPD was chosen to deposit not more than 1/3 of a ML to avoid merging of the islands that are mainly concentrated at the Au steps.[Ovi+16]

The deposition of the first third of a ML starts at 0.55 V vs SHE. A full monolayer of Cu on Au(111) is deposited at 0.35-0.37 V prior to the start of Cu bulk deposition lower than 0.32 V vs SHE.[Zei+87]. The deposition potentials of 0.44 and 0.47 V vs SHE (Figure 3.1a) therefore lead to maximum surface coverage of 0.33 ML. The results show that a maximum surface coverage of 0.33 ML for Pd islands is reached at 0.44 V after 8 s and >18 s for 0.47 V vs SHE (Figure 3.1b), in line with the theoretical maximum of 0.33 ML at deposition potentials above 0.34 V.[May+19] The surface coverage vs deposition time curve is shifted towards longer durations for more positive deposition potentials. This can be understood in terms of the exponential behavior of the current vs time trace. At the initial moment of the UPD, the current strongly depends on the applied potential. At lower potentials, the initial current is much higher, and, therefore, leads to a larger amount of Cu deposited on the surface compared to higher potentials. At durations >1 s, the growth of surface coverage is small compared to the influence of the applied potential. This can be used to fine-tune the amount of Cu deposited on the surface. Higher deposition potentials allow more control of the amount of Cu while lower deposition potentials lead to higher coverage in shorter time.

The current-time traces show exponential behavior for both applied potentials (0.44 and 0.47 V vs SHE) during Cu UPD (Figure 3.2). The exponential decay of the current indicate that the UPD process is not merely diffusion controlled.[HRK94] On the other hand, a process following purely the nucleation and growth law would show a current-time trace that show a local minimum followed by a current maximum.[Gar+07] The Cu UPD 2D nucleation and growth process is rate limited by a lattice incorporation process (2DLI). Nucleation rate and the number density of active sites are both dependent on the applied potential during Cu UPD.[PGB00] STM images of Pd/Au(111) prepared by Cu UPD at 0.44 and 0.47 V vs SHE, respectively, show a significant difference in the number of islands and the size of the islands (Figure 3.6). At lower deposition potential, the amount of islands is much higher compared to the more positive potential of 0.47 V. This shows the higher nucleation rate for lower potentials. At lower potential, more nuclei are formed in the initial stage of Cu UPD. Palomar-Pardavé et al. have shown that higher overpotentials for Cu UPD require less Cu atoms to form a stable nucleus than lower overpotentials. The critical nucleus size is smaller for lower potentials. After the early step of nucleation, the current density decays exponentially. The transferred charge required to reduce the same amount of Cu from solution is the same, independent of the applied potential. Both, high and low deposition potentials, follow a $t^{-1/2}$ law, i.e. the island growth is diffusion limited by the mass transport of Cu to the electrode, which is in agreement with literature.[Sta+78] This means that a similar charge leads to the growth of very different numbers of nuclei. In case of the lower deposition potential of 0.44 V, many nuclei have been formed and the charge transferred after the initial stage leads to growth of these nuclei. A similar charge leads to the growth of much fewer nuclei in case of the higher potential. That means that in case of more negative deposition potentials, more islands are formed during nucleation and the islands grow

smaller on average compared to more positive deposition potentials because of diffusion limitations. The total amount of Cu deposited after the early nucleation step is the same for both potentials.
The differences in surface coverage calculated from STM image analysis and the CV data are a result of the different measuring techniques. The CV data are average data over the total exposed surface area of the electrode and therefore show values of the surface coverage that are at or below the theoretical maximum of 0.33 ML. STM images, however, can only show one small area of the total electrode surface. Surface coverage values obtained from STM images show values with a large variation between 5% and 65% coverage. This large variation of surface coverage indicates that this value strongly depends on the imaged area. Thus, STM images can be used to show qualitative trends for island size and inter-island spacing but they cannot be used to quantify the efficiency of the displacement process or Cu UPD.
The heights of the islands are in line with theoretical expectations. Pd islands show heights of 0.33 nm, the atomic diameter of Pd is 0.34 nm.[80] However, it can be noted that some STM images of Pd/Au(111) show islands with an apparently smaller height of about 0.1 nm. Flatter islands are only observed in STM images recorded in ambient environment, and therefore, auto-oxidation of the islands can not be ruled out. (Partial) oxidation of the Pd islands could lead to smaller tunneling current and thus to smaller apparent height of the islands.[Meh+20] We speculate that these flatter islands are partially oxidized Pd islands.

Just like the island size, the inter-island distance also depends on the applied potential during Cu UPD. The more nuclei are formed per unit area, the smaller the distance between these nuclei. The effect gets attenuated by the fact that at higher potential the islands grow larger and therefore the inter-island distance gets smaller. Nonetheless, the inter-island distance of Pd islands produced at 0.47 V vs SHE (4.8 nm) is three times higher than corresponding islands produced at 0.44 V vs SHE (1.5 nm). The length of the island boundaries is also strongly effected by the applied potential because it is also a function of the number of nuclei formed in the early nucleation phase. The more nuclei are formed, the more islands are formed per unit area. More separate islands at the same surface coverage means more rim sites and therefore a larger island boundary length. At a deposition duration of 6 s, the island boundary length of Pd/Au(111) formed at 0.44 V is more than twice as long as seen for Pd/Au(111) formed at 0.47 V (Table 3.1). This effect remains until the islands begin to merge because the inter-island distance gets to small for long deposition durations. Merging of the islands is not favorable because the number of Pd/Au rim sites is drastically lowered when the islands tends towards merging to a large overlayer.

Even though the applied potential and deposition duration are applied during Cu UPD and therefore influence the characteristics of the Cu islands prior to the galvanic

displacement with Pd or Ir, the effect of the UPD properties on the island properties is transferable to the final Pd/Au(111) catalyst. STM images of Cu islands after Cu UPD and subsequent rinsing in MilliQ (according to the procedure we use) do not show significant differences to samples that were not rinsed subsequently after Cu UPD, so that we can assume that the island shape is reproduced during galvanic displacement with Pd. Moreover, XP spectra do not show residues of Cu on the surface after galvanic displacement. In case of Ir, we see on average larger islands compared to Pd/Au(111) produced under the same conditions. For Ir/Au(111), the islands appear less uniform than for Pd/Au(111), with a larger distribution of island size. The standard deviation of the size for Ir/Au(111) is about twice as high as for Pd/Au(111). This can be explained by two factors. One factor is the metal displacement reaction for the two PGMs shown below. In case of Pd, the galvanic displacement reaction employs a bivalent Pd salt (H_2PdCl_4), that has an electron ratio of 1:1 when exchanged with Cu to Cu^{2+}.

$$H_2PdCl_4 + Cu^0 \longrightarrow Pd^0_{(s)} + 4Cl^- + 2H^+ + Cu^{2+} \tag{3.1}$$

Ir, however, is employed in form of the salt H_2IrCl_6, containing an Ir ion with a charge of +4. Given the RedOx reaction, the ratio when exchanged with Cu to Cu^{2+} is 1:2 instead of 1:1.

$$H_2IrCl_6 + 2Cu^0 \longrightarrow Ir^0_{(s)} + 6Cl^- + 2H^+ + 2Cu^{2+} \tag{3.2}$$

The consequence of this charge difference is that Cu islands are separated into smaller agglomerations of Ir during the galvanic displacement process, because two Cu atoms are needed to be exchanged for one Ir atom. The high mobility of the Ir atoms on the gold surface together with the space released between the individual atoms leads to the formation of small Ir agglomerates. These agglomerations can then merge together to form islands due to ad-atom diffusion. The resulting islands are less uniform in their size distribution compared to Pd/Au(111). The second factor for the difference between Pd/Au(111) and Ir/Au(111) is the stability of the ad-atoms on Au(111). Pd is known to interact strongly with Au, forming (subsurface) alloys sometimes. Ir, on the other hand, is essentially not miscible with Au[Gon12] and can therefore be expected to posses a higher mobility on Au(111) than Pd. This would favor more ad-atom diffusion and growth of the islands to larger size with larger size distribution, as the formed islands tend to merge to reduce the number of undersaturated rim sites.

3.5 Effect of island characteristics on HER

We evaluate the efficiency of the 2D confined catalysts by their activity to catalyze the HER. In terms of mass-activity, an optimized catalyst should have largest possible current densities, low overpotential and relatively low PGM surface coverage. The

pristine Au(111) electrode is used as reference for a surface coverage of 0%. The measured onset potential of HER for Au(111) of -0.13 V vs SHE differs by 0.11 V from literature values of -0.02 V.[ACH90; Str+13] This difference is because of different measuring techniques. We do not use a rotating disc electrode and, therefore, can not correct for diffusion limitations during our measurements, thus, our results are not quantitatively comparable to literature. Nonetheless, we can compare qualitative trends. Moreover, we can quantitatively compare the different samples measured with our method.

The HER onset for Pd/Au(111) and Ir/Au(111) was found to be -0.06 and -0.10 V vs SHE, respectively, independent of the island characteristics. The shift of +70 mV and +30 mV of the Pd and Ir samples versus Au(111) is in qualitative agreement with literature that report a more positive HER onset potential for Pd compared to Ir (and even more positive compared to pristine Au(111)).[ACH90]. The independence of the overpotential for HER on the island characteristics shows that the overpotential of HER is only material dependent and, under given conditions, not a function of island size or inter-island spacing. The material dependency of HER kinetics was already found by Butler[BK32] in 1936 and later explained by Trasatti.[Tra72] The latter one related the exchange current density of HER to the bond strength between metal catalyst and adsorbed H atoms H_{ads} and presented his results in volcano plots.[Tra72; PT94] Efficient HER catalysis requires a H-bond-strength of about 230 kJ/mol.[Tra72] The bond strength of Au-H_{ads} with about 190 kJ/mol is too weak to efficiently catalyze HER.[Tra72] The Ir-H_{ads} bond strength on the other hand is too strong (250 kJ/mol).[Tra72] Pd exhibits a Pd-H_{ads} bond strength suitable for efficient HER catalysis.[Tra72] Also other properties of metal catalysts have been proposed to correlate with the activity for HER catalysis such as the electron work function[CB56; Boc47; KN30], the extend of the d-electron character of the metal[ASD79; Vij71], the inter-atomic distance in the lattice[Lei49] or the potential of zero charge (pzc).[Ant60; HW87; Bru+84]

Unlike the onset potential of HER, we find that the HER charge density strongly depends of the island characteristics and thus, on the Cu UPD conditions. The HER charge density as a function of the deposition duration for Pd/Au(111) and Ir/Au(111) prepared at 0.47 V vs SHE is shown in Figure 3.8. It can be seen that prior to the start of island merging at deposition durations longer than 12 s, a maximum in HER charge density exists for both catalyst materials. A similar effect has been reported before for directly deposited Pd overlayers on Au(111).[Smi+12; Tan+05] At highest ad-metal surface coverages of 0.32 ML (18 s and 14 s Cu UPD deposition duration at 0.47 V vs SHE for Pd and Ir islands, respectively), the HER charge density drops. It has been suggested previously in different studies that the primarily HER active sites are defect sites such as kink sites or step-edges.[HB07; Len+19; Fes+18] The rim sites between Au(111) and the respective islands can be considered as such defect sites. Bjorketum

et al. published a detailed theoretical study on HER on Pd submonolayers on Au(111) in which they predicted a similar maximum in HER exchange current density and strong catalytic contribution of the rim sites.[Bjö+11] Here, we find that the number of active rim sites grows with the growing circumference of the islands. With further island growth, the ad-atom diffusion path drops below a critical length and the islands begin to merge. Merging of the islands leads to a decrease of the number of active edge sites resulting in a decrease of catalytic activity even though the total ad-metal surface coverage increases. Figure 3.11 shows the correlation between the increase of the boundary length (■) with deposition time and the increase in HER charge density (●) for Pd/Au(111) (0.47 V vs SHE).

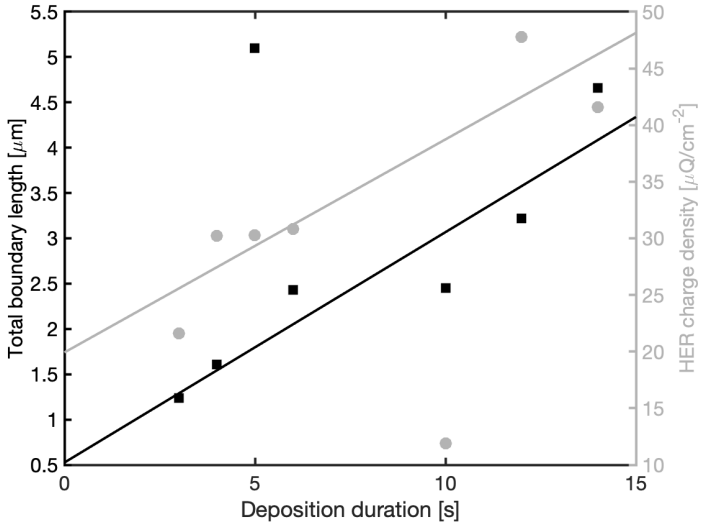

Figure 3.11.: Total boundary length (■) and HER charge density (●) as functions of the deposition duration during Cu UPD for Pd/Au(111) prepared at 0.47 V vs SHE.

We find a steady increase in rim length up to a deposition duration of 14 s. This increase correlates well with the increase in HER charge density. Note that the island edge length only gives a crude approximation of the number of active sites as it does not include defect or kink sites in/on the catalyst islands. Comparing the results from Pd/Au(111) samples prepared at different deposition potentials of 0.44 and 0.47 V vs SHE, we find a significant difference in HER activity. At 0.44 V vs SHE, we find small islands (3.4 nm) with small inter-island distances (1.5 nm) and a high boundary length of 227.1 $\mu m/\mu m^2$. For Pd/Au(111) prepared at 0.47 V vs SHE, we find bigger islands (13.8 nm) with a larger inter-island distance of 4.8 nm and a boundary length of 102.5 $\mu m/\mu m^2$. The resulting HER charge densities are 196.8 $\mu C/cm^2$ and 30.8 $\mu C/cm^2$, respectively. We see that the high boundary length of the small islands leads to a significant higher HER activity compared to the smaller boundary length. If we assume that during HER, one electron is transferred per active Pd atom, we can calculate the number of atoms per unit area n_{Pd} for the samples to be $1.23 \cdot 10^{21}$ atoms/cm^2 (0.44 V, 6s) and $1.93 \cdot 10^{20}$ atoms/cm^2 (0.47 V, 6s). Further, we can assume that only Pd edge atoms are active sites for HER catalysis. Then n_{Pd} is the number of edge atoms per unit area. From STM images, we can estimate the approximate number of edge

atoms from the boundary lengths to be $6.63 \cdot 10^{13}$ atoms/cm^2 (0.44 V, 6s) and $3.01 \cdot 10^{13}$ atoms/cm^2 (0.47 V, 6s). These numbers estimated from STM analysis are much lower than the numbers calculated from HER charge densities but are in qualitative agreement.

The Tafel slopes for Pd/Au(111) after Cu UPD@0.47 V vs SHE range between 80 and 90 mV/dec with an average Tafel slope of 86 mV/dec. The average Tafel slope for Ir/Au(111) after Cu UPD@0.47 V is 68 mV/dec, thus 18 mV/dec lower than the average Pd sample. For Pd/Au(111) prepared from Cu UPD@0.44 V, the average Tafel slope is 96 mV/dec, 10 mV higher than the samples prepared at 0.47 V. A pristine Au(111) has a Tafel slope of 110 mV/dec. From the Tafel slopes, the rate determining step of the mechanism of the catalyzed reaction, i.e. HER, can be derived. For pristine Au(111) with a Tafel slope of 110 mV/dec, a Volmer-Heyrowsky Mechanism can be assigned.[Smi+12] This mechanism is characterized by a Volmer step describing the adsorption and reduction of H atoms and thus lead to a MH_{ads} species. The subsequent and rate determining Heyrowsky step describes the formation of molecular hydrogen from the adsorbed intermediate[BB08]:

$$\mathrm{MH_{ads} + H^+ + e^- \longrightarrow M + H_2} \tag{3.3}$$

The Pd/Au(111) and Ir/Au(111) catalysts show significant lower Tafel slows. Lower Tafel slopes are an indication for lateral interactions between adsorbed hydrogen and surface atoms.[Smi+12] These lateral interactions lead to a change in the rate determining step from a Heyrosky step to a Volmer step. The Volmer step describes the formation of molecular hydrogen by direct interaction of two adsorbed intermediates[BB08]:

$$\mathrm{MH_{ads} + MH_{ads} \longrightarrow 2M + H_2} \tag{3.4}$$

The mechanism of HER can therefore be assigned as Volmer-Tafel mechanism for Ir/Au(111) with the rate determining Tafel step, as indicated by low Tafel slopes. The slightly higher Tafel slopes of Pd/Au(111) indicate a mixture of the mechanisms, i.e. a Volmer-Heyrosky mechanism with slow Volmer steps, as has also been reported in previous studies for the Pd/Au(111) HER system.[Smi+12] The small deviations from the average Tafel slope in case of Pd/Au(111) samples prepared at different deposition durations show that the island morphology plays a secondary role for the mechanism of HER. Smaller islands, however, tend to push the HER towards the Volmer-Heyrowsky mechanism, as indicated by the higher Tafel slopes of samples prepared at 0.44 V.

3.6 2D catalyst stability

The charge density in the HER region is an indicator of the presence of catalytically active Pd or Ir sites on the Au surface. A decrease of HER charge density thus is an

indication of a decrease in the number of active sites. We have probed the long term stability of the catalysts in a small potential range from -0.2 V to 0.5 V and on an increasing potential range with increasing upper limit.
In the small potential range, we observe a loss in charge density of <1% for Pd/Au(111) and 5% for Ir/Au(111) over 50 CV cycles. This indicates a higher stability of the Pd islands comapred to the Ir islands. Moreover it shows that the catalyst can be used over at least 50 cycles without loosing most of its catalytic activity for HER.
We find that the critical upper potential limit for the onset of severe loss of catalytic activity lies between 0.8 and 0.9 V vs SHE. This finding is in agreement with the onset of Pd defect oxidation starting at 0.84 V vs SHE.[Tan+05] In case of Pd islands, we have highly reactive undercoordinated Pd edge sites that are easy to oxidize. We expect that the oxidation of Pd nanoislands leads to (partial) dissolution of the islands and, therefore, irreversible partial degradation of the sample and loss of its catalytic activity.[El-02] The oxidation of defect sites, such as steps or kink sites, is thermodynamically favorable over the terrace oxidation. This is why we expect the oxidation to start at the Pd/Au rims which would lead to a fast inhibition of the HER activity.
Due to the thermodynamics of surface oxidation, the size distribution should play a role for the onset of island degradation. A large number of small islands exhibits a higher rim-to-terrace site ratio, and, therefore should be more oxidation prone compared to larger islands with relatively smaller boundary length.

3.7 Summary and outlook

In this work we have presented a simple route for fabrication of 2D confined PGM nanoislands on Au(111) that function as efficient 2D HER catalysts with respect to the mass activity via two steps, Cu UPD and subsequent galvanic displacement (Figure 3.12). The size and surface distribution of the resulting islands and thus the HER activity can be well controlled by tuning the applied potential and duration of the Cu UPD step.

The Cu islands resulting from the Cu UPD step can easily be displaced by any more noble metal, here by Pd and Ir to form Pd/Au(111) and Ir/Au(111), respectively. We find that a lower deposition potential of 0.44 V vs SHE leads to small islands with an average diameter of 2-3 nm while a higher deposition potential of 0.47 V vs SHE leads to the formation of larger islands with diameters that range from 5 to 14 nm. The island size parameters can be further controlled by tuning the deposition duration. The different size distribution resulting from different applied Cu UPD potentials is a result of the different number of nuclei formed in the early phase of Cu UPD. At lower potentials, more nuclei are formed compared to at higher potentials. In the later growth phase, the nuclei grow to larger islands consuming a similar Cu mass, thus

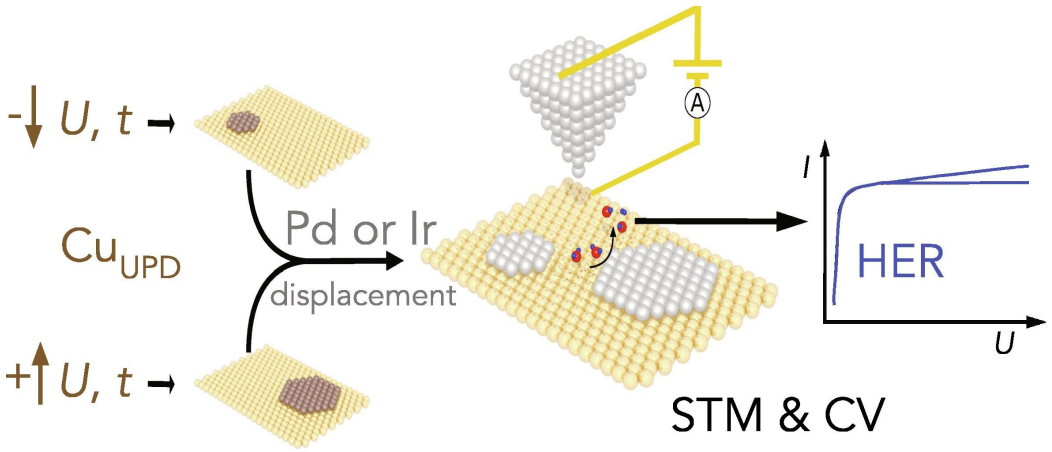

Figure 3.12.: Schematics of the presented two-step route towards 2D confined PGM nanoislands via Cu UPD and subsequent galvanic displacement. The fabrication of these islands is highly controllable via tuning of the applied potential and duration of the Cu UPD. The quality of the resulting catalyst was images by STM and probed by its ability to catalyze HER via CV. Image reprinted from [OD21] under CC license.

leading to bigger islands when fewer nuclei are available. The average inter-island distance is small for lower potentials (1.5 nm, Pd/Au(111)) and about three times larger for the higher deposition potential (4.8 nm). For Ir/Au(111), the inter-island distance is extraordinarily high with an average of 12.1 nm. This finding is explained by the high mobility of Ir on Au(111) compared to Pd, which is known to be able to form (subsurface) alloys on Au(111). Moreover, the different inter-island distance between Pd and Ir islands can be explained by the ratio of Cu to Ir and Pd, respectively, in the galvanic displacement process. The Cu-to-metal exchange ratio is 1:1 for Cu to Pd and 2:1 for Cu to Ir. In the latter case, this leads to a wider size distribution and larger inter-island distances.

We have characterized the different samples by their ability to catalyze the HER. We find that the HER charge density varies as a function of deposition duration at 0.47 V. The HER activity increases with increasing deposition time (and thus, island size and boundary length) before a critical duration is reached. For durations longer than that critical duration of 14 s and 10 s for Pd and Ir based catalysts, respectively, we observe a decrease of catalytic activity. Our data suggests an optimal combination of 2D catalyst confinement with an island size of 13-14 nm and an inter-island spacing of about 5nm. Higher PGM mass on the catalyst does not lead to higher HER activity. For Ir/Au(111), the best catalyst in terms of mass-activity has an inter-island spacing of 10 nm. These optimal catalysts in terms of mass activity can be reached with a deposition duration of 10-12 s at a Cu UPD potential of 0.47 V during Cu UPD. At lower deposition potential of 0.44 V vs SHE, an even higher activity for HER is achieved. Pd/Au(111) with islands of 2 nm size reach a HER charge density that is a factor 3-4 higher than slightly larger islands prepared at 0.47 V.

The HER activity drops by a maximum of 5% after 50 cycles in a potential range of -0.2 to 0.5 V, and it significantly drops at potentials higher than 0.8 V because of the

onset of Pd defect oxidation and reduction of the number of catalytically active sites. The work presented here provides a strategy to obtain controllable PGM islands that are highly active for HER. With this route highly mass-active catalysts for HER can be fabricated in a tunable fashion. The well defined catalyst islands are well suited for further studies of the fundamentals of catalytic mechanisms and electrode surface activities. To gain more information about the underlying mechanisms and kinetics during the surface reactions, high resolution STM experiments and nanosacale spectroscopy such as tip-enhanced Raman spectroscopy could shed light on Pd and Ir atomic locations, interactions and dynamics. In the following chapter we use the Pd based catalysts that were presented in this chapter to catalyze the formic acid oxidation reaction and to study the poisoning by reaction intermediates with the help of EC-TERS to further understand the reactivity of the 2D nanocatalysts.

Part IV

EC-TERS study to unveil the nature of catalyst poisoning agent during formic acid oxidation

4

EC-TERS study to unveil the nature of catalyst poisoning agent during formic acid oxidation

The chapter is about the study of the origin of catalyst poisoning during formic acid oxidation through reaction intermediates to understand how to avoid degredation of FAOR based catalytic devices through poisoning - A tip-enhanced Raman spectroscopy study.

Contents

This chapter is reproduced from the manuscript 'Daniel Ohm, Yawei Li, Jinggang Lan and Katrin F. Domke, *Insights into electrochemical catalyst poisoning during formic acid oxidation on 2D confined Palladium nanoislands via electrochemical Tip-enhanced Raman spectroscopy*, to be submitted to Electrochmica Acta, **2023**'.

The work presented in this chapter is the work of Daniel Ohm.

4.1 Introduction

The modern world faces the task to find a sustainable, economical and environmental friendly way of producing usable energy while overcoming the dependency of fossil fuels. One approach to overcome this dependency is the use of small organic molecules as fuels for fuel cells. The conversion of formic acid to CO_2 and the respective backreaction is one promising candidate to realize the goal of an effective fuel cell that does not rely on fossil fuel.[Ric+02; YP08; Ric+03] Formic acid is a byproduct of biorefinery processing, essentially non-toxic, it has a high energy density and is biodegradable.[Liu+15; BR18] These aspects make formic acid a good candidate as fuel for effective energy conversion devices from economical and ecological points of view.

The choice of the best-suited catalyst under ecological and economical aspects is also crucial for the successful turn to environmentally friendly direct formic acid fuel cells (DFAFC) and similar fuels from small organic molecules. With that, not only the theoretically most active catalyst is considered the best, but also mass activity, cost and availability play a role. For DFAFCs, Pt and Pd are considered to be the most active pure bulk metal catalysts[Che+22b], and Pd is also the most active bulk metal catalyst for CO_2 reduction.[Kor+15] The weak point of these catalyst materials is the loss of activity during operation of the fuel cell because they exhibit severe poisoning by intermediate products of the FAO reaction.[YP09] To find ways to avoid catalyst poisoning and the associated efficiency decrease of DFAFCs, a detailed understanding of the underlying poisoning mechanism is required.

FAO can be considered as electrochemical prototype reaction because of the molecular simplicity of the formic acid molecule. The FAO reaction is therefore well studied on different catalysts such as Pt, Pd, Au and mixed catalysts like Pd/Au(111) and on various others.[Gro+11; Per+15; HF18; Hos+06; BK96] Mechanistic studies of FAO have revealed a mixture of three competing pathways of the reaction mechanism. The pathways are I) the direct pathway, involving the dehydrogenation of formic acid to CO_2, II) the formate pathway, leading to intermediately adsorbed formate species prior to the formation of CO_2 and III) the indirect pathway that forms intermediate CO after dehydration of formic acid.[Cue+12; Osa+11] Studies suggest that on Pd based catalysts the direct pathway that does not involve any intermediates is the dominant FAO reaction mechanism.[BK96; ULL09; CP73] Nonetheless, Pd-based DFAFCs show

efficiency losses attributed to the poisoning of the catalyst used in the fuel cell.[YP09]. This studies are contradictory because (intermediate) products of FAO are not expected to be formed based on the direct reaction pathway of FAO.
In this study, we show the loss of electrocatalytic activity of a Pd(islands)@Au(111) catalyst after (partial) surface oxidation. We aim to study the reaction conditions that lead to catalyst poisoning by CO and the associated loss of catalytic activity with electrochemical (CV) and spectroscopy (EC-TERS) methods.

4.2 Experimental details

The preparation of the Pd(islands)@Au(111) samples is described in detail in chapter 3.
The Pd island samples used in this experiment are prepared at 0.47 V vs SHE CuUPD deposition potentials unless stated otherwise. The prepared samples were kept under Ar atmosphere with a covering water droplet for no longer than 12 hours before the start of the TERS experiment.
CV measurements are carried out in the TERS cell, described in section 2.2.6. CO saturated solutions are prepared by bubbling CO directly into the electrolyte prior to the TERS measurement for 5-10 minutes. Because the TERS setup does not allow for closing the cell during the experiment, contamination with air cannot fully be excluded. To avoid excessive diffusion of air into the electrolyte, an Ar is applied above the electrolyte prior to the experiment, so that the cell is Ar blanketed during the experiment.
TERS tips are prepared by electrochemical etching of an Au wire (0.25 mm diameter, 99.997% trace metal basis, Alfa Aesar) from a 1:1 mixture of EtOH (Merck) and fuming HCl (37%, Merck). A voltage of 2.4 V is applied between the tip and a ring-shaped Au counter electrode. The tip is placed in the middle of the ring and reaches few millimeters into the solution. Electrical isolation of the tip in TERS experiments is assured by coating the tips with Zapon paint.
The TERS setup that is used was described previously in section 2.2.6 of the fundamentals chapter. Data analysis is performed with Matlab software. Data treatment includes fast-Fourier transformation of the raw data using a filter function.[OHa22]. Spectra recorded over wide spectral range are automatically stitched together from three consecutively recorded small range spectra to maintain the highest spectral resolution using the 600 g/mm grating. Baseline correction is applied to the Fourier transformed spectra using an asymmetric least square method. The smoothening parameters are chosen in a way to avoid the creation of arbitrary signals and maintain the overall shape of the plasmonic background. Peaks are fitted as Lorentzians to determine the peak positions and FWHM.

4.3 Experimental results

In this study, we test the activity of the 2D Pd islands on Au(111) toward FAO and probe the island stability under *operando* conditions with EC-STM. In addition to previous studies (see Chapter 3), we focus on imaging the catalyst surface conditions at different potentials with EC-STM. Most importantly, we probe the nature of the catalyst poisoning species found during FAO on Pd/Au(111). Figure 4.1 shows (EC-)STM images recorded under ambient conditions (a) and under *operando* conditions in 0.1 M H_2SO_4 at 0.2 V vs SHE (b) and 0.8 V vs SHE (c). All images show Pd islands as bright spots on the darker Au(111) surface. The island size and distribution of (a) and (b,c) differs because two different Au substrates are used that differ in their surface morphology. To be able to compare the effect of the applied potential on the island morphologies, (b) and (c) are images of the same surface region of the same sample, recorded in consecutive measurements. STM height profiles of the islands show an average height of 0.32 nm. The average step edge height is 0.28 nm. In CO saturated electrolyte, only noisy STM images are recorded in our setup (see appendix A.1) and could not be further analyzed.

Figure 4.2 shows the CV of Pd/Au(111) in a mixture of formic acid and sulfuric acid in a potential window from 0.05 V to 0.7 V vs SHE. The first cycle (gray) shows the current during formic acid oxidation. It shows a current maximum at 0.47 V vs SHE and a peak current density of 230 $\mu A/cm^2$.

The onset of formic acid oxidation on the Pd/Au(111) catalyst used in this study is 0.17 V. However, after one cycle of formic acid oxidation, the peak current density drops to 0 $\mu A/cm^2$ and no significant charge is transferred. The catalyst shows no activity for FAO and can be compared to the activity of Au(111) towards FAO. Figure 4.3 shows LSVs of the same system after the loss of catalytic activity.

The linear sweeps ramp the potential from 0.05 V to 1.2 V vs SHE in formic acid containing electrolyte. The FAO charge density increases during the LSVs from less than 1 $\mu A/cm^2$ at the poisoned surface to 7 $\mu A/cm^2$ after 10 LSVs. The corresponding potential-time curve that is used in the depoisoning process is shown in figure 4.4.

After the depoisoning process, the FAO can be run without further loss of activity. Figure 4.5a shows the a sample without formic acid in the supporting electrolyte as reference. Figure 4.5b shows the CV of the same Pd/Au(111) sample with FAO conditions for five cycles after depoisoning. The peak current density remains constant at about 55 $\mu A/cm^2$ at 0.47 V vs SHE. Without formic acid, the catalyst shows strong HER activity with a maximum current density of 3 mA/cm^2 at -0.2 V vs SHE and the typical H desorption on Pd at potentials positive of 0 V vs SHE.

The possibility of catalyst poisoning by CO is probed with CV in CO saturated electrolyte in an electrochemical glass cell setup. The electrolyte is first saturated with CO by bubbling directly into the solution. After each CV, Argon is bubbled through

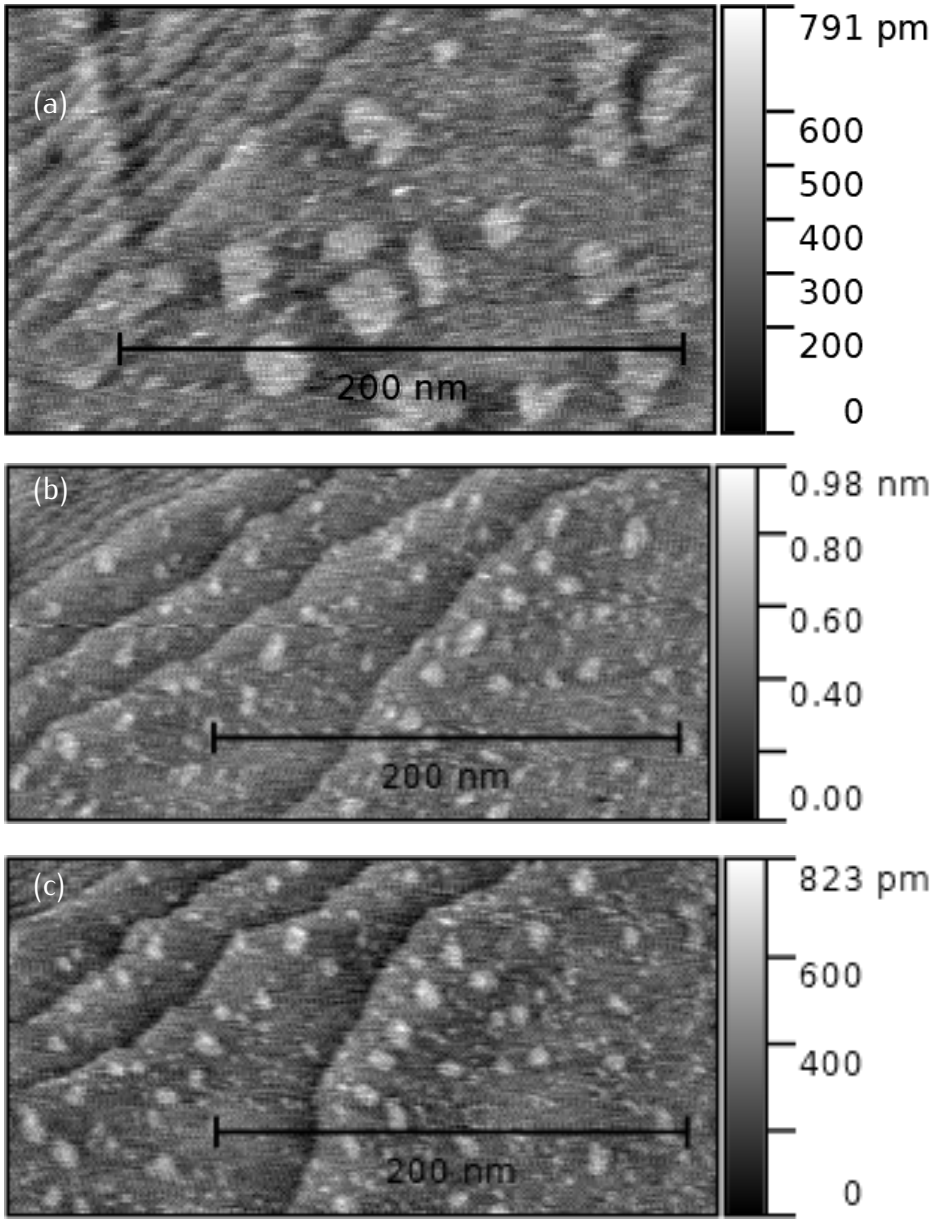

Figure 4.1.: STM images of Pd/Au(111) recorded under (a) ambient conditions and under *operando* conditions at (b) 0.2 V vs SHE and (c) 0.8 vs SHE. Bright spots are Pd islands on top of dark Au(111).

the solution for 2 minutes to reduce the amount of CO in the electrolyte to probe the behaviour of the catalyst when different amounts of CO are present in the electrolyte. Figure 4.6 shows the blocking of catalytically active sites for HER in CO saturated electrolyte. With a decrease of CO concentration, the HER charge density increases until the CO concentration is too low to effectively poison the catalyst and block the active sites.

The HER charge Q increases from 10^2 µAs to 10^4 µAs after cumulative 11 minutes of bubbling Ar into the solution. The increase of the HER charge by two orders of magnitude upon CO concentration decrease is accompanied with a shift of the HER onset potential from -55 mV to -42 mV, i.e. a decrease of the HER overpotential of

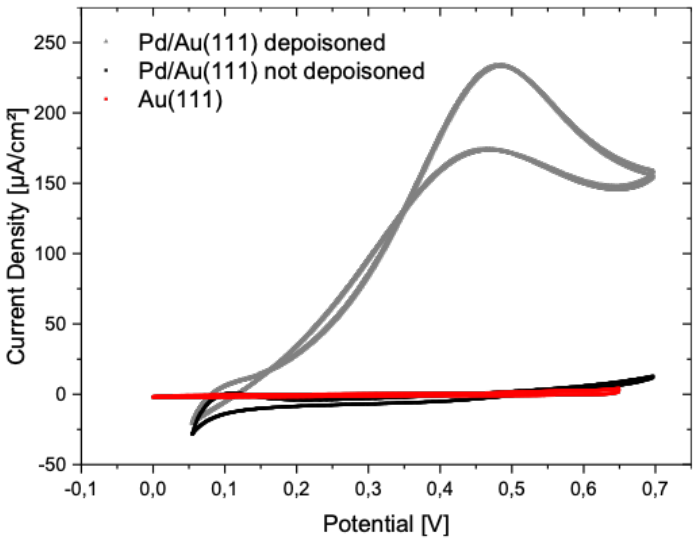

Figure 4.2.: CVs of Pd/Au(111) in formic acid containing electrolyte. Gray shows the first cycle of FAO with a peak current density of 230 µA/cm^2 at 0.47 V vs SHE. The black cycle shows the total loss of catalytic activity of the system for FAO.

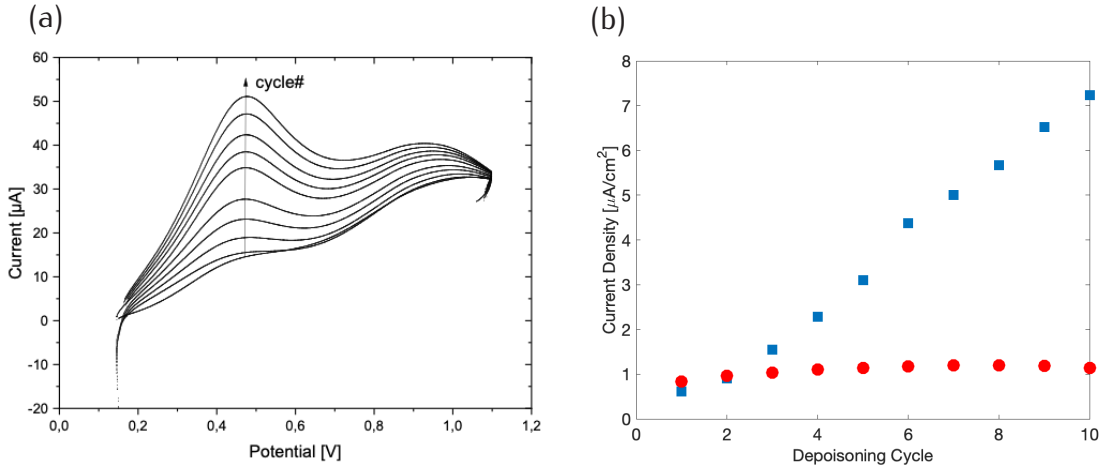

Figure 4.3.: Depoisoning of the Pd/Au(111) catalyst. (a) Linear sweep voltammograms of Pd/Au(111) in formic acid containing H_2SO_4 from 0.05 V to 1.2 V vs SHE. The peak current density increases with increasing number of LSVs. (b) Increase of the FAO peak current densities as a function of the number of LSVs for depoisoning.

13 mV. Figure 4.7 shows the CO stripping and readsorption on Pd/Au(111) in CO saturated electrolyte in the CV scans between -0.08 and 1.2 V vs PdH.

The first cycle (dashed) shows stripping of CO from the fully blocked Pd/Au(111) catalyst at 0.71 V. Readsorption of CO from the electrolyte occurs in the cathodic scan at 0.62 V. The CO stripping is not fully reversible under the given experimental conditions and CO concentration. With increasing number of scans, the amount of CO on the catalyst decreases, indicated by a decrease of CO stripping charge from $4 \cdot 10^{-2}$ µQ to $8 \cdot 10^{-3}$ µQ.

EC-TERS was used to investigate the chemical fingerprint of the poisoning agent

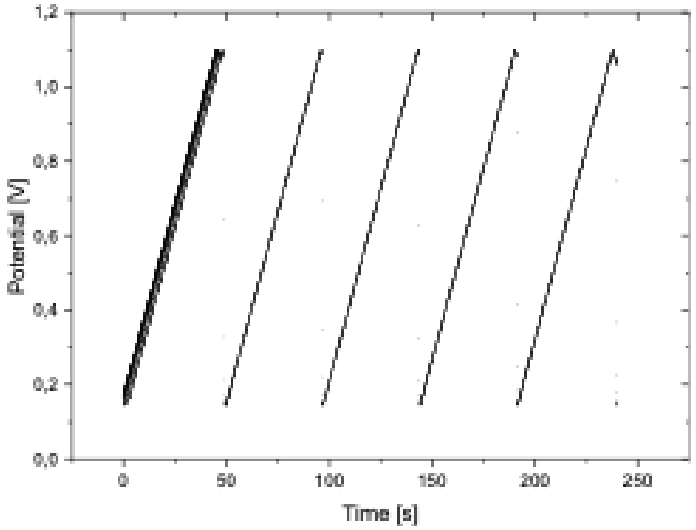

Figure 4.4.: Potential-time curve that was used for depoisoning. The potential was ramped linearly from 0.05 V to 1.2 vs SHE.

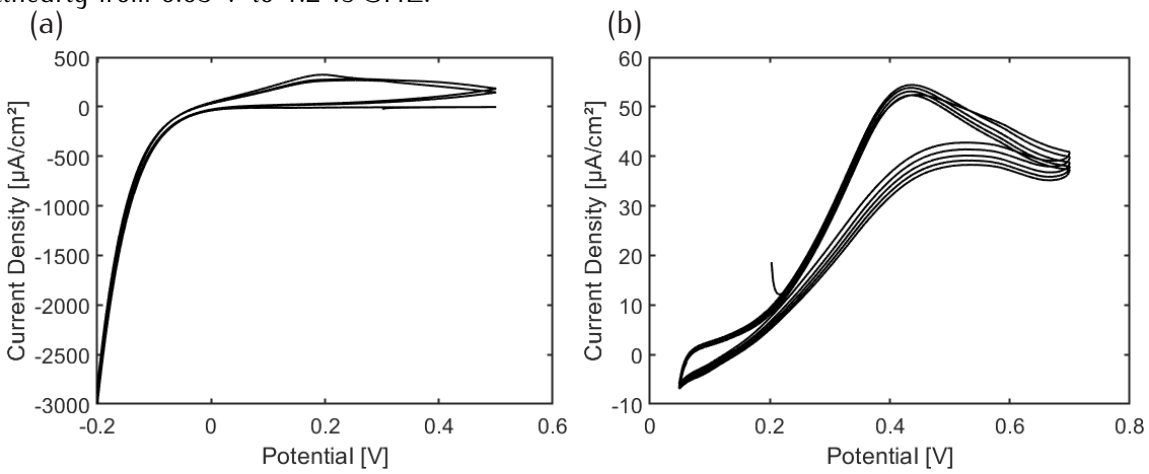

Figure 4.5.: (a) CV of Pd/Au(111) without formic acid in 0.1 M H_2SO_4, scan speed 25 mV/s. (b) Same sample as in (a) but with formic acid in the supporting electrolyte.

that was found to effectively block the catalyst for FAO. We recorded EC-TER spectra in 0.1 M H_2SO_4, pure and with formic acid and CO, respectively, in the solution. Spectra were recorded after immersion at an immersion potential of 0.3 V as reference before FAO. FAO was triggered by ramping the potential to 0.7 V. To see a signal difference between poisoned and not poisoned surface, the potential was ramped successively to 1.2 V. After reaching the upper potential, we lowered the potential again and recorded a potential series to investigate the behavior upon potential change. The tip position (on top of Au and on top of Pd, respectively) was controlled by EC-STM.

Figure 4.8 shows raw TER spectra recorded at 0.6 V (i.e. prior to Pd oxidation) (blue) and 1.2 V (i.e. after FAO and Pd oxidation) (black) on top of Pd. The blue spectrum shows no major peaks with significant signal to noise ratio. The spectral region between 1700 and 2400 cm^{-1} is essentially flat. The black spectrum, however, shows bands at 264, 620 and 2192 cm^{-1}, the latter one in the region of interest between 1700 and

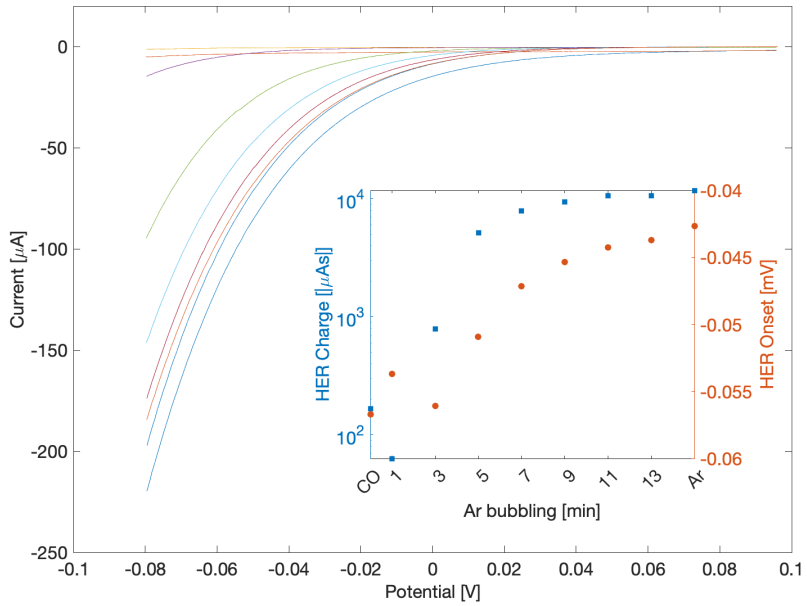

Figure 4.6.: CVs of Pd/Au(111) in electrolyte with decreasing concentration of CO. Inset: HER charge as function of the time Argon was bubbled into the electrolyte to lower the CO concentration..

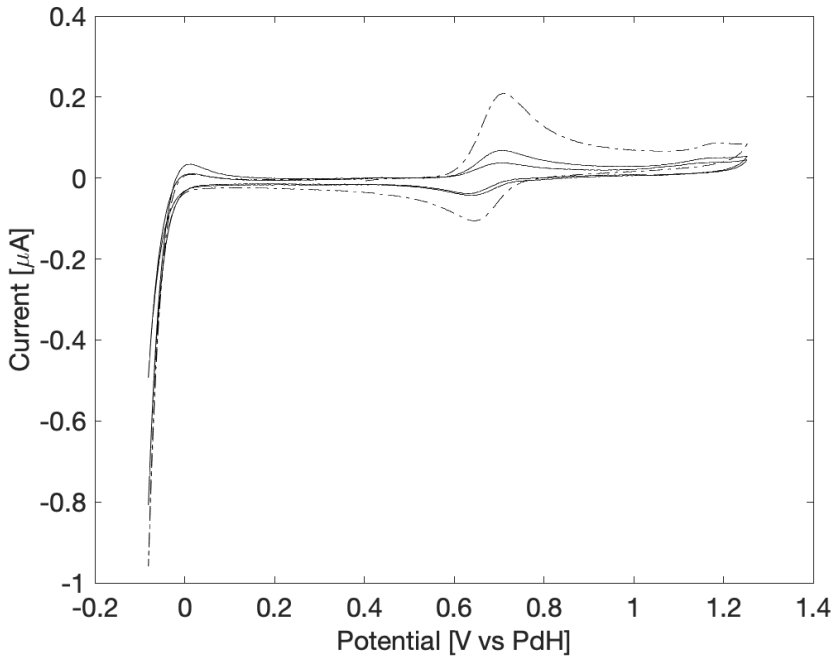

Figure 4.7.: CVs of Pd/Au(111) in not fully CO saturated electrolyte. The dashed line indicates the first CV cycle.

2400 cm^{-1}. EC-TER spectra recorded in CO saturated electrolyte without the presence of formic acid show the same behavior. Figure 4.9 shows uncorrected spectra recorded in CO saturated H_2SO_4 at 0.5 V (blue) and after ramping the potential to 1.2 V vs SHE

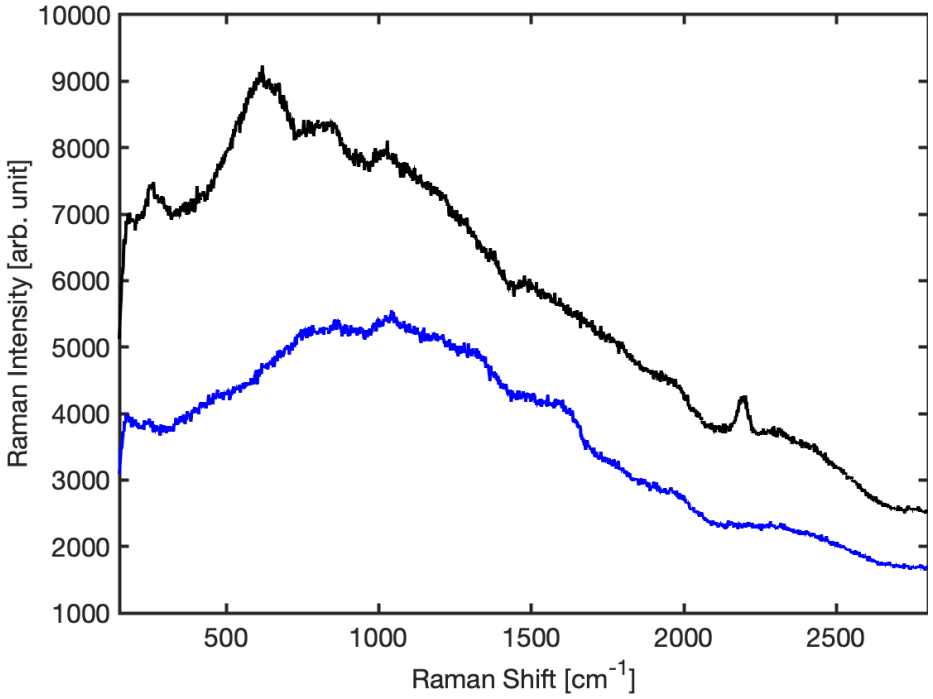

Figure 4.8.: Raw EC-TER spectra recorded at 0.6 V (i.e. prior to Pd oxidation) (blue) and 1.2 V (i.e. after FAO and Pd oxidation) (black) on top of Pd.

(black) and without CO in the electrolyte recorded at 1.2 V vs SHE (magenta). The blue and magenta spectra show bands in the lower Raman shift region at 979, 1047 and 1399 cm^{-1} and a flat region between 1700 and 2400 cm^{-1}. The black spectrum shows an additional band at 2190 cm^{-1}.

Computational data obtained from our collaborators Jinggang Lan and Yawei Li from EPF Lausanne are used to study the most stable, high-coverage adsorption structures of CO on pristine Au(111), Pd-coated Au(111), a PdO_2(111) slab and PdOx/Au(111). They used *ab initio* methods to calculate the CO stretch vibrations upon adsorption on different adsorption sites on the materials. On pristine Au(111), a CO stretch frequency of 2056 cm^{-1} is found at an applied potential of 1.25 V vs SHE, 144 cm^{-1} lower than the shift found in our experiments. On Pd/Au(111), an even lower shift of 1916 cm^{-1} is calculated, 284 cm^{-1} lower than the experimental value. However, on the oxidized surfaces, values much closer to the experimental values are obtained. For the CO stretch vibration on PdOx/Au(111), a Raman shift of 2130 cm^{-1} is calculated, 70 cm^{-1} lower than the shift found in EC-TERS experiments. The highest calculated shift is found for PdO_2(110), with a frequency of 2163 cm^{-1}, 37 cm^{-1} less than the value found in TERS experiments.

The band of interest at 2192 cm^{-1} is further investigated by recording a potential series of EC-TER spectra. Here, as we focus on the particular band, we record spectra over a short frequency range between 1200 and 2700 cm^{-1} at potentials between 1200 and -100 mV after poisoning the surface with CO during FAO. The acquired TER spectra are shown in figure 4.10a as waterfall plot with respective y-offsets of 100 [arb. units] for each spectrum. 4.10b shows the band positions as obtained from Lorentzian

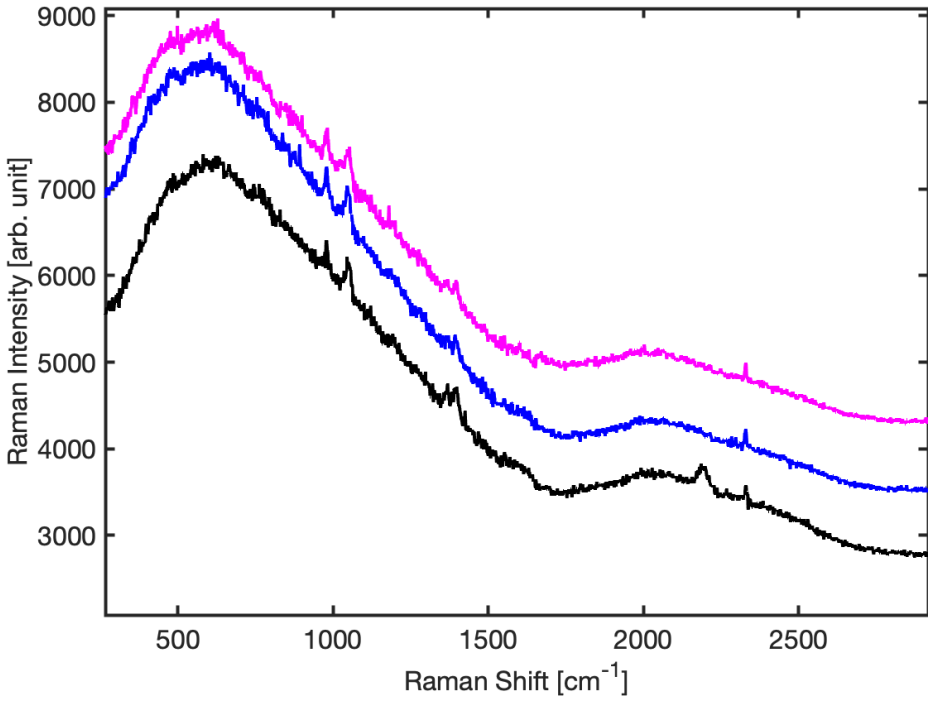

Figure 4.9.: EC-TER spectra of Pd/Au(111) recorded on top of Pd in CO saturated electrolyte. The blue spectrum was recorded at 0.5 V, the black spectrum after ramping the potential to 1.2 V vs SHE. The magenta spectrum was recorded on top of Pd without CO at 1.2 V vs SHE. The spectra are plotted on top of each other with an offset of 800 counts each.

fits as a function of the applied potential.

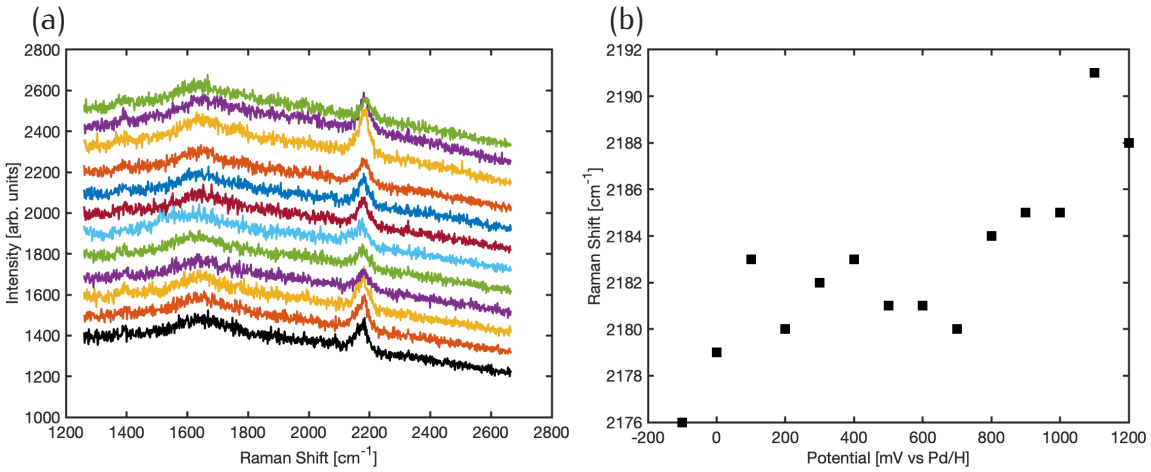

Figure 4.10.: (a) Waterfall plot of EC-TER spectra recorded in the range from 1200-2700 cm^{-1} at potentials between 1200 to -100 mV in CO saturated electrolyte. The respective spectra are plotted with y-offsets of +100 arb. units each. (b) Raman shift of the band of interest as function of the applied potential. The shift was obtained from Lorentzian peak fitting routine.

The tip position is held constant while the spectra are acquired at different potentials. The band positions are obtained by Lorentzian fitting of the baseline subtracted spectra. The data show a blueshift of the band of interest with increasing potential. At low potential of -0.1 V vs SHE, the band is found at 2176 cm^{-1}. At high potential of 1.1 V

vs SHE, the band of interest is located at 2191 cm^{-1}, a difference of 13.6 $cm^{-1} \cdot V^{-1}$. Note that the sign of the applied tip-sample bias is changed from -0.2 V to +0.2 V at the potential step from 1.0 V to 1.1 V vs SHE to avoid tip oxidation starting at potentials higher than 1.2 V (surface potential) and therefore to avoid a change of the tip properties for the rest of the experiment.

The band of interest cannot be observed in conventional Raman spectra, i.e. with the tip retracted several µm from the surface to switch off tip enhancement. The conventional Raman spectrum is shown (blue) compared to the nearfield spectrum (black) without baseline correction in figure 4.11.

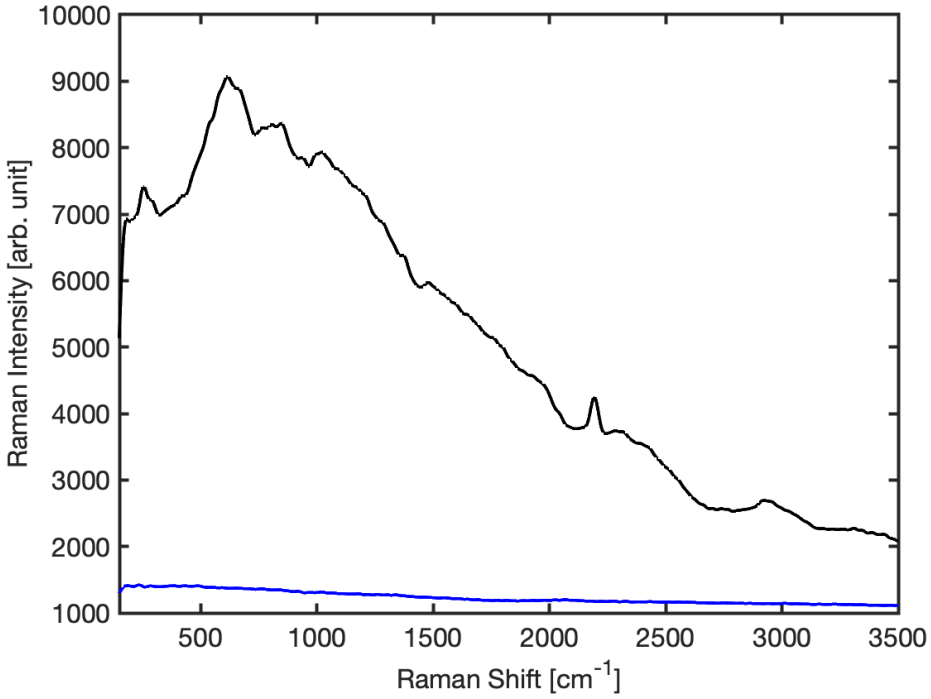

Figure 4.11.: Raman spectrum of the poisoned catalyst surface in nearfield (black) and farfield (blue). For the farfield spectrum acquisition, the tip was retracted several µm from the surface to loose tip-enhancement.

In addition to the experiments with constant tip position during the experiment, EC-TERS mapping experiments are carried out with the goal to correlate the band of interest (intensity and position) with the surface sites provided by the EC-STM image. In the mapping experiment, the probed surface is divided into a 8-by-8 or 16-by-16 grid, respectively. The tip is moved horizontally along the grid and a spectra was acquired after each step. After each grid line, the tip is scanned in lines to reach the next horizontal line of the grid. Figure 4.12 shows an EC-STM image image with an 8-by-8 grid overlay. The red dots indicate the tip positions at which TER spectra are acquired. The red arrow marks the horizontal tip movement while stepping along the grid x-axis and acquiring spectra. The black arrow indicate the tip movement while scanning to the next line in the grid.

The resulting map shows the integrated intensity of a chosen spectral area of interest in the respective parts of the grid. Figure 4.13a shows an EC-STM image acquired

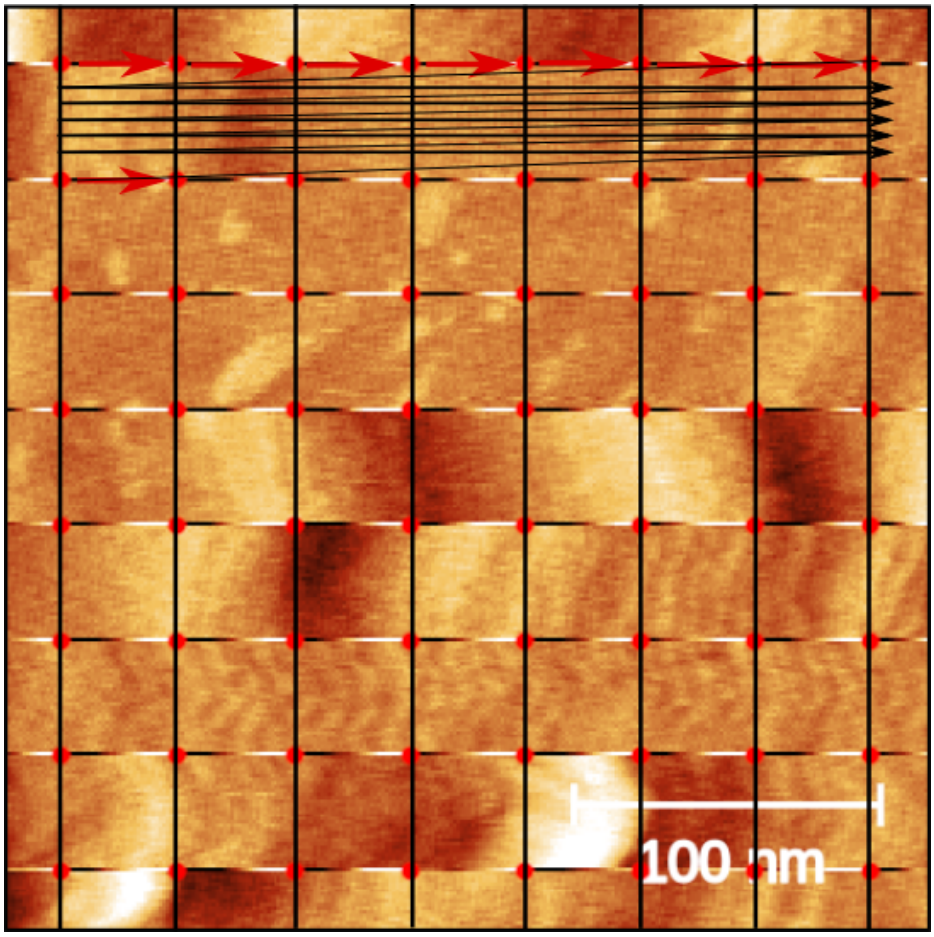

Figure 4.12.: EC-STM image recorded during a mapping experiment with 8-by-8 grid overlay. Red dots mark the tip positions at which spectra are recorded. The tip is moved along the red arrows and one spectrum is recorded after each step. The black arrow shows an example of the movement of the tip while scanning down to the next horizontal grid line.

during mapping, the resulting EC-TERS map with an integrated spectral range from 580 to 650 cm^{-1} is shown in 4.13b. The mode at 2190 cm^{-1} is not observed in any of the recorded spectra, so that a spectral range is chosen that shows a signal that vary based on the tip position to test the experiment. However, the current state of the EC-TERS setup does not allow for sufficient stability to achieve meaningful mapping results on the CO@Pd/Au(111) system. The STM image shows strong variations in the tip position while moving to the next line of the grid, which makes an interpretation of the data nearly impossible, unless an area of interest lies within a grid line.

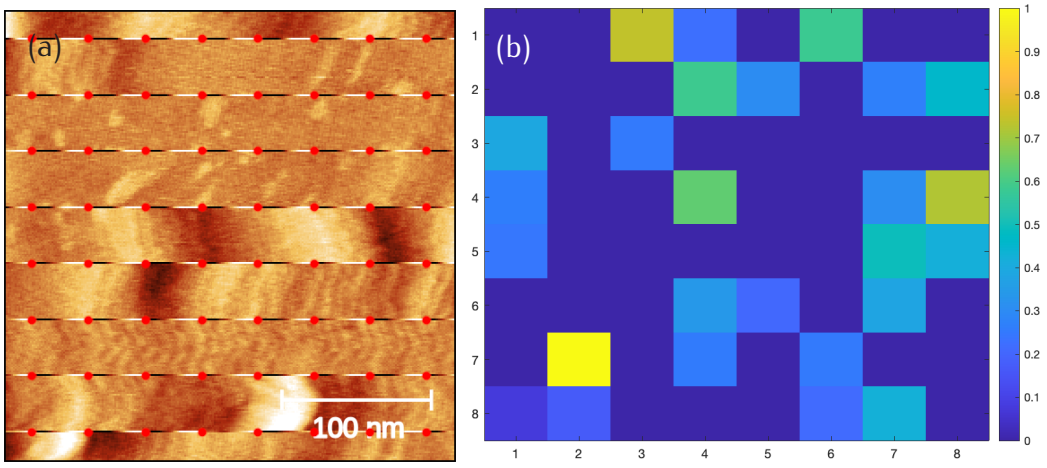

Figure 4.13.: (a) EC-STM image acquired during mapping acquisition of 64 EC-TER spectra on a 8-by-8 grid. (b) EC-TER map resulting from 8-by-8 mapping acquisition with an integrated spectral range from 580 to 650 cm^{-1}.

4.4 EC-STM - Imaging under *operando* conditions

Ambient and EC-STM images shown in figure 4.1 show bright Pd islands formed mostly in close proximity of the Au(111) step edges. The Pd adlayer shows similar distribution and morphology in all three images, independent of the applied potential or environmental conditions. STM images show the stability of the Pd adlayer at potentials up to 0.8 V vs SHE. A change from ambient conditions to *operando* conditions has no significant effect on the Pd adlayer properties. The change to liquid conditions does not change the island shape, size or distribution compared to STM images recorded under ambient conditions. Especially no increased mobility of the Pd adatoms can be observed, neither a dissolution of pristine or oxidized Pd species that would lead to a change of the morphology of the adlayer. Figure 4.14b shows the STM height profile extracted from 4.14a (marker 1) with a sketch of the surface. The height profile includes a Au(111) step edge and a step onto a Pd/Au(111) island.

The height of the islands is 0.34 nm at all potentials, which is in agreement with the atomic diameter of Pd of 0.34 nm.[Man68] The Au(111) step edge height was measured to be 0.26 nm, 0.02 nm larger than the literature value of 0.24 nm.[Spu+20], which can be caused by adjusting the tip distance too far directly at the step edge, where the height profile exhibits a maximum after which the apparent height gets smaller again.

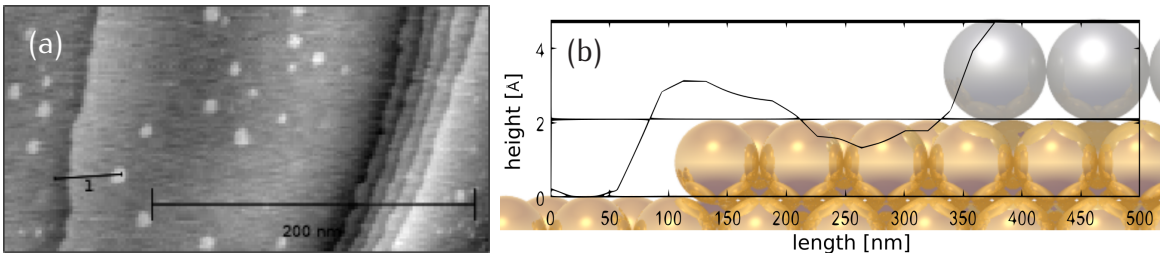

Figure 4.14.: (a) EC-STM image acquired at 0.2 V vs SHE. The line (marker 1) indicates the line along which the height profile was extracted. (b) Extracted STM height profile along the marker in (a) together with a sketch of the surface structure along the height profile. The length axis of the sketch is scaled for clarification and to keep the proportions of the balls that represent the surface atoms.

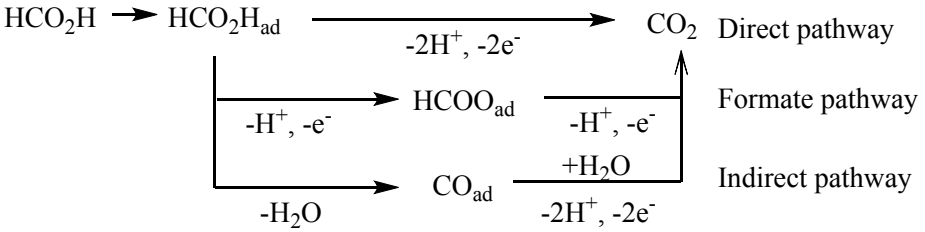

Figure 4.15.: Possible reaction pathways of formic acid oxidation. The direct pathway lead to the formation of CO_2 via direct dehydrogenation of formic acid. The formate pathway has adsorbed formate as reaction intermediate, while the indirect pathway proceeds via dehydration of formic acid and adsorbed CO as reaction intermediate to CO_2.

4.5 Catalyst poisoning during FAO

Relying on the three possible pathways of FAO, shown in figure 4.15, there are three possible adsorbates that could lead to the significant reduction of catalytic activity of the Pd/Au(111) catalyst: intermediately formed formate adsorbed to the catalyst, intermediately formed and adsorbed CO, and the adsorption of the reaction product CO_2.

The experimental onset potential for CO_2 reduction on Au(111) has been measured to ocuur at potentials lower than -0.4 V vs SHE[Hor+87], which is at least 0.2 V lower than the lower potential limit applied in our experiments. On Pd, the onset potential of CO_2 reduction is lower than -0.1 V vs RHE.[Gao+15; Gao+18] Experiments have shown CO_2 reduction charge densities arise at potentials lower than this value.[Guo+17; Che+22b] In comparison to formate, CO is able to adsorb strongly on Pd and does only weakly adsorb on Au(111)[WXS13], which could explain the poisoning of the Pd-based catalyst by CO. However, earlier studies of the FAOR suggested that the indirect pathway, leading to adsorbed CO intermediates, is not dominant on Pd compared to direct and formate pathways.[YP09].

Figure 4.2 shows the CVs of an unpoisoned, pristine Pd/Au(111) sample, pristine

Au(111) and a poisoned Pd/Au(111) catalyst. It can be seen that the catalytic activity of Au(111) for FAO is weak, as no current peak is observed during FAO, comparable to that of the poisoned Pd/Au(111). Au(111) is known to be a weaker catalyst for FAO compared to Pd[CP73; ZW93; Cue+13], leading to less charge transferred during FAO. The weak activity of the pristine Au(111) catalyst can be used as reference for the poisoned Pd/Au(111) system, in which most of the active sites appear to be blocked by the poisoning agent, and thus, show no current peak during FAO, the same behaviour as pristine Au(111).
After the depoisoning of the surface, shown in figure 4.3, the FAO peak potential at 0.47 V vs SHE is in good agreement with the value of 0.42 V that is reported by Kolb and co-workers.[BK96]
The results of the CV experiments in CO containing electrolyte (Figure 4.6) show that the presence of CO can effectively block the catalytic activity towards HER and also suggests that the activity towards catalysis of FAO is blocked by CO, because the Pd sites, both rim and terrace, are deactivated. We assume that CO adsorbed to the Pd sites and block them, so that no other reactands, formate or formic acid in case of FAO and protons in case of HER, can adsorb.

4.6 Raman fingerprint of CO_{ads} on Pd/Au(111)

The chemical nature of the catalyst poison is studied with EC-TERS. The Raman spectra recorded during FAO are shown in figure 4.8. The spectra are recorded at different working electrode potentials, namely at 0.6 V, prior to the oxidation of the Pd islands, and at 1.2 V, after the onset potential of oxidation of Pd. A summary of the discussed relevant Raman modes at different experiments is listed in table 4.2.

Table 4.1.: List of the relevant Raman modes for observation of CO adsorbates on the Pd(island)@Au(111) catalytic system during FAO and in CO saturated electrolyte.

Raman modes				
System	Spot	ν(PdOx) [cm^{-1}]	ν(PdOx) [cm^{-1}]	ν(CO) [cm^{-1}]
FAO	Pd	258	621	2193
FAO	Au	not observed		
CO_{sat}	Pd	-	-	2193
CO_{sat}	Au	not observed		

The spectrum recorded at 0.6 V vs SHE, i.e. prior to the Pd oxidation onset potential does not show any clear bands. However, after ramping the potential to 1.2 V, the spectrum shows bands in the fingerprint region that can be assigned to the formation of oxidized Pd (PdOx) (264 and 620 cm^{-1}), as it has been reported in Raman spectra of PdO.[Chl+17; Dem+03] A strong band at 625 cm^{-1} band was assigned by Demoulin and coworkers[Dem+03] to the presence of the Raman active E_g and B_{1g} vibrations

of PdO. They also found a band at 273 cm^{-1}, and assigned it to PdO, similar to the mode we observe as a shoulder at 264 cm^{-1}. The sharp band at 2192 cm^{-1} can only be observed in the spectra recorded on Pd after reaching the oxidation potential of Pd in the presence of formic acid. The TER spectra recorded on Pd in CO saturated sulfuric acid at potentials below and above the oxidation onset potential of Pd, respectively, also differ in the band at 2192 cm^{-1}, which is only observable in the spectrum acquired at 1.2 V vs SHE, i.e. at sufficient overpotential for Pd oxidation. EC-TER spectra measured in electrolyte without CO or FA, and spectra acquired on Au or below the Pd oxidation potential do not show any bands in the region between 1700 and 2200 cm^{-1}. The band at 2192 cm^{-1} is further investigated because it is only observable in context with CO or FAO on Pd islands.

Potential dependent EC-TER spectra in the region of interest after poisoning of the surface show a relative blueshift of the band around 2190 cm^{-1} of 13 cm^{-1}/V with increasing potential. The shift of the band position could be influenced by the vibrational Stark effect. However, calculated values of the Stark shift on Pd(001) single crystalline surfaces suggest much higher shifts of 45 cm^{-1}/V.[Bag90]

The results indicate a clear correlation between the presence of the 2192 cm^{-1} mode and the presence of a poisoning species on the Pd islands. Possible intermediates during the FAO that can adsorb to Pd and lead to catalyst poisoning are formate and CO. The appearance of the band of interest in electrolyte saturated with CO without presence of FA supports the assumption that the band of interest can be assigned to the presence of adsorbed CO on the Pd islands. The vibrational modes of formate on Au were calculated at zero electric field by the group of Marc Koper.[BSK05] They found vibrational mode for HCOO-Au at 1321 and 1562 cm^{-1} with a Stark tuning of 21 cm^{-1}/V, a mode for COOH-Au at 1748 cm^{-1} with a Stark shift of 0 cm^{-1}/V, and additional C-H and O-H stretching modes at 3000 cm^{-1} and 3500 cm^{-1}, respectively. Even though the studied system was the adsorption on Au instead of Pd/Au, it is unlikely that a change in the metal substrate would lead to a blueshift of 400-500 cm^{-1}.

Former studies on Pd single crystalline surfaces could not demonstrate the occurrence of the CO pathway on low-index single crystal or complete monolayer substrates.[BK96; ULL09] However, in this study, we do not use a Pd single crystal or full Pd monolayer as substrate, but a Pd submonolayer on Au that has a high defect density and unsaturated surface Pd atoms, which is more prone to oxidation than the systems used in reference studies. The high number of undercoordinated Pd atoms at Pd/Au rim sites leads to a lowered oxidation barrier of the 2D island structures compared to single crystals.[El-02] The oxidation prone 2D Pd submonolayer, that we use may result in the presence of surface oxides in a wide potential range, and thus, lead to an essential difference between the studies of single crystalline Pd surfaces that could not show the presence of CO during operation in FAO. We speculate that (partial) surface oxidation of the Pd adlayer could play a role driving the FAO towards the indirect pathway, leading to significant accumulation of CO and, thus, poisoning of the Pd/Au(111) catalyst.

We assign the band at 2192 cm^{-1} with a FWHM of 31 cm^{-1} to the CO stretch mode of

CO adsorbed on Pd islands. Reference studies on Pd low-index faces suggest lower Raman shifts of the CO stretching mode.[MXW12; Mor+05; Zei+16] The Raman shift of the band of interest in our experiment is independent of the origin of the CO, either from direct CO introduction into the electrolyte or formed during FAO. Besides the origin as intermediate product during the indirect pathway of FAO, the backreduction of CO_2, the final product of FAO, to CO, which then leads to catalyst poisoning can be ruled out in the potential window that we use in our experiments. The reduction of CO_2 requires potentials at least 0.2 V lower than the lowest potential used in our experiments.[Gao+15; Gao+18]

The shift of the CO_{ads} stretch vibration is strongly coverage dependent. IR experiments of Bradshaw et al. found the CO vibrational mode at 1895 cm^{-1} for a coverage of $\Theta<0.05$, i.e. very low CO coverage.[BH78] For a higher coverage of $\Theta= 0.61$, they found a blueshift of 88 cm^{-1} to 1983 cm^{-1}. They explain this coverage dependency by the compression of the ordered CO adsorbate structure at higher coverages that leads to a decrease in adsorption energy and, thus, in a blueshift of the vibrational mode. Another factor that influences the Raman shift of the CO stretch vibrational mode is the electronic environment of the adsorbed molecule. Different electrode materials as well as different supporting materials for Pd exhibit significant differences in the shift of the CO stretch mode. The group of Weaver studied the potential dependent surface enhanced Raman response of adsorbed CO on Pd- and Pt coated gold electrodes.[LW87] They found two different modes at 1984 and 2083 cm^{-1}, which they assigned to bridge and atop adsorbed CO stretch vibrations, a difference of 99 cm^{-1} between the two adsorption sites. Other studies on the adsorption site dependent Raman shift of the CO stretch vibration show a band at 1807 cm^{-1} on threefold adsorption sites of Pd.[Hof83; Tue90] Higher CO coverages between $\Theta= 0.5$ and $\Theta= 0.6$ on bridge and atop sites of Pd(111) show significant larger shifts of 1966 cm^{-1}[Tue90; Tue+90] and 2110 cm^{-1}[Gio+02], only 66 cm^{-1} lower than the lowest frequency of 2176 cm^{-1} at -100 mV vs SHE reported in our study. *Ab initio* calculations of our collaborators at EPFL reveal the highest CO stretching vibration, calculated at zero charge, to come from CO adsorption on coordinatively undersaturated (cus) Pd sites on PdO_2(111) and from the adsorption at 4-fold Pd sites on PdOx/Au(111). Weaver at al. have reported a blueshift of the band upon potential increase.[LW87] Moreover, they have observed the vanishing of the CO mode in potential dependent IR spectra at potentials above 0.6 V, whereas they found the mode in SER spectra at potentials up to 0.9 V, i.e. at potentials higher than the oxidation potential of Pd. They explain that in SERS they sense only the minority of CO adsorbates that are less oxidation prone and are situated close to SERS active defect sites of the surface. In our case, we also observe the Raman active mode at potentials up to 1.2 V, i.e. at a (partially) oxidized surface. We speculate that the (partial) oxidation of the Pd islands causes the reported blueshift of the CO stretching mode compared to previous studies on pristine Pd surfaces, resulting from an interaction between the oxide layer and CO, forming a coordination intermediate between CO and CO_2 that would strengthen the CO stretch vibration, leading to a blueshift of the vibrational mode. Support to this hypothesis comes from the observation

of the CO band only after (partial) oxidation of the Pd adlayer structure at 1.2 V.

The potential dependence of the CO stretch vibration can be caused by a potential dependent change of the PdOx layer. This hypothesis is supported by simulation results, that show significantly larger frequencies on adsorption at both, supported (2129 cm^{-1}) and unsupported (2162 cm^{-1}) Pd oxides, compared to the frequencies calculated for CO adsorption on pristine Au(111) (2056 cm^{-1}) and reduced Pd/Au(111) (1915 cm^{-1}). The Raman shift of 2162 cm^{-1} originating from CO adsorption on PdO_2 is within the FWHM of the band found in our TER experiments, indicating CO adsorption on larger PdO_2 domains generated by the high oxidation overpotential at 1.25 V vs SHE. The presence of PdO_2 is supported by the Pourbaix diagram of Pd, indicating the formation of PdO_2 at high potentials.[MM10] After reaching a potential just below the oxidation potential of Pd in the cathodic direction, many undercoordinated Pd atoms remain oxidized because of the kinetics of the reduction, giving raise to the blueshift of the CO vibration. At even lower potentials, and higher overpotential for Pd reduction, the oxide layer is smaller compared to higher potentials, leading to a relatively smaller oxide layer and blueshift of the CO mode. A change in the PdOx layer would, according to our hypothesis, lead to a change in the CO-OxPd interaction. The inherent high defect density of our Pd/Au(111) model catalyst is crucial for the appearance of the oxide layer that is stabilized by the CO adsorbates.

Even though the Raman shift of the modes reported in previous studies and mentioned throughout this discussion are smaller by 90 cm^{-1} compared to the mode at 2192 cm^{-1} that we found in our EC-TERS experiments, the studies show that the actual Raman shift of the band is strongly influenced by the amount of adsorbed CO, the applied potential at the electrode and the electronic environment of the adsorbates. We do not quantify the amount of CO adsorbed on the catalyst and did not test catalysts with different surface morphologies, i.e. Pd islands, mono- or multilayers. Nonetheless our results in formic acid, CO and without both in the electrolyte strongly imply the presence of CO that blocks the catalyst for FAO. Further results on the isotope effect of CO and the study of a greater variety of Pd adlayer morphologies could allow for further interpretation of the unusually high Raman shift of the 2192 cm^{-1} band.

Moreover, going away from sulfuric acid as supporting electrolyte to perchloric acid could allow for better results as no additional adsorbing species like sulfate and bisulfate would cover the Pd surface sites. Even though the TER spectra presented in this study could not show any presence of (bi-) sulfate on the Pd islands, the choice of a less adsorbing supporting electrolyte would make a discussion of the CO band easier. First experiments in $HClO_4$ were carried out. The resulting EC-TER spectrum is shown in figure 4.16.

Four bands are present in the spectral range of interest at 2174, 2182, 2189 and 2203 cm^{-1}. Without the presence of additionally adsorbing species in the supporting electrolyte, it could be possible to resolve the adsorption of CO to different surface sites that exhibit different vibrational frequencies and therefore leads to multiple Raman bands.

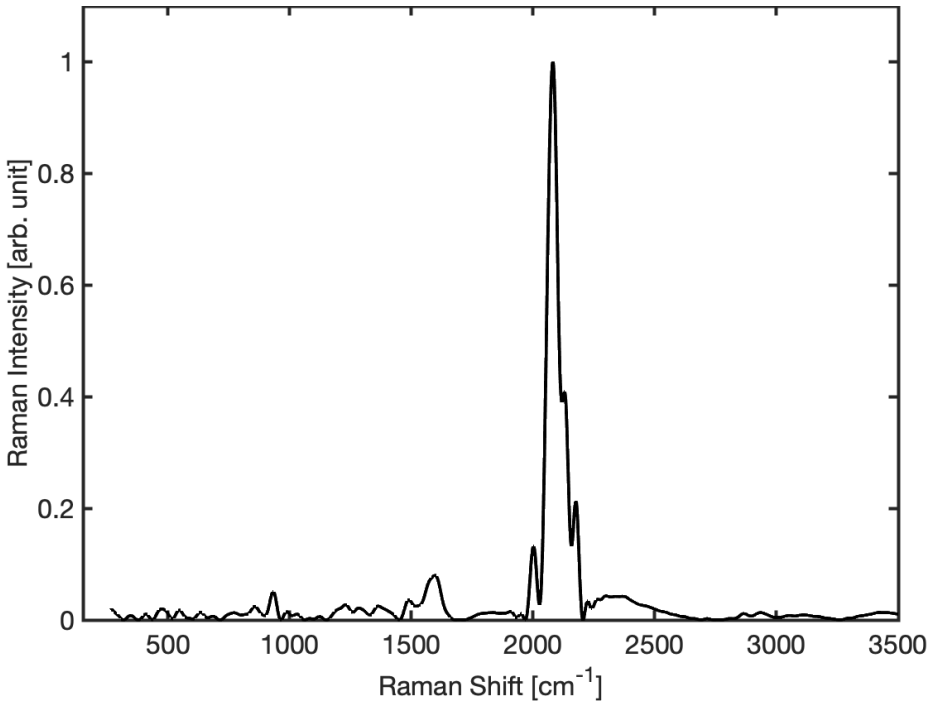

Figure 4.16.: EC-TER spectrum recorded on Pd/Au(111) after oxidation in CO saturated perchloric acid as supporting electrolyte.

4.7 Summary and Outlook

We show in our experiments that significant surface poisoning can happen on Pd/Au(111) model catalysts during FAOR. Going along with the poisoning, the FAO charge density, i.e. the catalytic activity, drops from 7 $\mu\mathrm{As/cm^2}$ to 1 $\mu\mathrm{As/cm^2}$. The activity can be (partially) restored by electrochemical depoisoning of the surface by ramping the potential and CO stripping. The nature of the poisoning species was further investigated by EC-TERS. EC-TER spectra recorded prior to and after poisoning of the catalyst during FAO reveal significant spectral differences. A small band at 2192 $\mathrm{cm^{-1}}$ appears after one cycle of FAO. In reference experiments, the same band was shown in CO saturated electrolyte at high potentials applied to the model catalyst. We assigned the band to the $\mathrm{CO_{ads}}$ stretch mode. Despite the fact that bands reported in previous studies show lower frequencies, calculations of CO adsorbed to pristine Au(111), Pd/Au(111) and oxidized Pd (supported and unsupported) support the assumption that the unusually high Raman shift reported in this study is due to (partial) oxidation of the Pd adlayer. From simulations, a frequency of 2163 $\mathrm{cm^{-1}}$ was obtained, that is within the FWHM of the band at 2192 $\pm$ 31 $\mathrm{cm^{-1}}$ recorded at 1.25 V vs SHE. We assume that the interaction between the adsorbed CO and the oxide layer influence the stretch vibrational mode of CO, leading to a blueshift compared to the bands reported on pristine Pd and

Pd/Au(111). The band of interest is not observable prior to surface oxidation in FAO experiments, which supports the hypothesis, that FAO runs through the direct pathway on reduced Pd catalysts. However, our results indicate that, once Pd is (partially) oxidized, the FAOR is driven to the indirect pathway, leading to intermediate production of CO and its adsorption on the surface. The presence of PdOx species at high oxidation overpotentials can be observed in the respective bands in the EC-TER spectra at 258 and 621 cm^{-1}.
For the use in DFAFCs, we therefore conclude that it is necessary to carefully avoid oxidation of Pd based catalysts that leads to the indirect pathway of FAO, to maintain the electrocatalytic activity.

A further understanding of the nature of the poisoning species could be gained in TERS experiments with isotopically pure CO, to study the isotope effect of the poisoning agent and the band of interest. Even though the experimental results and comparison between CO containing and CO free electrolyte strongly suggest that the catalyst poison is in fact CO, a shift of the band through the isotope effect would be another confirmation.
First attempts have been made to map the surface and directly correlate surface topography, i.e. Pd islands on the gold support, with the TER response of the system during FAO. Yet, the system was not stable enough to obtain meaningful TERS maps on the model catalyst during FAO. More progress would allow to gain insight into the reactive sites of FAO on the model catalyst. Together with a change of the supportive electrolyte, it could be possible to map the surface with regards to the different CO adsorption sites with EC-TERS.

Part V

Surface fluorescence microscopy: Development and application to measure the potential dependent surface pH in an electrochemical cell

5

Surface fluorescence microscopy: Development and application to measure the potential dependent surface pH in an electrochemical cell

This chapter shows the development of a new technique to measure the potential dependent surface pH in an electrochemical cell with help of fluorescence microscopy.

Contents

This chapter is based on a collaboration between Daniel Ohm (MPIP), Tobias Binninger (ICGM), Katrin F. Domke (MPIP), Adrian Heinritz (ETHZ), Juan Herranz Salaner (PSI), Albin Lahu (JGU), Xiaomin Liu (MPIP), Paramaconi Rodriguez Perez (CIC EnergiGUNE) and Qiqi Yang (MPIP). The work presented in this chapter is the work of Daniel Ohm.

5.1 Introduction

In this study we focus on the experimental proof of the existence of Protons at the electrode electrolyte interface in a bulk alkaline solution. The verification of this contradictory behaviour of the proton concentration, generated by water splitting close to an electrode under the influence of an electric field is of great importance to better understand and improve even simple electrochemical reactions that show a pH dependence in their kinetics or thermodynamic properties. The knowledge of the conditions in an electrochemical cell during operation is crucial for the unserstanding of reaction pathways and kinetics of specific reactions and therefore should be considered in the choice of suitable electrocatalysts for devices such as fuel cells and electrolyzers. One property of the electrochemical device is the pH. Many electrode reactions show a strong kinetic dependence on the pH of the electrolyte, especially reactions involving consumption or production of H^+ or OH^-. Electrochemical reactions that involve the transfer of protons are for example the hydrogen oxidation/evolution reactions (HOR/HER)[Str+16; Bri+20], the oxygen reduction/evolution reactions (ORR/OER)[BRM07; Li+13], formic acid oxidation (FAOR)[PHF14; Joo+13] or the CO_2 reduction reaction (CO_2RR)[Goy+20]. All of these reactions are of great relevance for fuel cell driven energy conversion and are highly pH sensitive. Yet, in most cases the pH of the bulk electrolyte is considered in theoretical and practical

The general effect of pH changes on electrode reactions is manifold. Fundamental properties like the binding energy of reaction intermediates or the level of the energy barrier[Kel+20; LSC19; Ros+13] are effected as well as the number of free reactive sites due to the specific adsorption of ions.[Zuo+18; Joo+14; AHK17] However, the current state of scientific discussion about local pH changes on the electrode-electrolyte interface is focused on medium pH electrolytes and the change of H^+ or OH^- concentrations due to proton consumption/production through reactions at the electrode and the comparably slow mass transport of H^+ or OH^- from the bulk medium pH electrolyte to the interface.[Bri+20; Per+15; BHF17] Nonetheless, studies conclude that the precise knowledge and/or control of the pH at the electrode-electrolyte interface is crucial to tune the electrocatalytic activity of reactions like the ones mentioned before.[Che+22a] here we extend the present state of scientific considerations and include not only a system in thermodynamic disequilibrium in the considerations, but show the existence

of protons at the interface between an alkaline solution and the electrode in the equilibrium state. We focus not only on changes of the local surface pH due to the consumption and production of protons by reactions at the electrode but also on the pH change by variations in the applied potential, as predicted by the Frumkin effect. We present a technique to directly measure variations in the local proton concentration by the use of a pH sensitive fluorophor in combination with highly sensitive fluorescence microscopy and electrochemical methods.

5.2 Experimental details

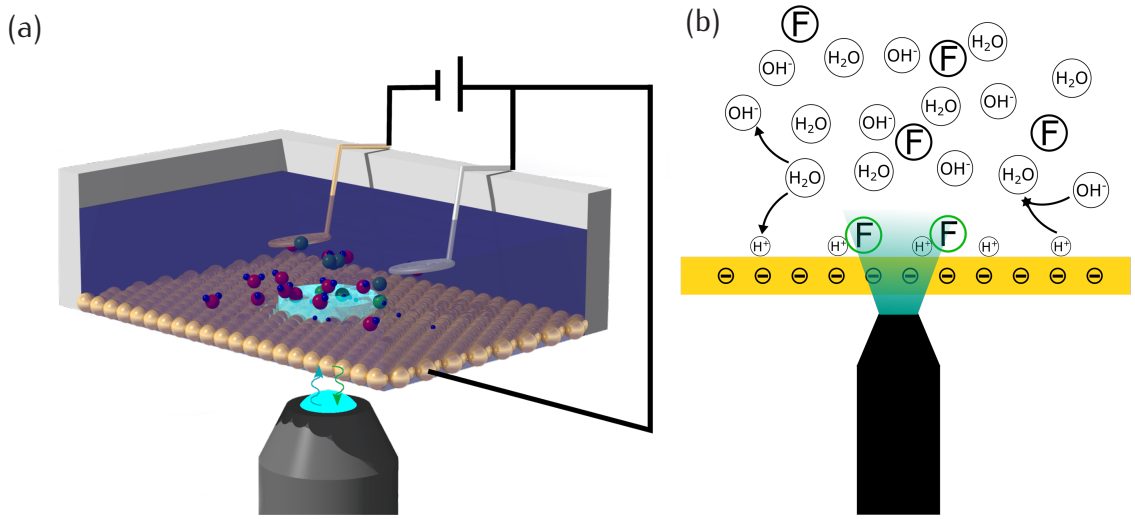

Figure 5.1.: (a) Drawing of the EC-FM cell setup. (b) Schematic of the experiment. The oil immersion objective illuminates the sample from underneath the electrode-electrolyte interface. A thin (10 nm) Au layer is used as WE, the focus size in z direction, i.e. perpendicular to the electrode surface, of the objective is 600 nm and covers not only the interface but reaches into the bulk solution. The pH dependent fluorescence of the fluorophores F is measured as function of the applied potential at the WE.

The figures shown in 5.1 show the working principle of the electrochemical fluorescence microscopy (EC-FM) method. The EC-FM cell is equipped with a CE and RE and a thin Au film WE. The WE is illuminated from the bottom and the fluorescence light is captured in epi configuration through the same objective. Water splitting close to the interface in the EDL leads to a potential dependent increase in proton concentration in the EDL that is sensed by the pH sensitive fluorophor.
Electrochemical fluorescence microscopy experiments are carried out in a home-built electrochemical cell to fit in the detection path of the home-built epifluorescence wide-field microscope that we use in the experiments presented in this chapter.
The electrochemical microscopy cell and glassware is cleaned by storing them in $KMnO_4$ solution for 24 hours. After that, they are kept in diluted acidified H_2O_2 for 15

minutes until all leftover $KMnO_4$ was reduced. Subsequently, all glassware and the cells were boiled in MilliQ water (Millipore, 18.2 MΩ, 3 ppb TOC) three times for two minutes.
A 170 µm thick glass slide, sputtered with a 10 nm thin Au layer on a 2 nm Cr sticking layer is glued to the bottom of the electrochemical cell with non-fluorescent UV glue. A drawing of the cell is shown in figure 5.2. The cell is cut on one side to allow for electric contacting of the Au film WE with a Au wire outside of the electrolyte. A hole with a diameter of 9 mm provides contact of a defined WE area with the electrolyte. A Au wire CE (0.5 mm diameter, 99.997% trace metal basis, Alfa Aeasar) and a H-loaded Pd wire (0.5 mm diameter, 99.95% metal basis, MaTecK) RE (for preparation see chapter 3) are attached to cell. The cell volume of 18 ml was filled with 0.1 M NaOH (Merck), mixed with 0.2 µL of a pH sensitive LysoSensor Green DND-189 (Thermo Fisher, $\lambda_{\mathrm{ex}} = 443\mathrm{nm}, \lambda_{\mathrm{em}} = 505\mathrm{nm}, \mathrm{pKa} = 5.2$) fluorophor.

An epifluorescence configuration is used to illuminate the sample and collect the fluorescence through one objective lens (HCX APO 100x, NA 1.47 oil immersion, Leica) placed on the bottom site of the sample cell. The excitation laser beam ($\lambda_{\mathrm{ex}} =$ 488 nm, Omicron, incident power: 5 mW, irradiance 0.47 kW/cm^2) is focused on the back focal plane of the objective, shining through the thin Au film with focus at the electrode-electrolyte interface. The fluorescence emission light is focused and imaged on a sCMOS camera (PCO edge 4.2) with a pixel size corresponding to 65 nm in the sample plane. The vertical (z) focus of the incident laser beam is 600 nm.
Focusing is done with white light illumination on a thin scratch on the Au surface layer. The laser is switched on directly before the image acquisition and shut off directly after finishing the measurement to avoid unnecessary irradiation of the dye. The thickness of the EDL is, depending on the size of the involved ions, in the range of several nm,[BKI01] which is much smaller than the focal size in the direction perpendicular to the interface. To obtain surface specific fluorescence results, the fluorophor is required to be non-fluorescent in the bulk solution, which is guaranteed by the pH sensitivity of the used fluorophor. In 0.1 M NaOH solution (pH 13), the fluorophor LysoSensor Green is deprotonated (pKa 5.2) and the fluorescence is quenched. According to the Frumkin effect described in chapter 2, the accumulation of protons happens in the EDL at potentials negative of the point of zero charge (pzc). The fast deprotonation of the dye as it reaches the bulk pH environment, as a result of the difference between pKa 5.2 and pH 13, and the resulting quenching of the fluorescence allows for surface (EDL) sensitive pH measurements despite the large focal size of 600 nm compared to the EDL thickness.
The rate of image acquisition is, if not stated otherwise, 5 Hz with a probed area of 1.06 $\cdot 10^{-5}\,\mathrm{cm}^2$.
The electrochemical control is done with an Autolab Potentiostat (Metrohm, PGSTAT30) equipped with a Metrohm Autolab Differential Electrometer Amplifier, controlled by NOVA software (Version 2.1, Windows 7). The potentials reported in this study are referred to the PdH potential.
Microscopy acquisition and potential control is started simultaneously to correlate the

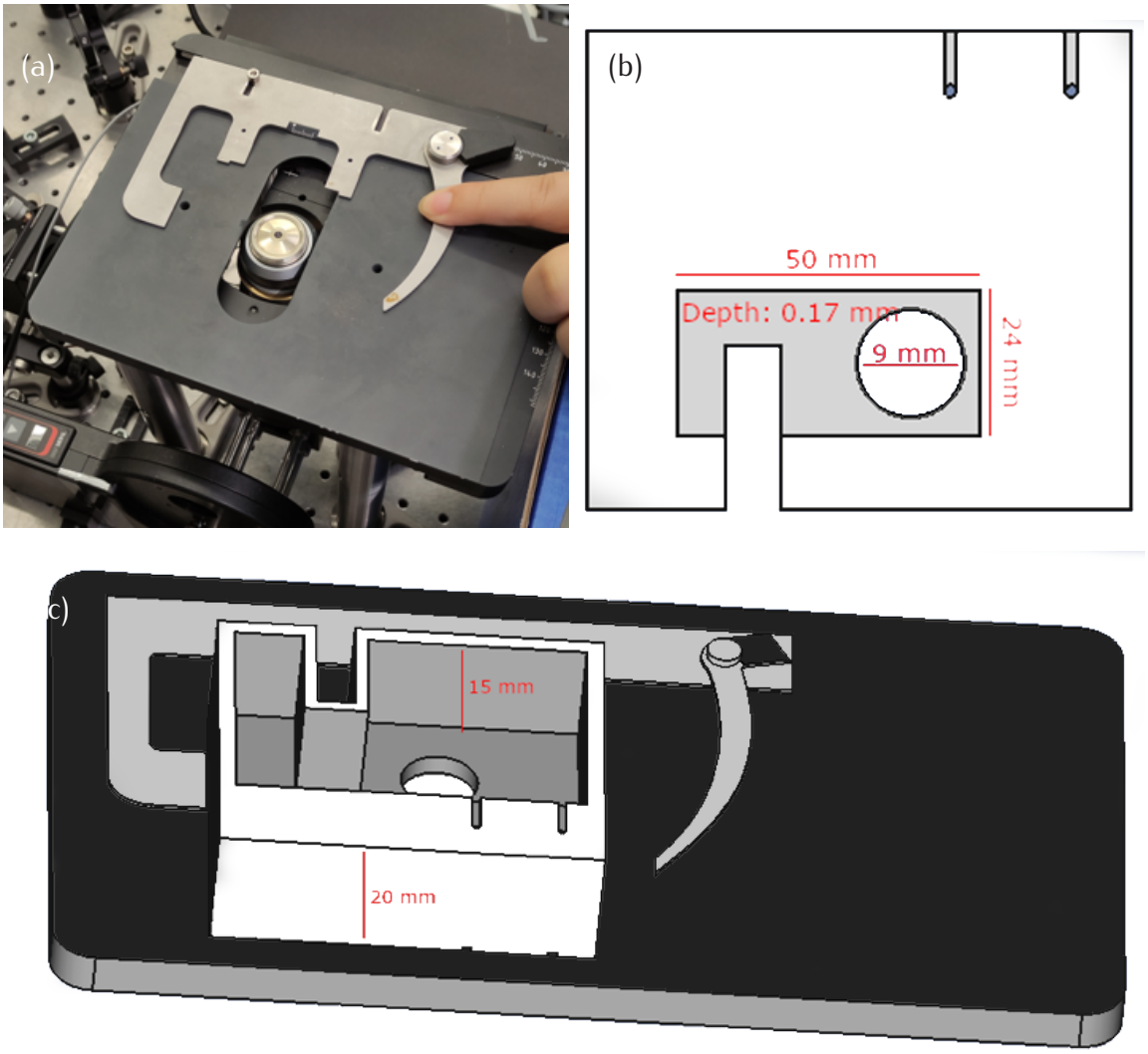

Figure 5.2.: (a) Picture of the home-built microscopy stage. The sample is illuminated from the bottom. (b) Drawing of the bottom view of the home-built electrochemical cell for surface fluorescence microscopy experiments. (c) Drawing of the top view of the cell mounted on the stage.

fluorescence signal with the applied potential and current signal.

5.2.1 Data processing

The fluorescence signal is evaluated by processing the acquired images. The mean gray value is used as a measure for the fluorescence. The time-domain of the fluorescence signal is converted to the applied potential using the potential-time correlation of the electrochemical data. The image data is processed with ImageJ software (Version 1.53f51). The obtained fluorescence data and electrochemical data are processed in Matlab (Version R2022b).

The raw fluorescence data are baseline corrected with an asymmetric least square method. Outliers (single datapoints with high deviation from a moving mean of a width of 20 datapoints) are automatically removed (for details see appendix). The fluorescence on- and offset potentials are determined by extrapolating the intersection between a linear fit at the maximum slope and the zero baseline.
Correlation of the experimental fluorescence data and the surface pH is done by comparing the normalized fluorescence intensity with data obtained from pH dependent bulk fluorescence spectroscopy measurements. The data were fitted by a nonlinear sigmoidal curve.

5.3 Experimental results

The basis of this new approach to measure the local surface proton concentration at an electrode is the pH dependence of the employed fluorophor. Here, we use the commercial dye LysoSensor Green DND-189 to probe the acidity of the interface in a bulk alkaline solution. The structure and the absorption/emission spectra of the fluorophor are shown in figure 5.3.

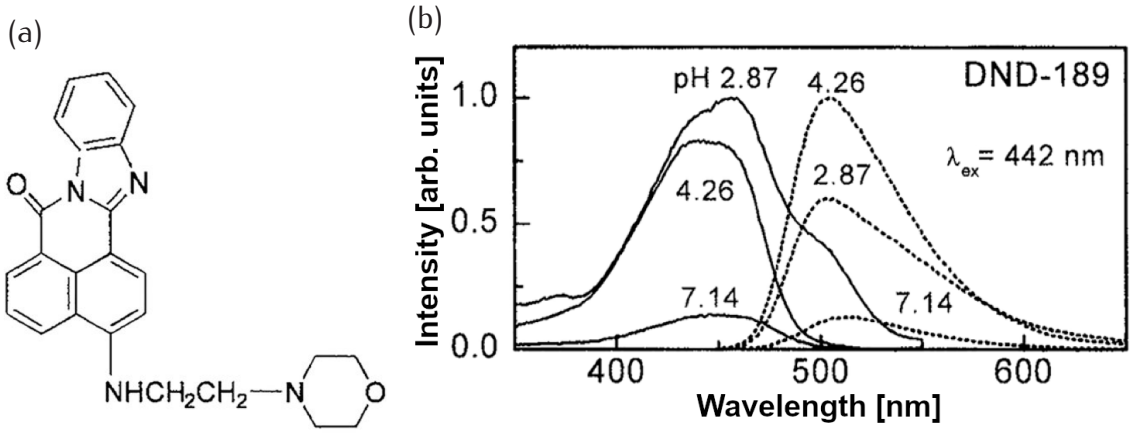

Figure 5.3.: (a) Molecular structure of LysoSensor Green DND-189. (b) Fluorescence excitation and emission spectra recorded at different pH values in commercial buffer solutions. Image adapted from [Lin+01].

The dye shows no fluorescence in alkaline media. After protonation (pKa = 5.2), the dye shows fluorescence with a maximum at 510 nm after excitation. The pH dependence measured with fluorescence spectroscopy is shown in figure 5.4. The bulk pH was adjusted by mixing different amounts of NaOH and H_2SO_4 to keep the experimental conditions as simple as possible and avoid the use of different salts in a buffer solution. The pH was measured with a pH meter directly before the spectroscopy. The data show an increase of the fluorescence intensity at an emission wavelength $\lambda\mathrm{em}$ of 510 nm, with decreasing pH, starting from a pH of 8.2. The experimental pKa (pH at 50%

fluorescence intensity) is 6, 0.8 decades higher than the value obtained from the vendor (pKa = 5.2). The fluorescence maximum is reached at pH 4.5.

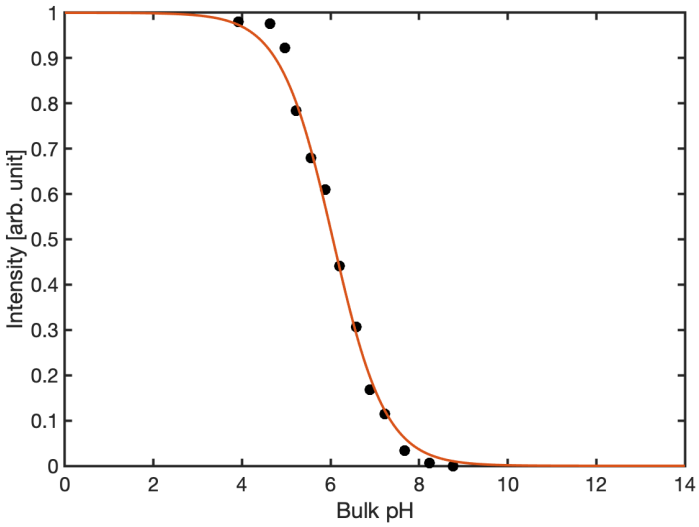

Figure 5.4.: Fluorescence intensity of LysoSensor Green DND-189 as function of the pH obtained from fluorescence spectroscopy in solutions of different bulk pH. The red line shows the sigmoidal function to fit the datapoints.

We run EC-FM measurements in bulk alkaline and acidic solutions to probe the dye behaviour in the microscope setup at extreme pH values. At pH 13 (0.1 M NaOH) we could not observe fluorescence, whereas at pH 1 (0.1 M H_2SO_4), a bright fluorescence signal was observed without potential control.

To proof the concept of the accumulation of stable protons, i.e. protons with a lifetime that allows for protonation of the dye, at the interface of a metal electrode and a bulk alkaline electrolyte, we run the EC-FM measurements under EC control to observe changes in the fluorescence response upon potential changes caused by the formation of interfacial protons and protonation of the fluorophor. The localization of the origin of fluorescence in the interface, i.e. the EDL, was proofed by focusing into the bulk solution while changing the potential. No fluorescence signal could be observed.

Figure 5.5 shows the fluorescence signal of the fluorophor in pH 13 at different potentials (●) and the response of a reference measurement without dye (▲). The potentials are changed stepwise after three datapoints are recorded for 180 s at each potential.

The observed fluorescence (●) starts to increase slightly from a normalized intensity of 0 at 600 mV to 0.06±0.02 at 100 mV. With a further decrease in potential, the fluorescence signal increases more strongly to 0.15±0.02 at 0 mV. A further decrease of 100 mV is followed by a strong fluorescence increase to bright fluorescence of 0.98±0.02 arb. unit at -100 mV. With subsequent increase of potential to the starting value of 600 mV, the fluorescence signal drops back to 0. The decrease is fluorescence is less steep than the increase. At 200 mV in cathodic direction, the fluorescence signal is 0.04±0.01, whereas the fluorescence signal is 0.13±0.02 at 200 mV in the anodic direction.

In the reference measurement without dye in the electrolyte (▲) no significant change

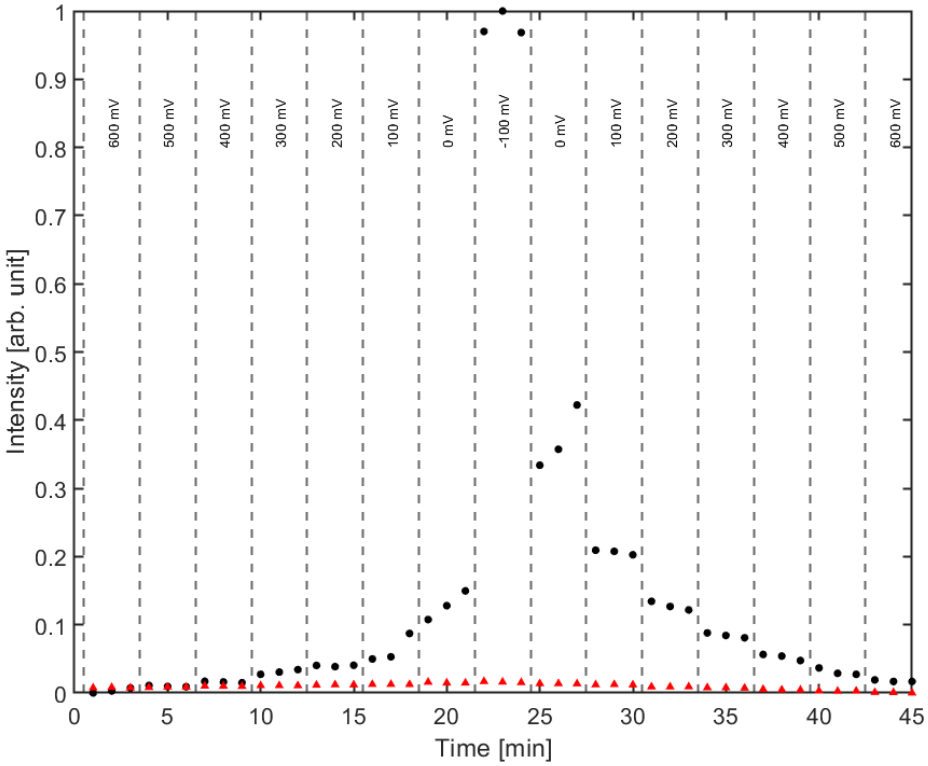

Figure 5.5.: EC-SM potential step experiment with dye (●) and reference measurement without dye (▲). The applied potential was changed stepwise after 180 s each. During one potential set, 3 images were acquired, each after 60 s.

in the signal is observed upon potential change.
Two fluorescence images, corresponding to fluorescence intensity 1 (recorded at -100 mV) and intensity 0 (recorded at 600 mV) are shown in figure 5.6. In further experiments, the filters of the setup were changed to avoid saturation of the camera, that can be seen in figure 5.6b.

To obtain a better time (potential) resolution of the fluorescence, we acquire images during CV scans. We cycle the potential between 600 mV and -80 mV with a scan rate of 25 mV/s. Every 200 ms, one fluorescence image is acquired, resulting in 1 frame per 5 mV. A full set of experimental EC-FM data is shown in figure 5.7.

Figure 5.7a shows the fluorescence signal recorded during two CV cycles in bulk alkaline (pH 13) media with (black) and without (red) dye to be able to assign the measured fluorescence signal to the dye fluorescence. Without dye, there is no significant change of fluorescence with changes in potential. However, under the same experimental conditions but with fluorophor in the cell, a strong fluorescence signal is observed with decreasing potential. The peak fluorescence is reached in the lower CV turning point of -0.08 V in both cycles. Figure 5.7b shows the corresponding potential and current vs time traces, while the conventional representation of the CV is shown in figure 5.7c. From the CV, it can be seen that in the potential region, in which fluorescence occurs, no significant current flow is detected. The current that can be seen in the negative sweep of the CV is assigned to the ORR in alkaline media.[DGB67]

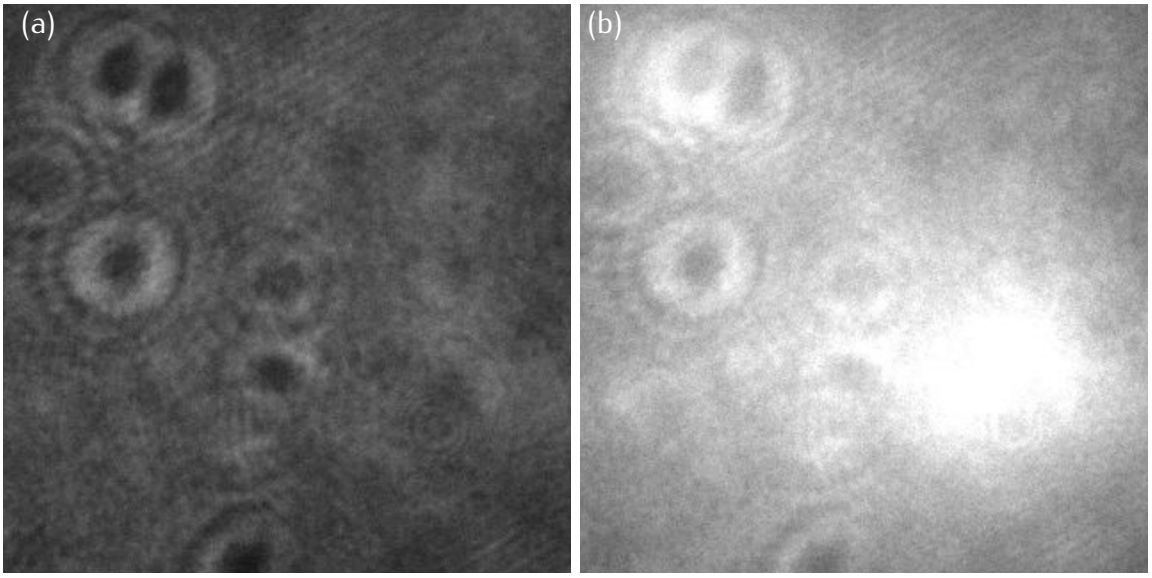

Figure 5.6.: (a) Fluorescence image acquired at 600 mV in pH 13 solution with 0.2 µM dye. (b) Image acquired on the same sample after stepwise potential reduction to -100 mV.

Because of space limitations in the experimental setup, we cannot fully avoid the diffusion of oxygen into the cell and the electrolyte. At the start of the experiment, the electrolyte is purged with Ar, but the cell is open to the environment during the experiment, therefore the ORR cannot be excluded but only held as small as possible by covering the cell with an Ar blanked during the experiment. The CV experiments show that the system reacts fast enough to the potential change to render possible the detection of fluorescence that results from the protonation of the fluorophor at the interface.

Important for the use of the surface microscopy method is the stability and reversibility of the fluorescence signal with time and with potential cycles, i.e. fluorescence on/off cycles. To test stability and reversibility, we run an experiment over five CV cycles with a total duration of 5 minutes and evaluated the changes in the fluorescence signal and in the current response of the system to proof its electrochemical stability. Figure 5.8 shows the fluorescence signal (black), the current response (red) and the respective fits of the peaks. Even though the fluorescence 'peaks' are not really peaks, but an increase and decrease of the signal with the potential up to a certain turning point, we use Lorentzian fit functions to estimate the FWHM and integrated the area of the fluorescence signal to study the fluorescence behavior during the experiment.

We observe a decrease in the fluorescence intensity with increasing number of cycles. The peak intensity of the first cycle is 290 arb. units, decreasing to 250 arb. units in the fifth cycle. The FWHM of the fitted peaks increases from 317 mV to 333 mV from cycle one to five. However, the peak area follows the decrease in peak intensity, starting at 1790 arb. units in the first cycle and decreases to 1330 arb. units in the last cycle of the experiment. The decrease in fluorescence signal is not correlated with a change in the current response. The charge density during the fluorescence 'on' state remaines constant at 760 $\mu As/cm^2$ over the five cycles. The peak current density also

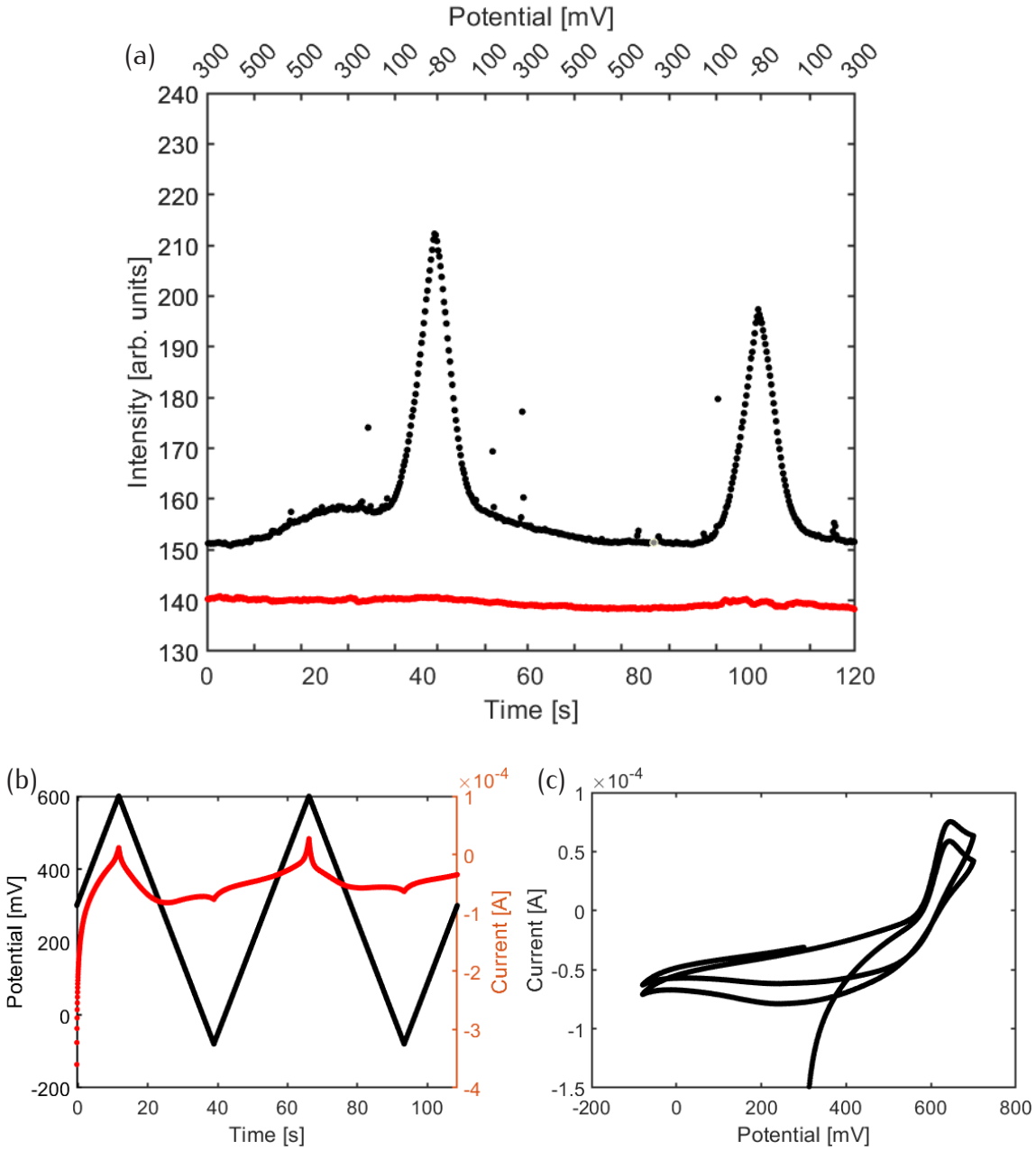

Figure 5.7.: (a) Fluorescence signal of LysoSensor Green DND-189 in bulk alkaline media on a Au(111) under electrochemical conditions (black) and the corresponding reference measurement without dye (red). (b) Applied sawtooth potential during the two CV cycles (black) and corresponding current response of the WE (red). (C) CV in conventional representation.

stays at a constant level of 90 $\mu A/cm^2$. The fluorescence signal shows a change in the asymmetry of the peaks. The first three peaks show a tiny shoulder on the increasing side of the fluorescence signal, whereas the last two cycles show a small shoulder on the decreasing side.

To understand the experimental results and the behavior of the fluorescence further, we examine the fluorescence on- and offset potentials and maximum slopes. Figure 5.9 shows the construction of the onset potential. We define the intersection between the

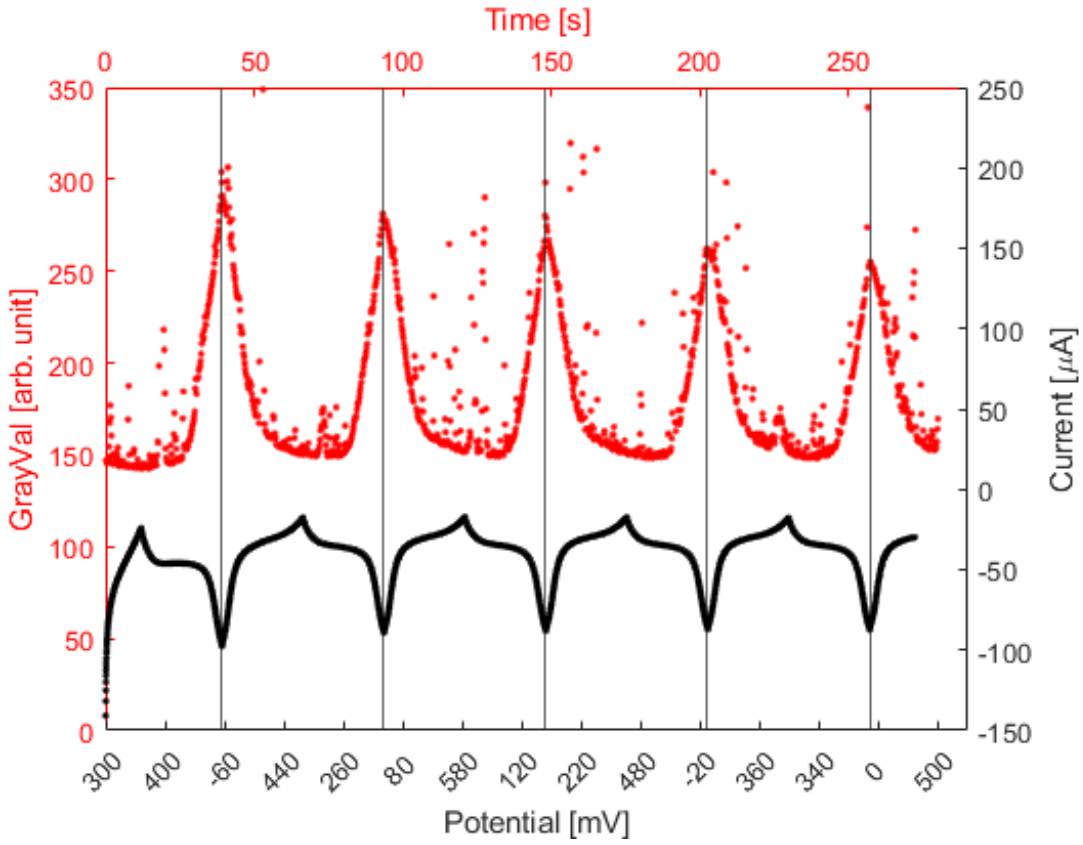

Figure 5.8.: Fluorescence signal as function of the applied potential during five consecutive CV scans in a potential range between 600 and -80 mV (red) and corresponding current (black).

slopeline of minimum (or zero) slope and the slopeline of maximum slope as the onset of the fluorescence increase and, constructed with the maximum negative slope, for the offset of the fluorescence response to obtain a reproducible way to estimate the on- and offset potentials. The onset potentials are widely scattered over different samples, independent of the experimental conditions such as potential limits, duration of the experiment or scan speed. A set of experimentally determined on-/offset potentials and slopes is listed as an example in table 5.1.

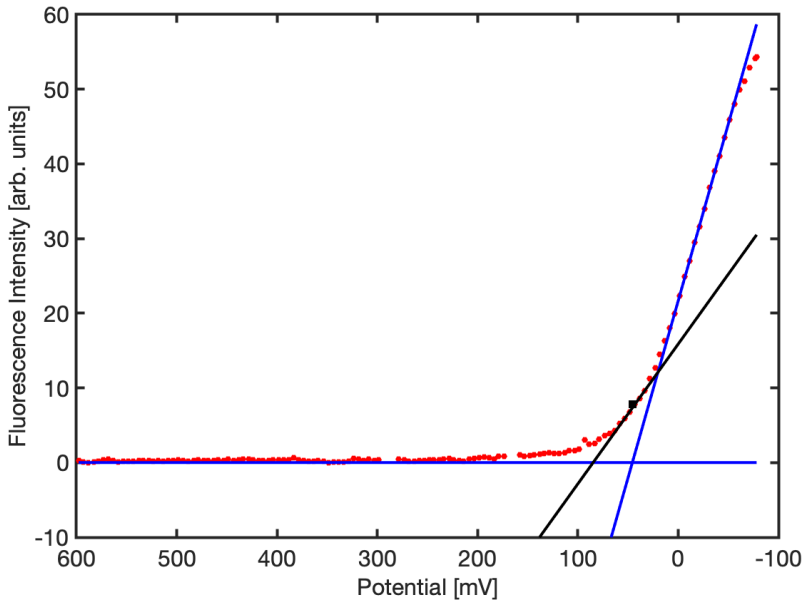

Figure 5.9.: Fluorescence signal as function of the applied potential of one half cycle of a CV from 600 to -80 mV (red). Linear fit functions at the point of maximum and minimum slope of the signal (blue). The black square indicates the constructed fluorescence onset potential with the onset slope drawn as black line.

Table 5.1.: Example list of on-/offset potentials and slopes of different samples at the same or different experimental conditions like potential limits and experiment duration.

Example list of on-/offset potentials and fluorescence slopes					
Exp	Limit [mV]	Scan Rate [mV/s]	Onset [mV]	Offset [mV]	On-/offset Slope [counts/mV]
1	600/-80	25	55	40	0.4/0.5
1	600/-80	25	51	59	0.4/0.4
2	700/-80	25	88	77	0.4/0.4
2	700/-80	25	89	71	0.4/0.5
3	600/-80	25	255	395	0.4/0.3
3	600/-80	25	281	590	0.5/0.2
4	400/0	25	151	255	1.7/1.2
4	400/0	25	170	-	2.1/-

The onset potentials are in a range between 51 mV and 281 mV. The maximum slopes of the increasing and decreasing fluorescence signal lie in a range between 0.2 counts/mV and 2.1 counts/mV.
In addition to the finding that the onset potential and maximum slopes of the fluorescence increase are widely scattered, we found that within one experiment, upon changing the upper potential limit and increasing the experiment time, a second fluorescence signal arises whose onset potential is different. This finding is shown in figure 5.10.

It can be seen that, starting at the third consecutive CV (upper potential limit 800

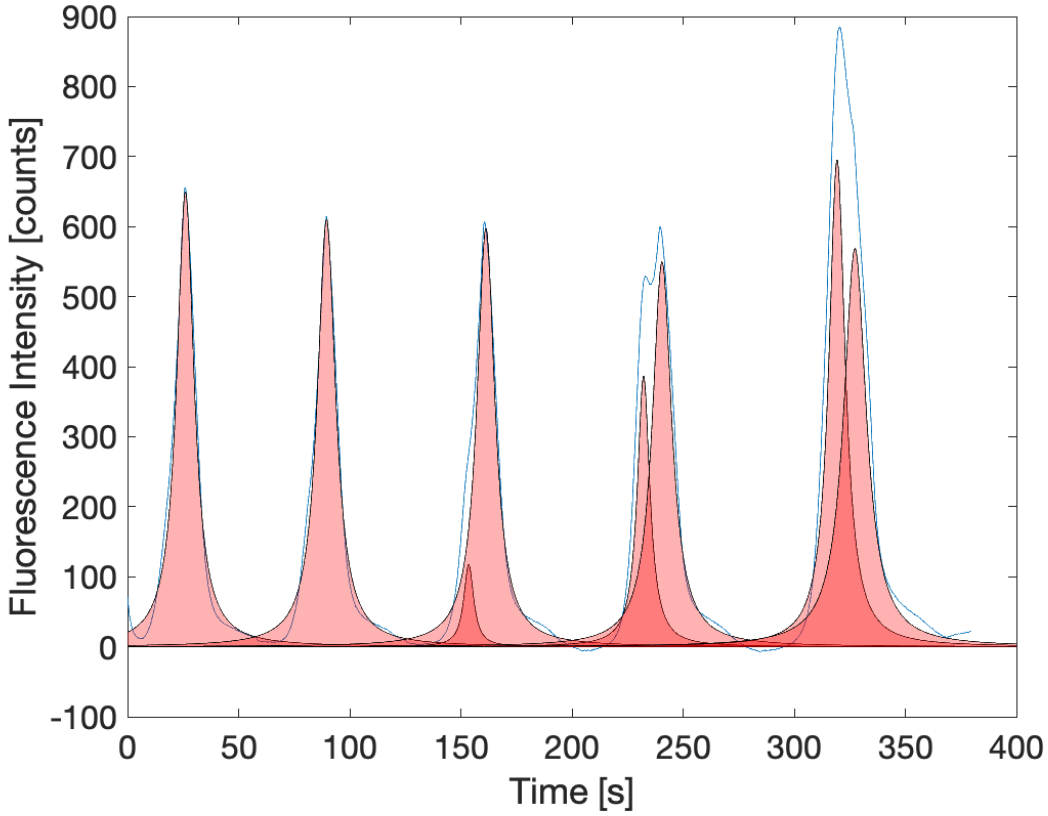

Figure 5.10.: Fluorescence intensity as a function of the applied potential. The upper limit of each CV was increased by 100 mV, starting at 600 mV. Lorentzian fits show the evolution of a second peak with a onset at a higher potential than the CV turning point, starting at 110 mV for peak 3 increasing to 140 mV for peak 5.

mV) a second fluorescence peak evolves that first appears as a small shoulder on the left side of peak 3, increasing in intensity in cycle 4 and becoming the dominant signal in cycle 5 which has an upper potential limit of 1000 mV. The fluorescence peak potentials are -80 mV (the lower turning point of the CV) in the first two cycles. The last three cycles show one peak at potentials of -75 and -60 mV, respectively and a second peak at a potential of 110 mV for peak 3, increasing to 140 mV for peak 5. The fluorescence onset potential of the respective scans slowly increases from 154 mV to 174 mV going from cycle 1 to cycle 3. The fluorescence onset potential of cycle 4 is dramatically more positive at 306 mV compared to the onset potentials between 154 to 174 mV in cycles 1-3, increasing to 345 mV in cycle 5.

We also ran the experiment with constant potential limits in consecutive CV scans with a waiting time of 2 minutes in between the scans. The resulting onset potentials and slopes of the fluorescence signal are listed in table 5.2.

Table 5.2.: On-/offset potentials and slopes of one sample after consecutive CVs with 2 minutes waiting time in between each CV.

On-/offset potentials and fluorescence slopes			
Delay time	Onset [mV]	Onset slope [counts/mV]	Maximum slope [counts/mV]
0	287	0.1	0.2
2	210	0.1	0.2
4	220	0.1	0.2
6	243	0.1	0.2
8	251	0.2	0.3

We test the behavior of the fluorescence response of the system at constant potential in the fluorescence 'on' region to test the stability of the fluorescence in the 'on' state. We scan the potential, starting at 600 mV in the fluorescence 'off' potential region, to -80 and to 58 mV, respectively, and hold the potential constant for 60 s while continuously recording fluorescence images. The two resulting fluorescence-time curves are shown in figure 5.11.

The fluorescence signal remains constant while applying a constant potential, only small deviations 70 and 20 counts, respectively can be observed, that are within the error of the experiment of approximately up to 5%, based on measured fluctuations of the fluorescence signal at steady potential in the potential step experiments, that is result of fluctuations of the number of fluorophores in the probed volume and artificial light from computer monitors. Subsequently decreasing the potential further leads to a further increase of the fluorescence signal. Ramping the potential to more positive values leads to a decrease of the fluorescence signal to the starting value, showing reversibility of the fluorescence response.

All experiments shown in the previous sections are carried out at potentials at which no electrode reaction (besides the unavoidable ORR) occur on the WE. In the following, we decrease the applied potential further to reach sufficient overpotential for the HER to run in bulk alkaline media and study the fluorescence response of the system. Figure 5.12 shows the fluorescence intensity as function of the applied potential for 8 cycles. The lower potential limit of the first 4 cycles was set to 0 mV, decreased to -500 mV in cycles 5 and 6 and further decreased to -700 mV in the last two cycles to reach high overpotential for HER.

All previous experiments show a maximum fluorescence in the lower CV turning point, which is also the case for the first 4 cycles shown in figure 5.12, that have a lower potential limit of 0 mV, i.e. before reaching sufficient overpotential for HER, which is -approximately -400 mV vs RHE.[GK21] However, as soon as the potential is low enough to allow HER, the fluorescence signal shows a peak, that is not located in the lower potential turning point. Decreasing the potential even further, i.e. increasing the HER rate, leads to a drop of the fluorescence signal to nearly zero at the lowest potential.

The first 4 cycles show a fluorescence onset potential of 339 $\pm$ 22 mV with a maximum

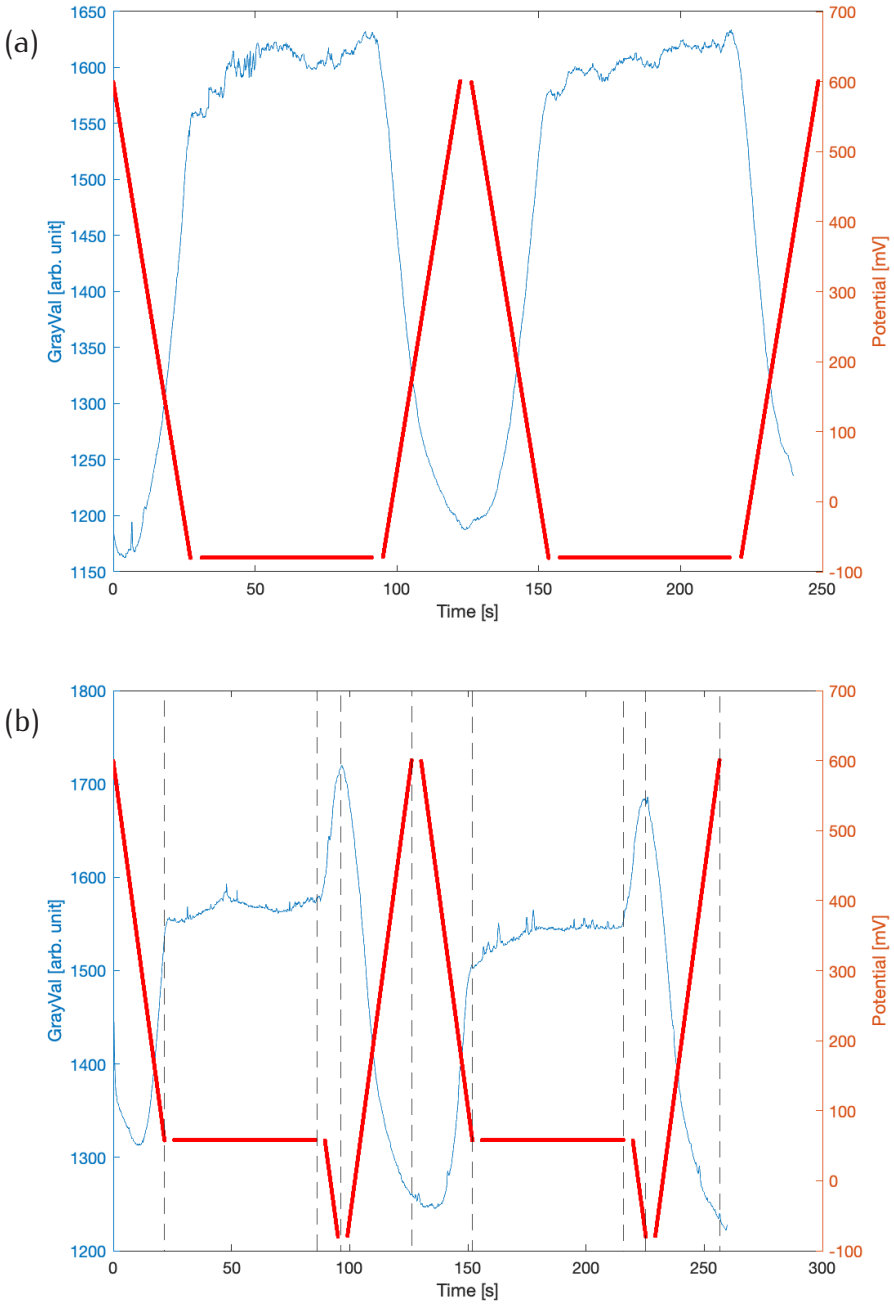

Figure 5.11.: (a) Potential held constant for 60 s after reaching the lower CV turning potential of -80 mV. (b) Potential held constant for 60 s at 56 mV after scanning down from 400 mV. After the potential was held, it is scanned further down to -80 mV. The black curve shows the fluorescence intensity, the red curve is the applied potential.

at 5 ± 4 mV. Cycles 5 and 6, with a lower potential limit of -500 mV, show fluorescence onset potentials of 295 ± 53 mV with a maximum at -308 ± 23 mV. After reaching the maximum, the fluorescence drops. The onset potential of the fluorescence drop is -386 ± 27 mV. The HER onset potential was derived from the CV at -388 mV and correlates well with the onset of the fluorescence drop. At an even higher overpotential for HER

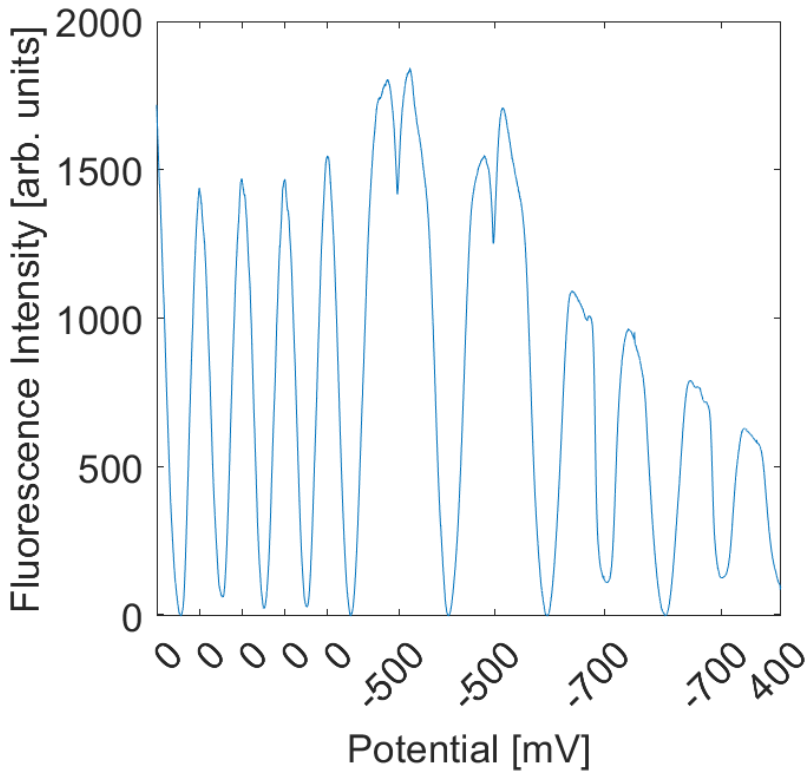

Figure 5.12.: Fluorescence intensity as function of the applied potential during 8 potential cycles. The lower turning potential was decreased from 0 to -500 to -700 mV after 4 and 6 cycles, respectively.

of -700 mV in cycles 7 and 8, the fluorescence onset potential is 294 ± 53 mV. The fluorescence reaches a plateau at -300 mV. The onset of the fluorescence drop is at -417 ± 73 mV, whereas the HER onset is at -410 mV.

To obtain insights into the rate at which the fluorescence response reacts to changes in the applied potential we run measurements with fast changes between fluorescence 'off' and 'on' potentials, i.e. switching between 400 and 0 mV with frequencies of 1, 2 and 10 Hz (Figure 5.13 1 Hz (yellow), 2 Hz (red), 10 Hz (blue)). It can be seen that the intensity of the fluorescence decreases with increasing switching frequency. The fluorescence maxima correlate well with the lower potential of 0 mV, corresponding to the fluorescence 'on' state.

5.4 Reference measurements and proof of concept

Figure 5.4 shows the fluorescence signal as function of the bulk pH. It can be seen, that the fluorophor is sensitive to pH changes and is only fluorescent in acidic to weak alkaline (pH = 8) media. This behavior of the fluorophor is used to probe the presence of protons at the interface between metal electrode and electrolyte in alkaline media upon potential changes. The appearance of a fluorescence signal means the presence

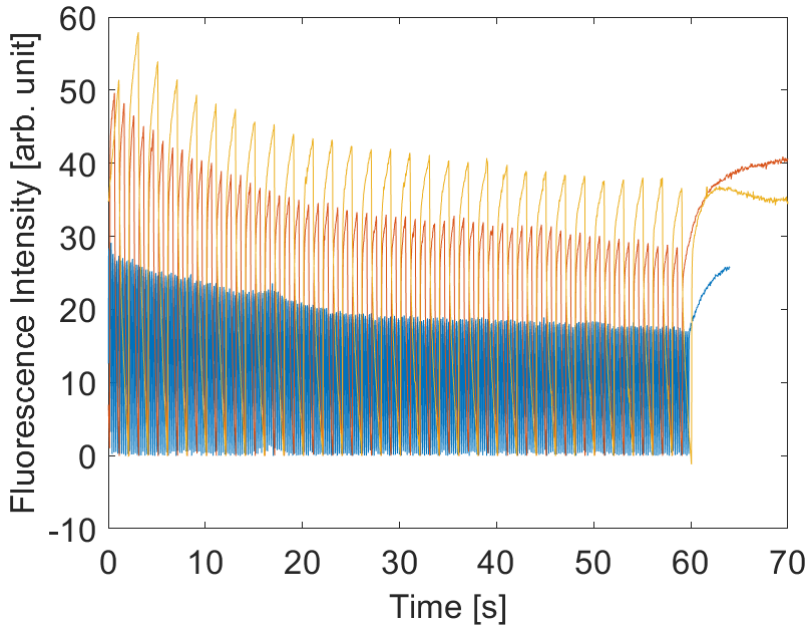

Figure 5.13.: Fluorescence intensity as a function of the potential switching frequency. The potential is switched with a frequency of 1 Hz (yellow), 2 Hz (red) and 10 Hz (blue) between 400 mV and 0 mV to switch between fluorescence 'off' and 'on' states.

of free protons in the double layer region that are able to protonate the fluorophor and trigger the switching of the fluorescence state from off to on.
To proof the concept of detection of free protons in alkaline media in the EDL region, we run sets of reference measurements to exclude other mechanism that lead to the detection of a fluorescence signal than the protonation of the dye.
The experiment without dye, shown in figure 5.5 (▲), demonstrates the lack of fluorescence signal in the cell under potential control without dye. This result supports the conclusion that the mesured light is the fluorescence light emitted by the fluorophor in its protonated state, as no extraordinary optical transmission as result of the interaction between incident laser light and the surface plasmon resonance of the gold film on the electrode induces a signal that could falsely be interpreted as fluorescence upon dye protonation. The extraordinary optical transmission by changes of the optical properties of the LSP induced by changes in the applied potential was subject to many studies[Par+20; Ven10], however, in our study, the effect does not seem to play a role in the origin of the fluorescence signal and the interpretation of the data, as shown by the blank signal of the sample without fluorophor. An influence of the extraordinary optical transmission of light would also be visible without dye. Instead, the results of the experiment with dye (●) show a clear, potential dependent change of the fluorescence state.
The measurements were done at potentials between 800 and -100 mV at which no reaction takes place at the electrode besides from ORR that cannot be avoided due to experimental limitations. In any case, all relevant reduction reactions, like ORR and HER, are hydrogen consuming processes. If there was any influence on the protonation

of the fluorophor by (unwanted) reactions happening in the EDL, the fluorescence would be lowered by the consumption of protons.
We also test the stability of the dye in the applied potential window between 0.6 and -0.2 V vs PdH in an electrochemical cell and cannot observe any dye related reaction (Figure 5.14). The CV, recorded in 0.1 M NaOH, shows a capacitive current of approximately 8 µA but no faradaic current flow at potentials above -0.1 V vs PdH. An electrochemical reaction related to the fluorophor would result in the appearance of a faradaic current flow.

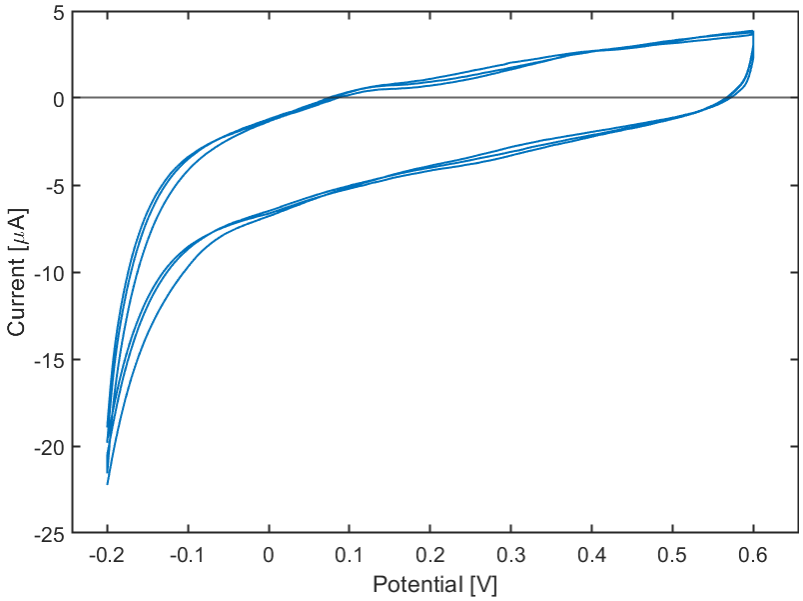

Figure 5.14.: CV recorded in an electrochemical glass cell in 0.1 M NaOH on a 10 nm thick Au on glass WE versus a PdH RE at a scan rate of 25 mV/s, i.e. the same conditions that are used in EC-FM experiments. The CV was recorded in the presence of oxygen to mimic the EC-FM conditions, where oxygen cannot be excluded from diffusing into the microscopy cell.

5.5 Fluorescence onset potentials and slopes

The on- and offset potentials are widely scattered, independently from experimental parameters like CV potential limits. Moreover, the evolution of a second fluorescence peak onset at higher potentials during a single experiment raises the question of the origin of the onset potential variation. The experiments differ in three main points: The constitution of the sample surface that is used. Because of the thin gold layer thickness, we dispense with flame-annealing to avoid damaging or the destruction of the sample and use it as rough Au(poly) electrode. This may cause deviations in the nature of the surface that may lead to differences in the electrochemical behavior. Moreover, differences in the upper potential limits can cause differences in the surface constitution by allowing for surface reconstruction if certain potentials are reached.

The third crucial parameter is the experimental time. With increasing time, the amount of oxygen that diffuses into the cell and into the EDL is higher compared to shorter experiments. On the other hand, cycling of the potential in the ORR region, i.e. at potentials lower than 400 mV, leads to a decrease of oxygen concentration because of the reduction of the oxygen in the electrolyte. These contrary mechanisms that either increase or decrease, respectively, the amount of oxygen in the cell complicate the interpretability of the fluorescence onset potentials and slopes and could be the reason for them being widely scattered. Figure 5.15a shows the fluorescence signal upon potential changes vs time (black) and the corresponding current response (red).

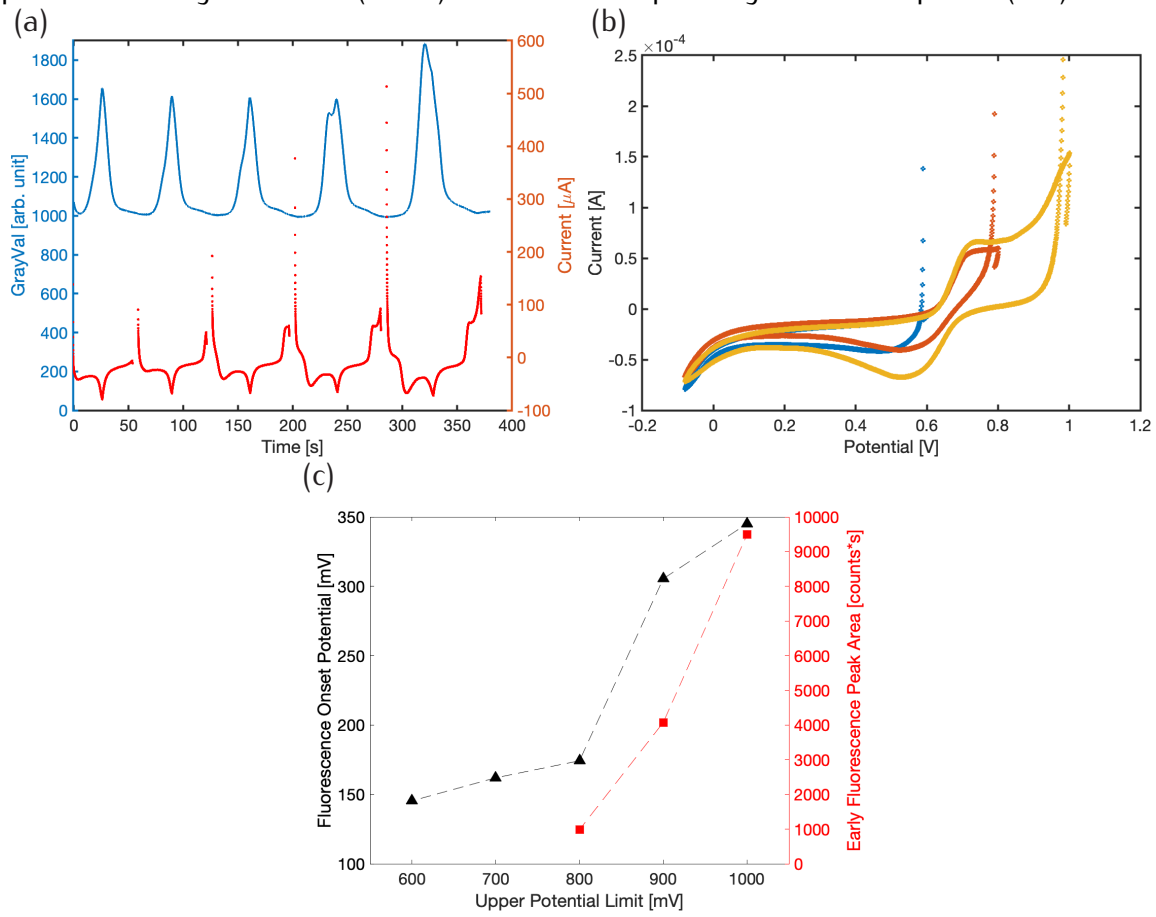

Figure 5.15.: (a) Fluorescence signal as function of changing potential plotted versus time (black) and the corresponding current recorded during the CV (red). (b) Conventionally plotted CV as current vs potential plot of the first, third and fifth cycle. (c) Evolution of the onset potentials and fluorescence peak areas. The potential was scanned with 25 mV/s in 0.1 M NaOH on a 10 nm thick Au WE on a glass slide.

The data shows the evolution of the early onset fluorescence peak, with an onset potential shifted towards the pzc of the WE (approx. 700 mV[**PARI1998**]), whereas the peak in the lower turning point of the potential cycle remains constant. At potentials negative of the pzc the electrode exhibit a negative surface charge, that would support an accumulation of protons at the electrode surface and therefore increase the measured fluorescence signal.

It can be noted that the current responses also changes significantly during the potential

cycles. A broad reductive current appears between 0.4 and 0.6 V in the regime of ORR in alkaline electrolyte.[DGB67] The increasing upper potential limit drives the system into specific adsorption of OH^- on the gold surfaces that can be seen as current flow in the anodic sweep at 0.7 to 0.8 V in figure 5.15.[Ham+90] The adsorption of OH^- causes the lifting of the reconstruction and significant higher current density of ORR.[Ham+90; SHA93] It seems that the lifting of surface reconstruction plays a role in the onset of the fluorescence. From a theoretical point of view, the onset of fluorescence should correlate with the availability of protons at the surface. That means, if less ORR happens during the cathodic sweep, that consumes protons, more protons would be available for protonation of the dye at potentials between 0.4 and 0.6 V, i.e. the potential window of ORR., which would result in a shift of the fluorescence onset towards higher potentials. As can be seen from the CVs, the ORR charge density increases with increasing upper limit, which would result in less available protons that can be sensed with the fluorophor. Nonetheless, the data show the evolution of the peak with an onset potential higher than the peak located in the potential turning point despite the rising ORR charge. Besides of the increasing ORR charge, the surface reconstruction, mediated through the adsorption of OH^-, happens at the high upper potential limit, which supports the assumption that the condition of the sample surface plays a crucial role in the fluorescence onset. However, the slope of the fluorescence increase is not affected by these considerations as it does not follow the widely scattered onset potentials but remains at values around 0.4 counts/mV.
Figure 5.16 shows the fluorescence onset • and offset ▶ potentials of different experiments, denoted with different colors, as a function of the ORR charge during the potential cycle.

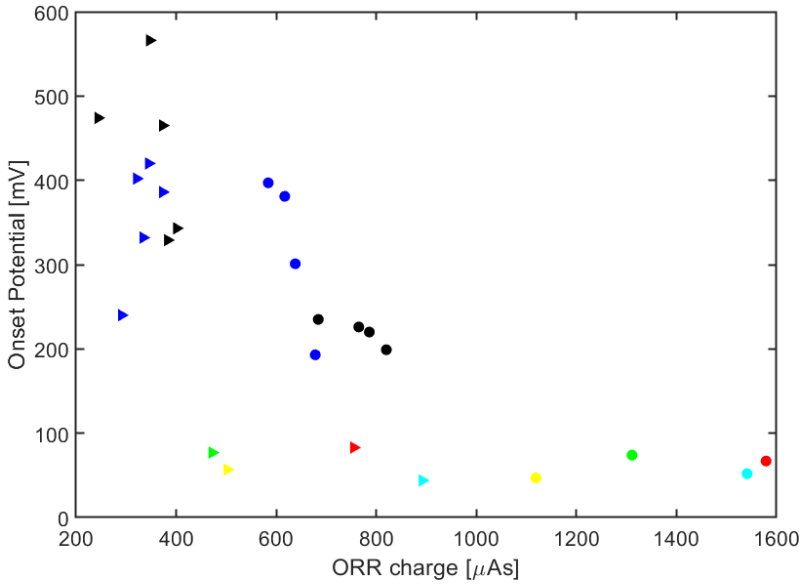

Figure 5.16.: Fluorescence peak on-/offset potentials as function of the ORR charge density. •: Onset potentials, ▶: Offset potentials, Different colors denote different experiments.

Figure 5.16 clearly shows a strong correlation between the sample (same color) and

the onset and offset potentials, indicated by a grouping of points of the same color. The ORR charge on the other hand does not seem to correlate with the onset potential, and therefore we cannot conclude that the amount of oxygen plays a role in the onset potential of the fluorescence. However, the related onset potentials of multiple potential cycles on one sample strongly indicate the influence of the the surface condition on the fluorescence onset potential. Experiments with strict exclusion of oxygen could bring more clarity in the interpretation of the onset potentials in the future. A total suppression of the ORR could show if the scattering of the onset potentials of the fluorescence is result of the surface condition of the electrode.

5.6 Fluorescence in non-equilibrium conditions

All experiments discussed before show a maximum fluorescence in the lower CV turning point, meaning that with decreasing potential, more free protons were generated to protonate and, therefore, 'activate' more fluorophores, leading to an increase in fluorescence. The experiments with the lower potential limits of -500 and -700 mV provide sufficient overpotential for HER off-equilibrium and show a fluorescence upper limit prior to the fluorescence drop at the onset of HER. Figure 5.17a shows two potential cycles with a lower potential limit of -500 mV. The fluorescence signal (blue) increase slowed down before dropping at the onset of HER. The corresponding current (red) also shows a short plateau at -100 µA prior to the onset of HER.

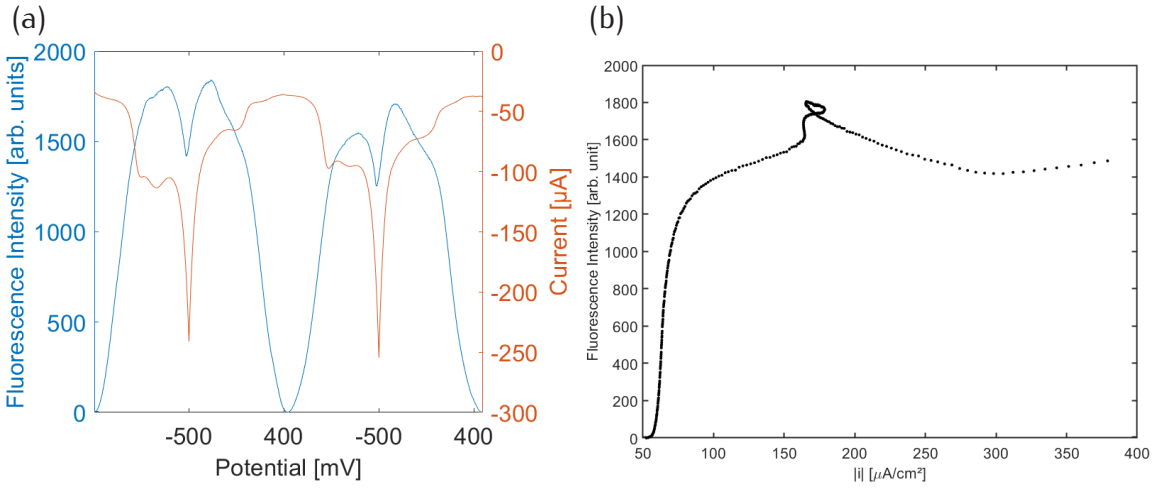

Figure 5.17.: (a) Fluorescence signal over 2 potential cycles (blue) between 400 and -500 mV. The corresponding current is shown in red. (b) Fluorescence intensity as a function of the absolute current density.

The correlation between fluorescence signal and current density is shown in figure 5.17b. Starting at the fluorescence onset potential of 295±53 mV, the fluorescence signal increases from 0 to 1420 counts at -90 mV independently of the current density (-42 to -50 µA). At -90 mV the current drops from -50 µA, i.e. the capacitive current,

to -103 µA, indicating that a cathodic reaction is starting. At the same potential, the fluorescence intensity increase levels off. The results show that at a potential of -90 mV, either the lower pH sensitivity limit of the dye is reached, i.e. all available dye molecules in the probing volume are protonated and fluoresce, or that the cathodic reaction that leads to the current increase from -50 to -103 µA consumes protons and inhibits a further fluorescence increase. The first explanation seems to be more likely, as the fluorescence signal levels off and does not decrease. A cathodic reaction that leads to a level off of the fluorescence signal would need to consume exactly the amount of protons needed to hold the fluorescence at a constant level to lead to the observed result, which is not likely the case. Experimentally a change of the dye with different pH dependence could help to prove this point and gain more information about the correlation between changes of the proton concentration through faradaic reactions and the recorded fluorescence signal.
The further decrease of the potential from the onset of HER at -388 mV to -500 mV leads to a drop of fluorescence, starting at -386 mV. The fluorescence drop is well correlated with the HER onset with a difference of 2 mV. As the HER starts to consume protons, fewer protons are available for the protonation of the dye. The rate of HER is fast enough to consume protons faster than the rate of protonation of fluorophores, leading to a decrease in the observed fluorescence intensity. The fluorescence response (blue) and current (red) of the further decrease of the lower potential limit to -700 mV are shown in figure 5.18a, the correlation between fluorescence and absolute current density is shown in 5.18b. Increasing the overpotential of HER even more by lowering the applied potential to -700 mV leads to a nearly total loss of fluorescence. By increasing the overpotential, the HER becomes faster and the consumption of protons causes the vanishing of the fluorescence signal.

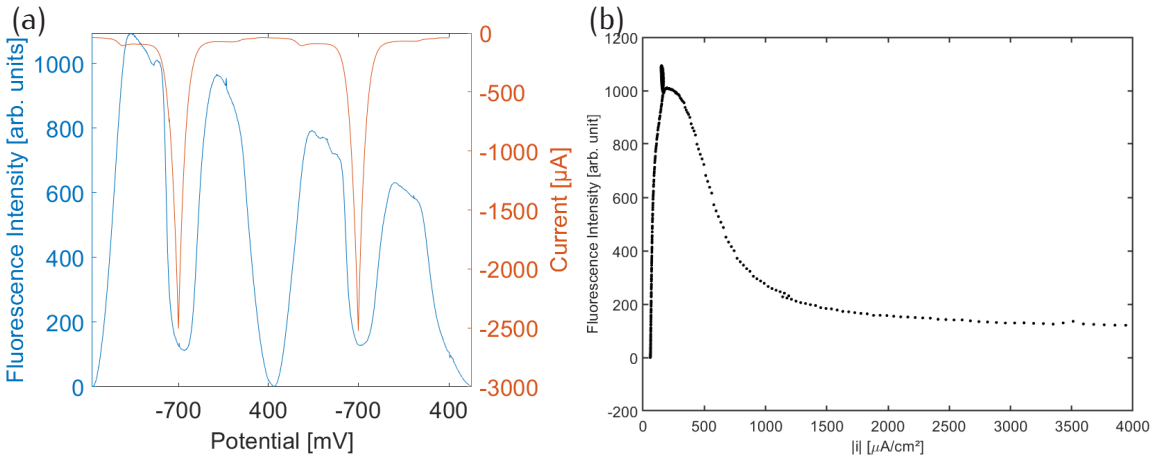

Figure 5.18.: (a) Fluorescence signal over 2 potential cycles (blue) as function of the applied potential between 400 and -700 mV. The corresponding current is shown in red. (b) Correlation between fluorescence intensity and absolute current density.

The onset of HER at -410 mV is followed by a rapid drop of the fluorescence that starts at -417 mV. Figure 5.18b shows a critical absolute current density for HER of 845 $\mu A/cm^2$. Overcoming this critical current leads to the rapid decrease of fluorescence.

The associated critical proton consumption rate at 845 $\mu A/cm^2$ is 3.8 protons per surface atom per second, means that 3.8 protons per surface atom per second are 'consumed' by the HER. The proton consumption rate is calculated from the charge density under the assumption that one electron is transferred per proton and with a surface atom density of Au(111) of $1.388 \cdot 10^{15}$ atoms/cm^2. At faster rates, the dye protonation seems not fast enough to maintain the fluorescence level and the local proton concentration sensed by the fluorophor drops. The delivery of protons by the water dissociation reaction, as the only source of protons in the bulk alkaline media, becomes the rate limiting process at high HER overpotentials.

5.7 Towards local surface pH measurements

The overall aim of this project is the direct measurement of the surface pH of a metal electrode under electrochemical conditions. Therefore we need to correlate the measured fluorescence signal, that is sensitive to the surface concentrations of protons, with a local pH. To calibrate the surface fluorescence signal, we compare the EC-FM signal with data obtained from bulk fluorescence spectroscopy experiments in solutions of different pH.
From the bulk experiments, we obtain a curve of values that follows a sigmoidal, just as expected for a titration experiment of a weak acid versus a strong base.[KP22] The obtained data from the surface fluorescence experiments can also be fitted following a sigmoidal curve. The bulk (●) and one example set of surface (●) fluorescence data and their respective sigmoidal fits as functions of the bulk pH and applied potential, respectively, are shown in figure 5.19.

The data show that the fluorophor can be used for pH detection in a window between 4 and 8.4 pH units. Below or above these values, the sigmoidal reaches a plateau and a change in pH does not lead to a change in fluorescence. Additionally, the surface fluorescence curve does not perfectly follow the fit function in the pH range between 7.6 and 8.4, i.e. around the fluorescence onset in some cases when the fluctuation of the measured signal without fluorescence, i.e. the background signal, is larger than the fluorescence change of the dye in the pH range between 7.6 and 8.4, which makes the correlation in this range unreliable.
For the correlation of pH and applied potential, we compare the fluorescence intensity with the bulk spectroscopy data normalized to 1 at maximum fluorescence in the bulk experiments. For each datapoint of the EC-FM dataset and the directly related potential at which it was recorded, we read the pH value of the datapoint of the fit of the bulk spectroscopic data that has the same normalized fluorescence intensity value. An example of the resulting plot is shown in figure 5.20a for one dataset.

It can be seen that at potentials above the onset potential of fluorescence, the correlation gives arbitrary values that are above the upper pH sensing limit of the

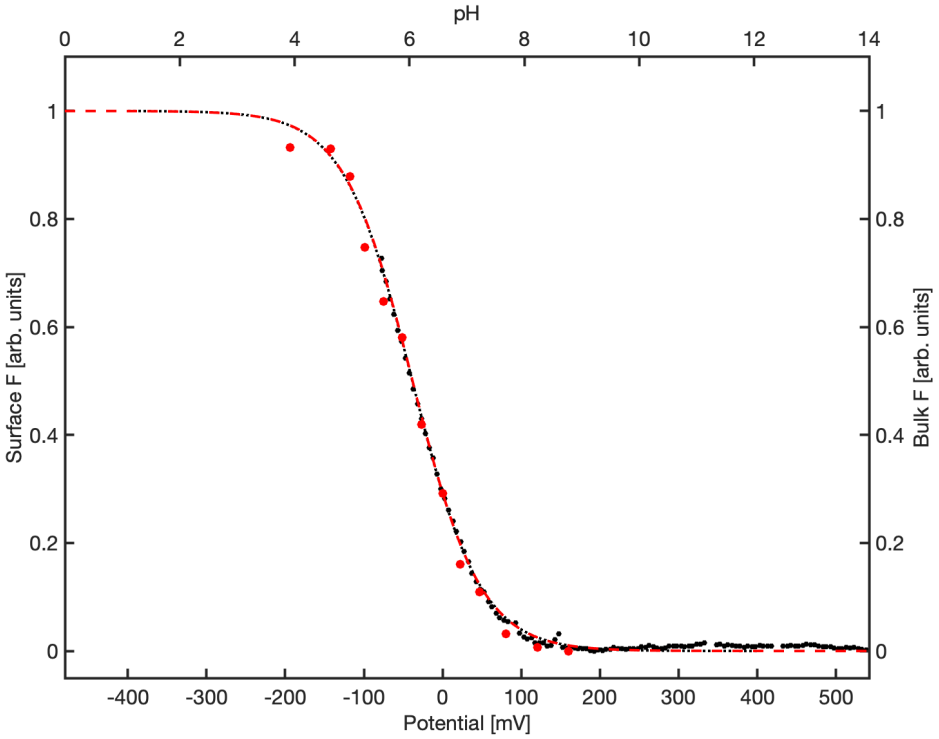

Figure 5.19.: Bulk fluorescence spectroscopy (●) data fitted with a sigmoidal fit as function of the pH of the bulk solution. Fluorescence data obtained from surface microscopy experiments ● as function of the applied potential of the WE.

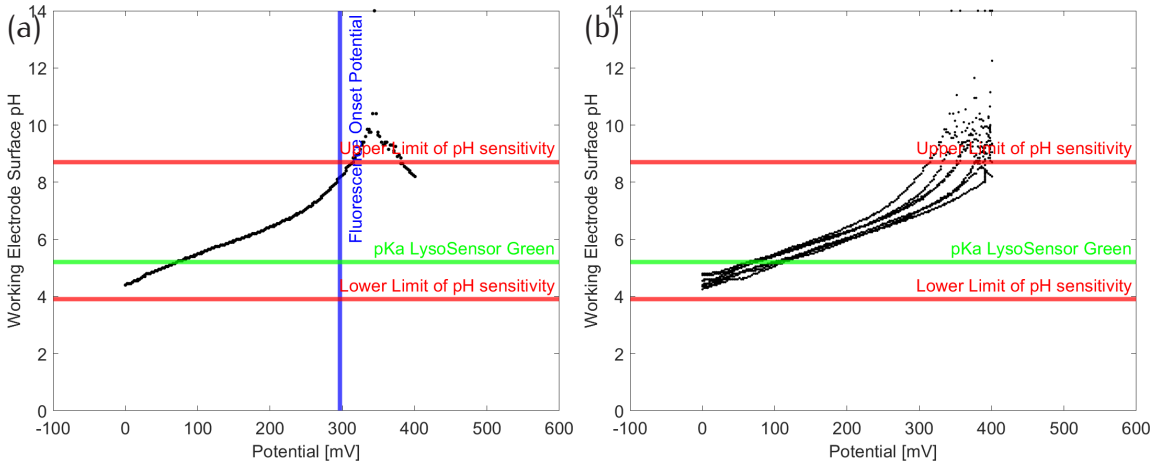

Figure 5.20.: (a) Working electrode surface pH as function of the applied electrode potential of an individual sample. (b) Comparison of the pH-potential correlation of multiple cycles of one sample.

fluorophor. These arbitrary values are result from experimental data that do not follow the sigmoidal fitfunction close to the fluorescence onset because the error is larger than the measured signal in this range. However, the fluorescence intensities measured at potentials below the onset potential are reliable as they are within the limit of the sensitivity of the fluorophor. The correlation shows a decrease in the surface pH of

the WE after the onset of the fluorescence, in the experiment shown in figure 5.20 at potentials lower than 300 mV. The slope of the pH decrease is 8.8 pH units per V until the experimental potential minimum of -80 mV is reached. That means that the effective proton concentration at the electrode surface increases with decreasing potential and leads to protonation of the dye, whose fluorescence signal is measured as increasing value. This happens despite the strong alkaline pH of the bulk solution and supports Frumkin assumption of the accumulation of protons in the EDL with decreasing potentials negative of the pzc. Figure 5.20b shows the correlation result of four consecutive measurements on one sample. It can be seen, that the final pH at the lower potential limit is within a range of 0.5 pH units between 4.2 and 4.7, which is close to the lower limit of the pH sensitivity. Slight variations of the final pH could be the result of fluctuations of the dye concentration in the probing volume or result of aggregation of the dye molecules, that would lead to a decrease in the sensed pH. Moreover, changes in the surface condition throughout the experiment could not only lead to a shift of the onset potential as described in the previous section, but also could influence the surface pH by changes in the water splitting rate, for example through the formation of defect sites. However, the slope of the pH decrease with potential is always the same in one sample (here: 8.8 pH units per V) and seems to depend on the onset of fluorescence of the sample. The pH value at 0 V is, independent of the sample, between 4.2 and 5. A large variation of the fluorescence onset potential between 51 and 281 mV therefore requires a change in the slope of the pH change to end in the same pH region.

Figures 5.21a and b show the pH-potential correlation of one dataset together with the measured fluorescence signal (a) and the current during the experiment (b) to directly compare the current flow during the experiment with the fluorescence signal.

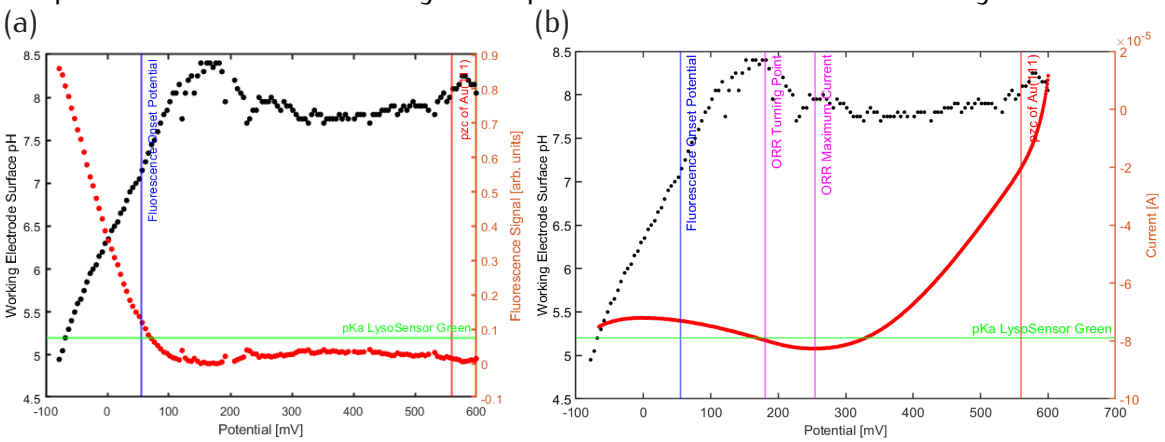

Figure 5.21.: (a) Local surface pH as function of the applied potential (black) as measured by the fluorescence signal of the dye (red). (b) Local surface pH as function of the applied potential (black) and measured current during the experiment (red).

Figure 5.21a shows that small deviations in the fluorescence signal at high potentials, that are within the experimental error (due to light fluctuations of the environment from monitors, etc.), strongly influence the extracted pH value.

The current curve shown in figure 5.21b correlates with the change in pH. In the

maximum of the current at 255 mV, related to the ORR, the pH value is at the upper sensing limit, where no fluorescence signal is detected. At the turning point of the ORR related current at 180 mV, the pH begins to decrease and reaches the experimentally determined fluorescence onset at 300 mV. The experimentally determined onset of fluorescence is at potentials below the onset of the pH decrease.
The potential-pH correlation plot for a lower limit of -700 mV is shown in figure 5.22. The experiments at high HER overpotentials show an increase of the surface pH at potentials lower than the HER onset. This pH increase after starting the HER means that the effective proton concentration at the electrode is lowered by the HER. This is in line with the expectations as the HER is a proton consuming reaction. At a rate at which the water splitting reaction becomes the rate limiting step to provide protons for the HER, which is experimentally determined to be 3.8 protons/s per surface atom, the effective proton concentration, i.e. the concentration of protons that is sensed by the fluorophor and not directly converted into molecular hydrogen, decreases and is sensed by a decrease of the fluorescence signal.

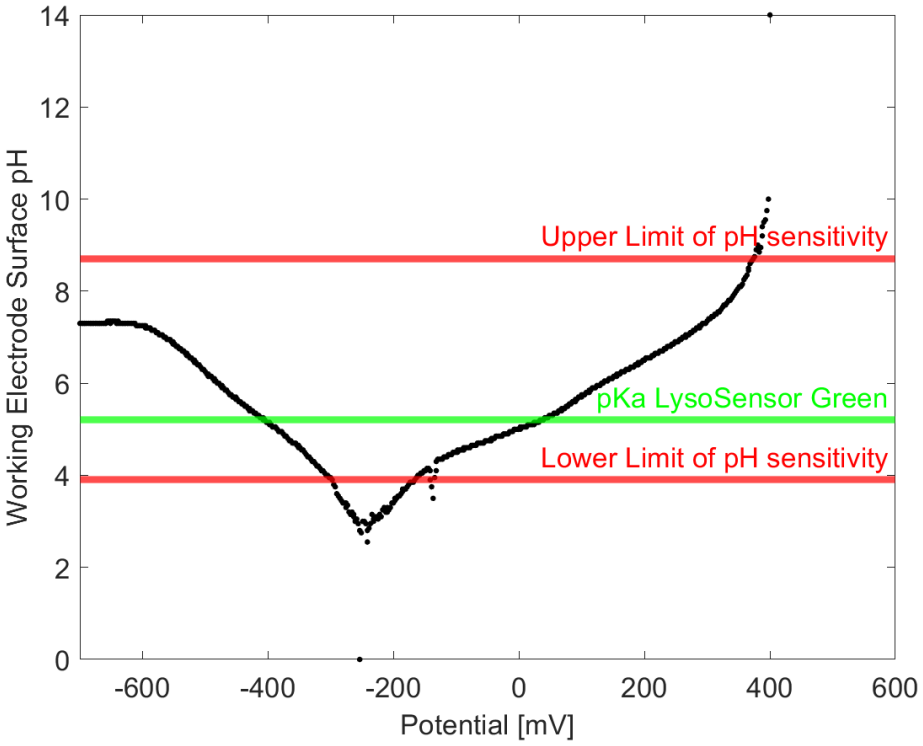

Figure 5.22.: Potential-pH correlation plot of an experiment with a lower potential limit of -700 mV.

It can be seen that the pH decreases until a potential of -250 mV is reached. However, in the potential region between -180 and -280 mV, we are out of the pH range of our sensor, so that we can not rely on the data. At potentials lower than this value, the pH increases due to the onset of HER and the ongoing proton consumption.

5.8 Summary and outlook

In this chapter we have shown an experimental way to directly measure the effective surface proton concentration on an electrified metal electrode by the use of a pH sensitive dye and highly sensitive fluorescence microscopy. We showed the proof of concept that the dye shows bright fluorescence at high proton concentrations at the surface despite the use of pH 13 bulk alkaline electrolyte. Moreover, we showed that the measured fluorescence is result of the protonation of the dye and is not influenced by any extraordinary optical transmission as result of the interactions of the incident light with localized surface plasmons on the metal electrode. We showed, that a fluorescence signal only occurs in the bulk alkaline solution when a potential is applied under electrochemical control.
The fluorescence signal shows an increase with decreasing potential until the potential turning point is reached as long as the overpotential is too small for the HER. We could show experimentally that the fluorescence level remained constant within the experimental error when the potential was held constant in the fluorescence 'on' state, showing the stability of the system under study. A subsequent decrease of potential led to a further increase of the fluorescence signal. The fluorescence onset potential was found to be widely scattered throughout the experiments on samples under the same experimental conditions. We conclude that the onset potential of the fluorescence is dependent on the state of the metal surface. Moreover, we found that a change in the upper potential limit of the CV leads to the loss of the reconstructed surface structure due to the specific adsorption of anions such as OH^-. The lifting of the reconstruction changes the surface state and thus, in our interpretation, can cause a change in the onset potential of the fluorescence.
The onset of the HER effectively reduces the effective surface pH and with that the effective proton concentration that is sensed by the fluorophor. We found a critical proton consumption rate that leads to the collapse of the acidic environment of the electrode surface. We conclude that the acidic surface condition can only be upheld when the rate of water splitting is higher than the rate of any proton consuming reaction, to deliver enough protons to maintain a lower effective surface pH than the bulk pH.

In further experiments, oxygen needs to be excluded from the experiment to exclude one of the variables that might influence the fluorescence onset potentials and slopes. If we only vary the surface condition between the experiments we could gain insight how this effects the surface proton concentration. With the design of a proper EC microscopy cell we could achieve this and gain further insights into this method.
Another approach is the use of different dyes that are responsive to different pH ranges to complete the picture of local surface acidity in alkaline media. Even a mixture of different dyes in one cell could be an approach to record data aver the whole pH scale.

The targeted triggering of electrochemical reactions during the experiment, i.e. measure out of equilibrium, may also be an interesting approach to investigate the robustness of the presented method against faradaic reactions on the electrode.
We could demonstrate that the EC-FM method is a promising approach to measure the surface pH on electrodes that helps to improve the development and outcome of electrochemical applications.

Bibliography

[23] Jan. 2023. URL: https://bip.cnrs.fr/groups/bip08/methods/.

[80] *CRC Handbook of Chemistry and Physics*. CRC Press, 1980.

[ACH90] H. Angerstein-Kozlowska, B. E. Conway, and A. Hamelin. "Electrocatalytic mediation of oxidation of H2 at gold by chemisorbed states of anions". In: *Journal of Electroanalytical Chemistry and Interfacial Electrochemistry* 277.1 (1990), pp. 233–252. DOI: https://doi.org/10.1016/0022-0728(90)85105-E. URL: https://www.sciencedirect.com/science/article/pii/002207289085105E.

[AH12] Javier Aizpurua and Rainer Hillenbrand. "Localized Surface Plasmons: Basics and Applications in Field-Enhanced Spectroscopy". In: ed. by Stefan Enoch and Nicolas Bonod. Springer Berlin Heidelberg, 2012.

[AHK17] Areeg Abdelrahman, Johannes M. Hermann, and Ludwig A. Kibler. "Electrocatalytic Oxidation of Formate and Formic Acid on Platinum and Gold: Study of pH Dependence with Phosphate Buffers". In: *Electrocatalysis* 8.6 (2017), pp. 509–517.

[And00] M. S. Anderson. "Locally enhanced Raman spectroscopy with an atomic force microscope". In: *Applied Physics Letters* 76 (2000), p. 3130.

[Ant60] L. Antropov. "Kinetics of Electrode Processes and Null Point of Metals". In: *Connc. Sci. Ind. Res.* (1960).

[ASD79] R. Adzic, M. Spasojevic, and A. Despic. In: *Electrochimica Acta* 24 (1979), p. 577.

[Bag90] P. S. Bagus. "Theoretical analysis of the vibrational shifts of CO chemisorbed on Pd(001)". In: *Surface Science* 236 (1990), pp. 233–240.

[Ban+14] Aliaksandr S Bandarenka et al. "Techniques and methodologies in modern electrocatalysis: evaluation of activity, selectivity and stability of catalytic materials". In: *Analyst* 139.6 (2014), pp. 1274–1291.

[Bay+10] D Bayer et al. "Electrochemical oxidation of C2 alcohols at platinum electrodes in acidic and alkaline environment". In: *International Journal of Hydrogen Energy* 35.22 (2010), pp. 12660–12667.

[BB08] Mukesh Bhardwaj and R. Balasubramaniam. "Uncoupled non-linear equations method for determining kinetic parameters in case of hydrogen evolution reaction following Volmer–Heyrovsky–Tafel mechanism and Volmer–Heyrovsky mechanism". In: *International Journal of Hydrogen Energy* 33.9 (2008), pp. 2178–2188. DOI: https://doi.org/10.1016/j.ijhydene.2008.02.027. URL: https://www.sciencedirect.com/science/article/pii/S0360319908001924.

[BBL83] B. Beden, A. Bewick, and C. Lamy. "A comparative study of formic acid adsorption on a platinum electrode by both electrochemical and emirs techniques". In: *Journal of Electroanalytical Chemistry and Interfacial Electrochemistry* 150 (1983), pp. 505–511.

[Ben+96] A. Bensalem et al. "Spectroscopic Study of CO adsorp- tion on palladium-ceria catalyst". In: *Journal of the Chemical Society* 92 (1996), pp. 3233–3237.

[Ber12] Isadore Berlman. *Handbook of florescence spectra of aromatic molecules*. Elsevier, 2012.

[BF01] A. J. Bard and L. R. Faulkner. *Electrochemical methods: Fundamentals and applications*. Vol. 2. John Wiley & Sons New York, 2001.

[BH78] A. M. Bradshaw and F. M. Hoffmann. "The Chemisorption of Carbon Monoxide on Palladium Single Crystal Surfaces: IR Spectroscopic Evidence For Localised Site Adsorption". In: *Surface Science* 72 (1978), pp. 513–535.

[BHF17] Valentin Briega-Martos, Enrique Herrero, and Juan M. Feliu. "Effect of pH and Water Structure on the Oxygen Reduction Reaction on platinum electrodes". In: *Electrochimica Acta* 241 (2017), pp. 497–509. ISSN: 0013-4686. DOI: https://doi.org/10.1016/j.electacta.2017.04.162. URL: https://www.sciencedirect.com/science/article/pii/S0013468617309568.

[Bjö+11] Mårten E. Björketun et al. "Hydrogen evolution on Au(111) covered with submonolayers of Pd". In: *Physical Review B* 84.4 (July 2011), pp. 045407–. DOI: 10.1103/PhysRevB.84.045407. URL: https://link.aps.org/doi/10.1103/PhysRevB.84.045407.

[BK32] John Alfred Valentine Butler and James Pickering Kendall. "The thermodynamics of the surfaces of solutions". In: *Proceedings of the Royal Society of London. Series A, Containing Papers of a Mathematical and Physical Character* 135.827 (1932), pp. 348–375. DOI: 10.1098/rspa.1932.0040. URL: https://doi.org/10.1098/rspa.1932.0040.

[BK65] Richard Brandt and Albert S. Keston. "Synthesis of diacetyldichlorofluorescin: A stable reagent for fluorometric analysis". In: *Analytical Biochemistry* 11.1 (1965), pp. 6–9.

[BK96] M. Baldauf and D. M. Kolb. "Formic Acid Oxidation on Ultrathin Pd Films on Au(hkl) and Pt(hkl) electrodes". In: *Journal of Physical Chemistry* 100 (1996), pp. 11375–11381.

[BKI01] Klemen Bohinc, Veronika Kralj-Iglič, and Aleš Iglič. "Thickness of electrical double layer. Effect of ion size". In: *Electrochimica Acta* 46.19 (2001), pp. 3033–3040. ISSN: 0013-4686. DOI: https://doi.org/10.1016/S0013-4686(01)00525-4. URL: https://www.sciencedirect.com/science/article/pii/S0013468601005254.

[Boc47] J. O'M. Bockris. "Electrolytic polarisation—I. The overpotential of hydrogen on some less common metals at high current densities. Influence of current density and time". In: *Transactions of the Faraday Society* 43.0 (1947), pp. 417–429. DOI: 10.1039/TF9474300417. URL: http://dx.doi.org/10.1039/TF9474300417.

[BR18] Dmitri A. Bulushev and Julian R. H. Ross. "Towards Sustainable Production of Formic Acid". In: *ChemSusChem* 11.5 (2018), pp. 821–836. DOI: https://doi.org/10.1002/cssc.201702075. eprint: https://chemistry-europe.onlinelibrary.wiley.com/doi/pdf/10.1002/cssc.201702075. URL: https://chemistry-europe.onlinelibrary.wiley.com/doi/abs/10.1002/cssc.201702075.

[BR82] G. Binning and H. Rohrer. "Surface studies by scanning tunneling microscopy". In: *Physical Review Letters* 49 (1982).

[Bri+20] Valentin Briega-Martos et al. "Why the activity of the hydrogen oxidation reaction on platinum decreases as pH increases". In: *Electrochimica Acta* 354 (2020), p. 136620.

[BRM07] B.B. Blizanac, P.N. Ross, and N.M. Markovic. "Oxygen electroreduction on Ag(111): The pH effect". In: *Electrochimica Acta* 52.6 (2007), pp. 2264–2271.

[Bru+84] G. J. Brug et al. "The analysis of electrode impedances complicated by the presence of a constant phase element". In: *Journal of Electroanalytical Chemistry and Interfacial Electrochemistry* 176.1 (1984), pp. 275–295. DOI: https://doi.org/10.1016/S0022-0728(84)80324-1. URL: https://www.sciencedirect.com/science/article/pii/S0022072884803241.

[BSK05] G. L. Beltramo, T. E. Shubina, and M. T. M. Koper. "Oxidation of Formic Acid and Carbon Monoxide on Gold Electrodes Studied by Surface-Enhanced Raman Spectroscopy and DFT". In: *ChemPhysChem* 6.2597-2606 (2005).

[BWA01] S. R. Brankovic, J. X. Wang, and R. R. Adžić. "Metal monolayer deposition by replacement of metal adlayers on electrode surfaces". In: *Surface Science* 474.1 (2001), pp. L173–L179. DOI: https://doi.org/10.1016/S0039-6028(00)01103-1. URL: https://www.sciencedirect.com/science/article/pii/S0039602800011031.

[CB56] B. Conway and J. O'M. Bockris. In: *Naturwiss.* 43 (1956), p. 446.

[Che+22a] Wei Chen et al. "Challenges and recent progress in unraveling the intrinsic pH effect in electrocatalysis". In: *Current Opinion in Electrochemistry* 34 (2022), p. 101003. DOI: https://doi.org/10.1016/j.coelec.2022.101003. URL: https://www.sciencedirect.com/science/article/pii/S2451910322000680.

[Che+22b] X. Chen et al. "How Palladium inhibits CO poisoning during electrocatalytic formic acid oxidation and carbon dioxide reduction". In: *Nature Communications* 13 (2022).

[Chl+17] D. K. Chlebda et al. "Surface structure of cobald, palladium and mixed oxide-based catalysts and their activity in methane combustion studied by means of micro-Raman spectroscopy". In: *Journal of Raman spectroscopy* 48 (2017), pp. 1871–1880.

[CJ15] Yi Cheng and San Ping Jiang. "Advances in electrocatalysts for oxygen evolution reaction of water electrolysis-from metal oxides to carbon nanotubes". In: *Progress in Natural Science: Materials International* 25.6 (2015), pp. 545–553. DOI: https://doi.org/10.1016/j.pnsc.2015.11.008. URL: https://www.sciencedirect.com/science/article/pii/S1002007115001264.

[Col+16] V. Colic et al. "Influence of the electrolyte composition on the activity and selectivity of electrocatalytic centers". In: *Catalysis Today* 262.24 (2016).

[Com] Wikimedia Common. *Epifluorescence Widefield Microscope*. (Visited on 2023).

[CP73] A. Capon and R. Parson. "The oxidation of formic acid at noble metal electrodes: I. Review of previous work". In: *Journal of Electroanalytical Chemistry and Interfacial Electrochemistry* 44.1 (1973), pp. 1–7.

[CPS78] R. R. Chance, A. Prock, and R. Silbey. "Molecular Fluorescence and Energy Transfer Near Interfaces". In: *Advances in Chemical Physics*. John Wiley & Sons, Ltd, 1978, pp. 1–65. ISBN: 9780470142561. DOI: https://doi.org/10.1002/9780470142561.ch1. eprint: https://onlinelibrary.wiley.com/doi/pdf/10.1002/9780470142561.ch1. URL: https://onlinelibrary.wiley.com/doi/abs/10.1002/9780470142561.ch1.

[Cre11] Christoph Cremer. "Lichtmikroskopie unterhalb des Abbe-Limits. Lokalisationsmikroskopie". In: *Physik in unserer Zeit* 42.1 (2023/03/01 2011), pp. 21–29. DOI: https://doi.org/10.1002/piuz.201101251. URL: https://doi.org/10.1002/piuz.201101251.

[CT02] B. E. Conway and B. V. Tilak. "Interfacial processes involving electrocatalytic evolution and oxidation of H_2, and the role of chemisorbed H". In: *Electrochimica Acta* 47.22 (2002), pp. 3571–3594.

[Cue+12] A. Cuesta et al. "Mechanism of the Electrocatalytic Oxidation of Formic Acid on Metals". In: *ACS Catalysis* 2 (2012), pp. 728–738.

[Cue+13] A. Cuesta et al. "Electrooxidation of formic acid on gold: An ATR-SEIRAS study of the role of adsorbed formate". In: *Catalysis Today* 202 (2013), pp. 79–86.

[Dem+03] O. Demoulin et al. "Operando resonance Raman spectroscopic chracterisation of the oxidation state of palladium in Pd/µ-Al_2O_3 catalysts during the combustion of methane". In: *Physical Chemistry Chemical Physics* 5 (2003), pp. 4394–4401.

[Dey22] Tania Dey. "Microplastic pollutant detection by Surface Enhanced Raman Spectroscopy (SERS): a mini-review". In: *Nanotechnology for Environmental Engineering* (Feb. 2022). DOI: 10.1007/s41204-022-00223-7.

[DGB67] A. Damjanovic, M. A. Genshaw, and J. O'M. Bockris. In: *Journal of Electroanalytical and Interfacial Chemistry* 15 (1967), p. 17.

[DKS76] D. Dickertmann, F.D. Koppitz, and J.W. Schultze. "Eine methode zum ausschluss von randeffekten bei elektrochemischen messungen an einkristallen: Test anhand der adsorptionssysteme Ag/Pb2+ und Au/Cu2+". In: *Electrochimica Acta* 21.11 (1976), pp. 967–971. ISSN: 0013-4686. DOI: https://doi.org/10.1016/0013-4686(76)85072-4. URL: https://www.sciencedirect.com/science/article/pii/0013468676850724.

[Dom06] K. F. Domke. "Tip-enhanced Raman spectroscopy – Topographic and chemical information on the nanoscale". PhD thesis. Freie Universitaet Berlin, 2006.

[Don+18] Q. Dong et al. "Multifunctional Pd-Sn electrocatalysts enabled by in situ formed SnO_x and TiC triple junctions". In: *Nano Energy* 53 (2018), pp. 940–948.

[DP10] K. F. Domke and B. Pettinger. "Studying surface chemistry beyond the diffraction limit: 10 years of TERS". In: *ChemPhysChem* 11 (2010), p. 1365.

[DZP06] Katrin F. Domke, Dai Zhang, and Bruno Pettinger. "Toward Raman Fingerprints of Single Dye Molecules at Atomically Smooth Au(111)". In: *Journal of the American Chemical Society* 128.45 (Nov. 2006), pp. 14721–14727. DOI: 10.1021/ja065820b. URL: https://doi.org/10.1021/ja065820b.

[EC11] Daniel V. Esposito and Jingguang G. Chen. "Monolayer platinum supported on tungsten carbides as low-cost electrocatalysts: opportunities and limitations". In: *Energy & Environmental Science* 4.10 (2011), pp. 3900–3912. DOI: 10.1039/C1EE01851E. URL: http://dx.doi.org/10.1039/C1EE01851E.

[Eft17] A. Eftekhari. "Electrocatalysts for hydrogen evolution reaction". In: *International Journal of Hydrogen Energy* 42.16 (2017), pp. 11053–11077.

[El-02] A. M. El-Aziz. "Influence of steps on the electrochemical oxidation of CO adlayers on Pd(111) and on Pd films electrodeposited on Au(111)". In: *Journal of Electroanalytical Chemistry* 534 (2002), pp. 107–114.

[Elg+18] N. Elgrishi et al. "A Practical Beginner's Guide to Cyclic Voltammetry". In: *Journal of Chemical Education* 95 (2018), pp. 197–206.

[FC21] Z. Fang and W. Chen. "Recent advances in formic acid electro-oxidation: from the fundamental mechanism to electrocatalysts". In: *Nanoscale Advances* 3 (2021), pp. 94–105.

[Fes+18] Jakob Fester et al. "The Structure of the Cobalt Oxide/Au Catalyst Interface in Electrochemical Water Splitting". In: *Angewandte Chemie International Edition* 57.37 (2023/02/08 2018), pp. 11893–11897. DOI: https://doi.org/10.1002/anie.201804417. URL: https://doi.org/10.1002/anie.201804417.

[Fru33] A. Frumkin. "Wasserstoffueberspannung und Struktur der Doppelschicht". In: *Zeitschrift fuer Physikalische Chemie A* 164.1 (1933), pp. 121–133.

[Gao+15] Dunfeng Gao et al. "Size-Dependent Electrocatalytic Reduction of CO2 over Pd Nanoparticles". In: *Journal of the American Chemical Society* 137.13 (Apr. 2015), pp. 4288–4291. DOI: 10.1021/jacs.5b00046. URL: https://doi.org/10.1021/jacs.5b00046.

[Gao+18] Dunfeng Gao et al. "Pd-Containing Nanostructures for Electrochemical CO2 Reduction Reaction". In: *ACS Catalysis* 8.2 (Feb. 2018), pp. 1510–1519. DOI: 10.1021/acscatal.7b03612. URL: https://doi.org/10.1021/acscatal.7b03612.

[Gar+07] Elizabeth Garfias-Garcia et al. "Kinetics Mechanism of Copper UPD Nucleation and Growth on Mono and Polycrystaline Gold". In: *Journal of the Electrochemical Society* 3.34 (2007), pp. 35–43. DOI: 10.1149/1.2795610. URL: http://dx.doi.org/10.1149/1.2795610.

[Gas+01] Maria L. Gaspar et al. "Fluorescein Diacetate Hydrolysis as a Measure of Fungal Biomass in Soil". In: *Current Microbiology* 42.5 (2001), pp. 339–344. DOI: 10.1007/s002840010226. URL: https://doi.org/10.1007/s002840010226.

[GAS13] E. D. German, H. Abir, and M. Sheintuch. "A tunnel model for activated hydrogen dissociation on metal surfaces". In: *Journal of Physical Chemistry C* 117 (2013), pp. 7475–7486.

[GC98] M. R. Gennero de Chialvo and A. C. Chialvo. "Kinetics of hydrogen evolution reaction with Frumkin adsorption: re-examination of the Volmer-Heyrowski and Volmer-Tafel routes". In: *Electrochimica Acta* 44 (1998), pp. 841–851.

[GGM06] N. Gupta, M. Gattrell, and B. MacDougall. "Calculation for the cathode surface concentrations in the electrochemical reduction of CO2 in KHCO3 solutions". In: *Journal of Applied Electrochemistry* 36.2 (2006), pp. 161–172. DOI: 10.1007/s10800-005-9058-y. URL: https://doi.org/10.1007/s10800-005-9058-y.

[Gio+02] J. B. Giorgi et al. "Study on CO adsorption on crystalline silica supported palladium particles". In: *Surface Science* 48 (2002), pp. 71–77.

[GK21] Akansha Goyal and Marc T. M. Koper. "The Interrelated Effect of Cations and Electrolyte pH on the Hydrogen Evolution Reaction on Gold Electrodes in Alkaline Media". In: *Angewandte Chemie International Edition* 60.24 (2023/03/09 2021), pp. 13452–13462. DOI: https://doi.org/10.1002/anie.202102803. URL: https://doi.org/10.1002/anie.202102803.

[GMR95] Hubert A Gasteiger, Nenad M Markovic, and Philip N Ross Jr. "Electrooxidation of CO and H2/CO mixtures on a well-characterized Pt3Sn electrode surface". In: *The Journal of Physical Chemistry* 99.22 (1995), pp. 8945–8949.

[GN97] Andrew A. Gewirth and Brian K. Niece. "Electrochemical Applications of in Situ Scanning Probe Microscopy". In: *Chemical Reviews* 97.4 (June 1997), pp. 1129–1162. DOI: 10.1021/cr960067y. URL: https://doi.org/10.1021/cr960067y.

[Gon12] Jinlong Gong. "Structure and Surface Chemistry of Gold-Based Model Catalysts". In: *Chemical Reviews* 112.5 (May 2012), pp. 2987–3054. DOI: 10.1021/cr200041p. URL: https://doi.org/10.1021/cr200041p.

[Goy+20] Akansha Goyal et al. "Competition between CO2 Reduction and Hydrogen Evolution on a Gold Electrode under Well-Defined Mass Transport Conditions". In: *Journal of the American Chemical Society* 142.9 (Mar. 2020), pp. 4154–4161. DOI: 10.1021/jacs.9b10061. URL: https://doi.org/10.1021/jacs.9b10061.

[Gro+11] V. Grozovski et al. "Adsorption of Formate and Its Role as Intermediate in Formic Acid Oxidation on Platinum Electrodes". In: *ChemPhysChem* 12 (2011), pp. 1641–1644.

[Guo+17] R.-H. Guo et al. "Electrochemical behavior of CO2 reduction on palladium nanoparticles: Dependence of adsorbed CO on electrode potential". In: *Electrochemistry Communications* 80 (2017), pp. 24–28.

[GW91] H.-J. Guentherodt and R. Wiesendanger. *Scanning Tunneling Microscopy I-III*. Springer, 1991.

[Ham+90] Antoinette Hamelin et al. "Cyclic voltammetric characterization of oriented monocrystalline gold surfaces in aqueous alkaline solution". In: *Journal of Electroanalytical Chemistry and Interfacial Electrochemistry* 295.1 (1990), pp. 291–300. ISSN: 0022-0728. DOI: https://doi.org/10.1016/0022-0728(90)85023-X. URL: https://www.sciencedirect.com/science/article/pii/002207289085023X.

[Hay+00] N. Hayazawa et al. "Metallized tip amplification of near-field Raman scattering". In: *Optics Communications* 183 (2000), p. 333.

[Hay01] S. Hayashi. *Spectroscopy of gap modes in metal particle - surfac systems in Near-field optics and surface plasmon polaritons*. Springer, 2001.

[HB07] Fernando Hernandez and Helmut Baltruschat. "Hydrogen evolution and Cu UPD at stepped gold single crystals modified with Pd". In: *Journal of Solid State Electrochemistry* 11.7 (2007), pp. 877–885. DOI: 10.1007/s10008-007-0308-2. URL: https://doi.org/10.1007/s10008-007-0308-2.

[HBA01] E Herrero, L J Buller, and H D Abruña. "Underpotential deposition at single crystal surfaces of Au, Pt, Ag and other materials." eng. In: *Chem Rev* 101.7 (2001), pp. 1897–1930. DOI: 10.1021/cr9600363.

[HCS58] J. P. Hoare, G. W. Castellan, and S. Schuldiner. "Poten- tials of Noble Metal and Palladium Alloy Hydrogen Electrodes". In: *Journal of Physical Chemistry* 62 (1958), pp. 1141–1142.

[Her+99] Enrique Herrero et al. "X-ray and electrochemical studies of Cu upd on single crystal electrodes in the presence of bromide: comparison between Au(111) and Pt(111) electrodes1Dedicated to Professor W. Vielstich on the occasion of his 75th birthday.1". In: *Journal of Electroanalytical Chemistry* 461.1 (1999), pp. 121–130. DOI: https://doi.org/10.1016/S0022-0728(98)00066-7. URL: https://www.sciencedirect.com/science/article/pii/S0022072898000667.

[HF18] E. Herrero and J. M. Feliu. "Understanding the formic acid oxidation mechanism on platinum single crystal electrodes". In: *Current Opinion in Electrochemistry* 9 (2018), pp. 145–150.

[HHI91] Toshinori Hachiya, Hidetoshi Honbo, and Kingo Itaya. "Detailed underpotential deposition of copper on gold(III) in aqueous solutions". In: *Journal of Electroanalytical Chemistry and Interfacial Electrochemistry* 315.1 (1991), pp. 275–291.

[HMB95] J. Hotlos, O. M. Magnussen, and R. J. Behm. "Effect of trace amounts of Cl-in Cu underpotential deposition on Au(111) in perchlorate solutions: an in-situ scanning tunneling microscopy study". In: *Surface Science* 335 (1995), pp. 129–144. DOI: https://doi.org/10.1016/0039-6028(95)00566-8. URL: https://www.sciencedirect.com/science/article/pii/0039602895005668.

[Hof83] F. M. Hoffmann. In: *Surface Science* 107 (1983).

[Hol04] J. M. Hollas. *Modern Spectroscopy*. Wiley, 2004.

[Hor+87] Yoshio Hori et al. "Electrochemical reduction of carbon dioxides to carbon monoxide at a gold electrode in aqueous potassium hydrogen carbonate". In: *J. Chem. Soc. Chem. Commun.* (10 1987), pp. 728–729. DOI: 10.1039/C39870000728. URL: http://dx.doi.org/10.1039/C39870000728.

[Hos+06] N. Hoshi et al. "Structural Effects of Electrochemical Oxidation of Formic Acid on Single Crystal Electrodes of Palladium". In: *Journal of Physical Chemistry B* 110 (2006), pp. 12480–12484.

[HRK94] M. H. Hölzle, U. Retter, and D. M. Kolb. "The kinetics of structural changes in Cu adlayers on Au(111)". In: *Journal of Electroanalytical Chemistry* 371.1 (1994), pp. 101–109. DOI: https://doi.org/10.1016/0022-0728(93)03235-H. URL: https://www.sciencedirect.com/science/article/pii/002207289303235H.

[Hua+15] Teng-Xiang Huang et al. "Tip-enhanced Raman spectroscopy: tip-related issues". In: *Analytical and Bioanalytical Chemistry* 407.27 (2015), pp. 8177–8195. DOI: 10.1007/s00216-015-8968-8. URL: https://doi.org/10.1007/s00216-015-8968-8.

[HW87] Antoinette Hamelin and Michael J. Weaver. "Dependence of the kinetics of proton reduction at gold electrodes on the surface cyrstallographic orientation". In: *Journal of Electroanalytical Chemistry and Interfacial Electrochemistry* 223.1 (1987), pp. 171–184. DOI: https://doi.org/10.1016/0022-0728(87)85258-0. URL: https://www.sciencedirect.com/science/article/pii/0022072887852580.

[HZK95] M.H. Hölzle, V. Zwing, and D.M. Kolb. "The influence of steps on the deposition of Cu onto Au(111)". In: *Electrochimica Acta* 40.10 (1995), pp. 1237–1247. ISSN: 0013-4686. DOI: https://doi.org/10.1016/0013-4686(95)00055-J. URL: https://www.sciencedirect.com/science/article/pii/001346869500055J.

[Ita98] Kingo Itaya. "In situ scanning tunneling microscopy in electrolyte solutions". In: *Progress in Surface Science* 58.3 (1998), pp. 121–247. DOI: https://doi.org/10.1016/S0079-6816(98)00022-7. URL: https://www.sciencedirect.com/science/article/pii/S0079681698000227.

[Jal+06] B. Jalali et al. "Raman-Based Silicon Photonics". In: *IEEE Journal of Selected Topis in Quantum Electronics* 6 (2006), pp. 412–421.

[Joo+13] Jiyong Joo et al. "Importance of Acid–Base Equilibrium in Electrocatalytic Oxidation of Formic Acid on Platinum". In: *Journal of the American Chemical Society* 135.27 (July 2013), pp. 9991–9994.

[Joo+14] Jiyong Joo et al. "The effect of pH on the electrocatalytic oxidation of formic acid/formate on platinum: A mechanistic study by surface-enhanced infrared spectroscopy coupled with cyclic voltammetry". In: *Electrochimica Acta* 129 (2014), pp. 127–136. ISSN: 0013-4686. DOI: https://doi.org/10.1016/j.electacta.2014.02.040. URL: https://www.sciencedirect.com/science/article/pii/S0013468614003429.

[Kas50] Michael Kasha. "Characterization of electronic transitions in complex molecules". In: *Discuss. Faraday Soc.* 9 (0 1950), pp. 14–19. DOI: 10.1039/DF9500900014. URL: http://dx.doi.org/10.1039/DF9500900014.

[KB82] M. Kerker and C. G. Blatchford. "Elastic scattering, absorption, and surface-enhanced Raman scattering by concentric spheres comprised of a metallic and a dielectric region". In: *Physical Review B* 26.8 (Oct. 1982), pp. 4052–4063. DOI: 10.1103/PhysRevB.26.4052. URL: https://link.aps.org/doi/10.1103/PhysRevB.26.4052.

[Kel+20] Sara R. Kelly et al. "Electric Field Effects in Oxygen Reduction Kinetics: Rationalizing pH Dependence at the Pt(111), Au(111), and Au(100) Electrodes". In: *The Journal of Physical Chemistry C* 124.27 (July 2020), pp. 14581–14591. DOI: 10.1021/acs.jpcc.0c02127. URL: https://doi.org/10.1021/acs.jpcc.0c02127.

[Kib+99] L. A. Kibler et al. "Initial stages of Pd deposition on Au(hkl) Part I: Pd on Au(111)". In: *Surface Science* 443.1 (1999), pp. 19–30. DOI: https://doi.org/10.1016/S0039-6028(99)00968-1. URL: https://www.sciencedirect.com/science/article/pii/S0039602899009681.

[KMV15] D. Kurouski, M. Mettei, and R. P. Van Duyne. "Probing redox reactions at the nanoscale with electrochemical tip-enhanced Raman spectroscopy". In: *Nano Letters* 15 (2015), p. 7956.

[KN30] N. Kobozev and N. Nekrasov. In: *Z. Elektrochem.* 36 (1930), p. 529.

[Kor+15] R. Kortlever et al. "Electrochemical CO_2 reduction to formic acid on a Pd-based formic acid oxidation catalyst". In: *Catalysis Today* 244 (2015), pp. 58–62.

[KP22] L. S. Lanka K. Fernando and L. Hasini R. Perera. "Graphical Application to Assist Students Understand the Basic Concepts in Acid–Base Titrations". In: *Journal of Chemical Education* 99.4 (2022), pp. 1547–1552. DOI: 10.1021/acs.jchemed.1c00881. eprint: https://doi.org/10.1021/acs.jchemed.1c00881. URL: https://doi.org/10.1021/acs.jchemed.1c00881.

[Kri+18] Arne S. Kristoffersen et al. "Testing Fluorescence Lifetime Standards using Two-Photon Excitation and Time-Domain Instrumentation: Fluorescein, Quinine Sulfate and Green Fluorescent Protein". In: *Journal of Fluorescence* 28.5 (2018), pp. 1065–1073. DOI: 10.1007/s10895-018-2270-z. URL: https://doi.org/10.1007/s10895-018-2270-z.

[Kur16] D. Kurouski. "Advances of tip-enhanced Raman spectroscopy (TERS) in electrochemistry, biochemistry and surface science". In: *Vibrational Spectroscopy* 91 (2016), p. 3.

[KW09] P. Kl'an and J. Wirz. *Photochemistry of organic compounds : from concepts to practice*. Wiley Blackwell, 2009.

[Lak07] J.R. Lakowicz. *Principles of Fluorescence Spectroscopy*. Springer US, 2007. ISBN: 9780387463124. URL: https://books.google.de/books?id=-PSybuLNxcAC.

[Lar11] P. Larkin. *Infrared and Raman spectroscopy: Principles and spectra interpretation*. Elesevier, 2011.

[Le +20] Florent Le Guern et al. "Fluorescein Derivatives as Fluorescent Probes for pH Monitoring along Recent Biological Applications." In: *Int. J. Mol. Sci.* 21.23 (Dec. 2020).

[LE09] E. C. Le Ru and P. G. Etchegoin. *Principles of surface-enhanced Raman spectroscopy and related plasmonic effects*. Elesevier, 2009.

[Lee+19] Joonhee Lee et al. "Visualizing vibrational normal modes of a single molecule with atomically confined light". In: *Nature* 568.7750 (2019), pp. 78–82. DOI: 10.1038/s41586-019-1059-9. URL: https://doi.org/10.1038/s41586-019-1059-9.

[Lei49] Henry. Leidheiser. "The Importance of Interatomic Spacing in Catalysis. A Correlation between Hydrogen Overvoltage on Metals and the Distance between Atoms". In: *Journal of the American Chemical Society* 71.11 (Nov. 1949), pp. 3634–3636. DOI: 10.1021/ja01179a015. URL: https://doi.org/10.1021/ja01179a015.

[Len+19] Richard van Lent et al. "Site-specific reactivity of molecules with surface defects—the case of H2 dissociation on Pt". In: *Science* 363.6423 (2023/02/08 2019), pp. 155–157. DOI: 10.1126/science.aau6716. URL: https://doi.org/10.1126/science.aau6716.

[Li+13] Ming Fang Li et al. "pH effect on oxygen reduction reaction at Pt(111) electrode". In: *Electrochimica Acta* 110 (2013), pp. 780–789. URL: https://www.sciencedirect.com/science/article/pii/S0013468613007664.

[Li+15] Jian-Feng Li et al. "Dielectric shell isolated and graphene shell isolated nanoparticle enhanced Raman spectroscopies and their applications". In: *Chemical Society reviews* 44 (Oct. 2015). DOI: 10.1039/c5cs00501a.

[Li+16a] Mufan Li et al. "Ultrafine jagged platinum nanowires enable ultrahigh mass activity for the oxygen reduction reaction". In: *Science* 354.6318 (2016), pp. 1414–1419. DOI: 10.1126/science.aaf9050. URL: https://doi.org/10.1126/science.aaf9050.

[Li+16b] Zhensheng Li et al. "Benzimidazole-BODIPY as optical and fluorometric pH sensor". In: *Dyes and Pigments* 128 (2016), pp. 165–169. ISSN: 0143-7208. DOI: https://doi.org/10.1016/j.dyepig.2016.01.029. URL: https://www.sciencedirect.com/science/article/pii/S0143720816300110.

[Lin+01] HJ Lin et al. "Fluorescence lifetime characterization of novel low-pH probes". In: *Analytical biochemistry* 294.2 (July 2001), pp. 118–125. ISSN: 0003-2697. DOI: 10.1006/abio.2001.5155. URL: https://europepmc.org/articles/PMC6906608.

[Liu+15] Xiang Liu et al. "Formic acid: A versatile renewable reagent for green and sustainable chemical synthesis". In: *Chinese Journal of Catalysis* 36.9 (2015), pp. 1461–1475. ISSN: 1872-2067. DOI: https://doi.org/10.1016/S1872-2067(15)60861-0. URL: https://www.sciencedirect.com/science/article/pii/S1872206715608610.

[Liu+86] H. Y. Liu et al. "Scanning electrochemical and tunneling ultramicroelectrode microscope for high resolution examination of electrode surfaces in solution". In: *Journal of the American Chemical Society* 108 (1986).

[LKA10] M. Lukaszewski, T. Kedra, and Czerwinski A. "Hydro- gen electrosorption into Pd-Pt-Au ternary alloys". In: *Electrochimica Acta* 55 (2010), pp. 1150–1159.

[Lon02] D. A. Long. *The Raman effect: A unified treatment of the theory of Raman scattering by molecules*. Wiley, 2002.

[LSC19] Philomena Schlexer Lamoureux, Aayush R. Singh, and Karen Chan. "pH Effects on Hydrogen Evolution and Oxidation over Pt(111): Insights from First-Principles". In: *ACS Catalysis* 9.7 (July 2019), pp. 6194–6201. DOI: 10.1021/acscatal.9b00268. URL: https://doi.org/10.1021/acscatal.9b00268.

[LW73] Joseph R Lakowicz and Gregorio Weber. "Quenching of fluorescence by oxygen. Probe for structural fluctuations in macromolecules". In: *Biochemistry* 12.21 (1973), pp. 4161–4170.

[LW87] L-.W. Leung and M. J. Weaver. "Extending Surface Enhanced Raman Spectroscopy to Transition Metal Surfaces: Carbon Monoxide Adsorption and Electrooxidation on Platinum- and Palladium-Coated Gold Electrodes". In: *Journal of the American Chemical Society* 109 (1987), pp. 5113–5119.

[Mag+90] O. M. Magnussen et al. "Atomic structure of Cu adlayers on Au(100) and Au(111) electrodes observed by in situ scanning tunneling microscopy". In: *Physical Review Letters* 64.24 (June 1990), pp. 2929–2932. DOI: 10.1103/PhysRevLett.64.2929. URL: https://link.aps.org/doi/10.1103/PhysRevLett.64.2929.

[Man68] J. B. Mann. "Atomic Structure Calculations II: Hartree-Fock Wavefunctions and Radial Expectations Values: Hydrogen to Lawrencium". In: *University of California Press* (1968).

[Mar+17] N. Martin Sabanes et al. "Electrochemical TERS elucidates potential-induced molecular reorientation of adenine/Au(111)". In: *Angewandte Chemie Intl.* 56 (2017), p. 9796.

[Mar+95] N. M. Markovic et al. “Electro-oxidation mechanisms of methanol and formic acid on Pt-Ru alloy surfaces”. In: *Electrochimica Acta* 40.1 (1995), pp. 91–98.

[Mar+96] Nenad M Markovića et al. “Hydrogen electrochemistry on platinum low-index single-crystal surfaces in alkaline solution”. In: *Journal of the Chemical Society, Faraday Transactions* 92.20 (1996), pp. 3719–3725.

[Mar18] Aaron T. Marshall. “Using microkinetic models to understand electrocatalytic reactions”. In: *Current Opinion in Electrochemistry* 7 (2018), pp. 75–80. ISSN: 2451-9103. DOI: https://doi.org/10.1016/j.coelec.2017.10.024. URL: https://www.sciencedirect.com/science/article/pii/S2451910317301497.

[Max+12] Rodolfo V. Maximiano et al. “Mechanism of near-field Raman enhancement in two-dimensional systems”. In: *Phys. Rev. B* 85 (23 June 2012), p. 235434. DOI: 10.1103/PhysRevB.85.235434. URL: https://link.aps.org/doi/10.1103/PhysRevB.85.235434.

[May+19] Nolwenn Mayet et al. “Probing the Surface of Noble Metals Electrochemically by Underpotential Deposition of Transition Metals”. In: 2.2 (2019), pp. 257–276. DOI: 10.3390/surfaces2020020.

[Meh+20] Vikram Mehar et al. “Growth and auto-oxidation of Pd on single-layer AgOx/Ag(111)”. In: *Physical Chemistry Chemical Physics* 22.11 (2020), pp. 6202–6209. DOI: 10.1039/C9CP06973A. URL: http://dx.doi.org/10.1039/C9CP06973A.

[Mel+18] Gisele A. B. Mello et al. “Glycerol electrooxidation on Pd modified Au surfaces in alkaline media: Effect of the deposition method”. In: *The Journal of Chemical Physics* 150.4 (2018). DOI: 10.1063/1.5048489. URL: https://doi.org/10.1063/1.5048489.

[MFC17] M. A. H. Mithu, G. Fantoni, and J. Ciampi. “Effect of electrolyte temperature on Faradaic effect in electrochemical microdrilling”. In: *Internation Journal of Prescision Technology* 7.1 (2017), pp. 17–31.

[MH14] Nina Mauser and Achim Hartschuh. “Tip-enhanced near-field optical microscopy”. In: *Chem. Soc. Rev.* 43 (4 2014), pp. 1248–1262. DOI: 10.1039/C3CS60258C. URL: http://dx.doi.org/10.1039/C3CS60258C.

[Mis+16] Hemma Mistry et al. “Nanostructured electrocatalysts with tunable activity and selectivity”. In: *Nature Reviews Materials* 1.4 (2016), p. 16009. DOI: 10.1038/natrevmats.2016.9. URL: https://doi.org/10.1038/natrevmats.2016.9.

[MM10] E. McCafferty and Edward McCafferty. "Thermodynamics of Corrosion: Pourbaix Diagrams". In: *Introduction to Corrosion Science*. New York, NY: Springer New York, 2010, pp. 95–117. ISBN: 978-1-4419-0455-3. DOI: 10.1007/978-1-4419-0455-3{_}6. URL: https://doi.org/10.1007/978-1-4419-0455-3_6.

[Mor+05] M. Morkel et al. "Interpreting intensities in vibrational sum frequency generation (SFG) spectroscopy: CO adsorption on Pd surfaces". In: *Surface Science* 586 (2005), pp. 146–156.

[MXW12] M. F. Mrozek, Y. Xie, and M. J. Weaver. "Surface Enhanced Raman Scattering on Uniform Platinum Group Overlayers: Preparation by Redox Replacement of Underpotial-Deposited Metals on Gold". In: *Analytical Chemistry* 73 (2012), pp. 5953–5960.

[NCL19] T. Noel, Y. Cao, and G. Laudadio. "The Fundamentals Behind the Use of Flow Reactors in Electrochemistry". In: *Accounts of Chemical Research* 52.10 (2019), pp. 2858–2869.

[NH11] L. Novotny and N. van Hulst. "Antennas for light". In: *Nature Photonics* 5 (2011), pp. 83–90.

[OD21] Daniel Ohm and Katrin F. Domke. "Controlled deposition of 2D-confined Pd or Ir nano-islands on Au(111) following Cu UPD, and their HER activity". In: *Journal of Electroanalytical Chemistry* 896 (2021), p. 115285. DOI: https://doi.org/10.1016/j.jelechem.2021.115285. URL: https://www.sciencedirect.com/science/article/pii/S1572665721003118.

[OHa22] Tom O'Haver. *ifilter: Interactive Fourier filter function*. Online: Matlab file exchange. 2022.

[Ohm+23] D. Ohm et al. "Insights into electrochemical catalyst poisoning during formic acid oxidation on 2D confined Palladium nanoislands via electrochemical tip-enhanced Raman spectroscopy". In: *to be submitted* (2023).

[Osa+11] M. Osawa et al. "The Role of Bridge-Bonded Adsorbed Formate in the Electrocatalytic Oxidation of Formic Acid on Platinum". In: *Angewandte Chemie Intl.* 50 (2011), pp. 1159–1163.

[Ovi+16] O. A. Ovideo et al. *Underpotential Deposition - From Fundamentals and Theory to Applications on the Nanoscale*. Springer, 2016.

[Par+20] Jongkyoon Park et al. "Spectral Shifting in Extraordinary Optical Transmission by Polarization-Dependent Surface Plasmon Coupling". In: *Plasmonics* 15.2 (2020), pp. 489–494. DOI: 10.1007/s11468-019-01058-w. URL: https://doi.org/10.1007/s11468-019-01058-w.

[Per+15] J. V. Perales-Rondon et al. "Further insights into the Formic Acid Oxidation Mechanism on Platinum: pH and Anion Adsorption Effects". In: *Electrochimica Acta* 180 (2015), pp. 479–485.

[Pet+05] B. Pettinger et al. "Tip-enhanced Raman spectroscopy (TERS) of malachite green isothiocyanate at Au(111): Bleaching behaviour under the influence of high electromagnetic fields". In: *Journal of Raman Spectroscopy* 36 (2005), p. 541.

[Pet+07] Bruno Pettinger et al. "Direct monitoring of plasmon resonances in a tip-surface gap of varying width". In: *Phys. Rev. B* 76 (11 Sept. 2007), p. 113409. DOI: 10.1103/PhysRevB.76.113409. URL: https://link.aps.org/doi/10.1103/PhysRevB.76.113409.

[Pet+09] Bruno Pettinger et al. "Tip-enhanced Raman scattering: Influence of the tip-surface geometry on optical resonance and enhancement". In: *Surface Science* 603.10 (2009). Special Issue of Surface Science dedicated to Prof. Dr. Dr. h.c. mult. Gerhard Ertl, Nobel-Laureate in Chemistry 2007, pp. 1335–1341. ISSN: 0039-6028. DOI: https://doi.org/10.1016/j.susc.2008.08.033. URL: https://www.sciencedirect.com/science/article/pii/S0039602809000648.

[Pet+19] D. V. Petrov et al. "Effect of pressure and composition on Raman spectra of CO-H_2-CO_2-CH_4 mixtures". In: *Spectrochimica Acta Part A: Molecular and Biomolecular Spectroscopy* 215 (2019), pp. 363–370.

[Pfi+19] Jonas H. K. Pfisterer et al. "Reactivity mapping of nanoscale defect chemistry under electrochemical reaction conditions". In: *Nature Communications* 10.1 (2019), p. 5702. DOI: 10.1038/s41467-019-13692-3. URL: https://doi.org/10.1038/s41467-019-13692-3.

[Pfi19] Jonas H. K. Pfisterer. "Toward nanoscale reactivity mapping under electrocatalytic reaction conditions : Plasmon-enhanced vibrational spectroscopy of the electrochemical gold oxidation and gold oxide reduction". eng. PhD thesis. Mainz, 2019. DOI: http://doi.org/10.25358/openscience-2351.

[PGB00] Manuel Palomar-Pardave, Ignacio Gonzalez, and Nikola Batina. "New Insights into Evaluation of Kinetic Parameters for Potentiostatic Metal Deposition with Underpotential and Overpotential Deposition Processes". In: *The Journal of Physical Chemistry B* 104.15 (2000), pp. 3545–3555.

[PHF14] Juan V. Perales-Rondon, Enrique Herrero, and Juan M. Feliu. "Effects of the anion adsorption and pH on the formic acid oxidation reaction on Pt(111) electrodes". In: *Electrochimica Acta* 140 (2014), pp. 511–517.

[PLW12] Ilya V. Pobelov, Chen Li, and Thomas Wandlowski. "Electrochemical Scanning Tunneling Microscopy". In: *Encyclopedia of Nanotechnology*. Ed. by Bharat Bhushan. Dordrecht: Springer Netherlands, 2012, pp. 688–702. ISBN: 978-90-481-9751-4. DOI: 10.1007/978-90-481-9751-4{_}46. URL: https://doi.org/10.1007/978-90-481-9751-4_46.

[PS07] Stanislav Pandelov and Ulrich Stimming. "Reactivity of monolayers and nano-islands of palladium on Au(111) with respect to proton reduction". In: *Electrochimica Acta* 52.18 (2007), pp. 5548–5555. DOI: https://doi.org/10.1016/j.electacta.2007.02.043. URL: https://www.sciencedirect.com/science/article/pii/S0013468607002228.

[PT94] Oleg A. Petrii and Galina A. Tsirlina. "Electrocatalytic activity prediction for hydrogen electrode reaction: intuition, art, science". In: *Electrochimica Acta* 39.11 (1994), pp. 1739–1747. DOI: https://doi.org/10.1016/0013-4686(94)85159-X. URL: https://www.sciencedirect.com/science/article/pii/001346869485159X.

[PV88] R. Parsons and T. VanderNoot. "The oxidation of small organic molecules: A survey of recent fuel cell related research". In: *Journal of Electroanalytical Chemistry and Interfacial Electrochemistry* 257.9-45 (1988).

[Rac+18] David Raciti et al. "Local pH Effect in the CO2 Reduction Reaction on High-Surface-Area Copper Electrocatalysts". In: *Journal of The Electrochemical Society* 165.10 (July 2018), F799. DOI: 10.1149/2.0521810jes. URL: https://dx.doi.org/10.1149/2.0521810jes.

[Rak+18] Christoph Rakousky et al. "The stability challenge on the pathway to high-current-density polymer electrolyte membrane water electrolyzers". In: *Electrochimica Acta* 278 (2018), pp. 324–331. DOI: https://doi.org/10.1016/j.electacta.2018.04.154. URL: https://www.sciencedirect.com/science/article/pii/S0013468618309150.

[RB80] R. Rossetti and L. E. Brus. "Time resolved molecular electronic energy transfer into a silver surface". In: *The Journal of Chemical Physics* 73.1 (1980), pp. 572–577. DOI: 10.1063/1.439857. eprint: https://doi.org/10.1063/1.439857. URL: https://doi.org/10.1063/1.439857.

[RB81] G. Ritchie and E. Burstein. "Luminescence of dye molecules adsorbed at a Ag surface". In: *Phys. Rev. B* 24 (8 Oct. 1981), pp. 4843–4846. DOI: 10.1103/PhysRevB.24.4843. URL: https://link.aps.org/doi/10.1103/PhysRevB.24.4843.

[Ric+02] C. Rice et al. "Direct formic acid fuel cells". In: *Journal of Power Sources* 111 (2002), pp. 83–89.

[Ric+03] C. Rice et al. "Catalysts for direct formic acid fuel cells". In: *Journal of Power Sources* 115 (2003), pp. 229–235.

[Ric+17] M. Richard-Lacroix et al. "Mastering high resolution tip-enhanced Raman spectroscopy: Towards a shift of perception". In: *Chemical Society Reviews* 46 (2017), p. 3922.

[Ros+13] Jan Rossmeisl et al. "pH in atomic scale simulations of electrochemical interfaces". In: *Phys. Chem. Chem. Phys.* 15 (25 2013), pp. 10321–10325. DOI: 10.1039/C3CP51083B. URL: http://dx.doi.org/10.1039/C3CP51083B.

[Rot08] G. Rothenberg. *Catalysis: Concepts and Green Applications*. Wiley-VCH, 2008.

[Ryb15] L. Ryba. *3D nanopositioning based on tunneling current sensing and piezoactuation*. 2015.

[Sch+09] T. Schmid et al. "Performing tip-enhanced Raman spectroscopy in liquids". In: *Journal of Raman Spectroscopy* 40 (2009), p. 1392.

[Sha14] Alexander G. Shard. "Detection limits in XPS for more than 6000 binary systems using Al and Mg KαX-rays". In: *Surface and Interface Analysis* 46.3 (2023/03/04 2014), pp. 175–185. DOI: https://doi.org/10.1002/sia.5406. URL: https://doi.org/10.1002/sia.5406.

[SHA93] S. Strbac, A. Hamelin, and R.R. Adzić. "Electrochemical indication of surface reconstruction of (100), (311) and (111) gold faces in alkaline solutions". In: *Journal of Electroanalytical Chemistry* 362.1 (1993). An International Journal Devoted to all Aspects of Electrode Kinetics, Interfacial Structure Properties of Electrolytes, Colloid and Biological Electrochemistry, pp. 47–53. ISSN: 1572-6657. DOI: https://doi.org/10.1016/0022-0728(93)80005-3. URL: https://www.sciencedirect.com/science/article/pii/0022072893800053.

[SHE10] M. Sauer, J. Hofkens, and J. Enderlein. *Handbook of Fluorescence Spectroscopy and Imaging: From Ensemble to Single Molecules*. Wiley, 2010. ISBN: 9783527633524. URL: https://books.google.de/books?id=sfLKgk20JjsC.

[Shi+17] X. Shi et al. "Advances in tip-enhanced near-field Raman microscopy using nanoantennas". In: *Chemical Reviews* 117 (2017), p. 4945.

[Shi+95] Zhichao Shi et al. "Electrochemical and second harmonic generation study of SO2-4 adsorption at the Au(111) electrode". In: *Journal of Electroanalytical Chemistry* 396.1 (1995), pp. 115–124.

[Sin+16] Meenesh R. Singh et al. "Hydrolysis of Electrolyte Cations Enhances the Electrochemical Reduction of CO2 over Ag and Cu". In: *Journal of the American Chemical Society* 138.39 (Oct. 2016), pp. 13006–13012. DOI: 10.1021/jacs.6b07612. URL: https://doi.org/10.1021/jacs.6b07612.

[Smi+12] Milutin Smiljanić et al. "Catalysis of Hydrogen Evolution on Au(111) Modified by Spontaneously Deposited Pd Nanoislands". In: *Electrocatalysis* 3.3 (2012), pp. 369–375. DOI: 10.1007/s12678-012-0093-2. URL: https://doi.org/10.1007/s12678-012-0093-2.

[SNK95] Robert Sjöback, Jan Nygren, and Mikael Kubista. "Absorption and fluorescence properties of fluorescein". In: *Spectrochimica Acta Part A: Molecular and Biomolecular Spectroscopy* 51.6 (1995), pp. L7–L21. ISSN: 1386-1425. DOI: https://doi.org/10.1016/0584-8539(95)01421-P. URL: https://www.sciencedirect.com/science/article/pii/058485399501421P.

[Sol+08] José Solla-Gullón et al. "Surface characterization of platinum electrodes". In: *Phys. Chem. Chem. Phys.* 10 (10 2008), pp. 1359–1373. DOI: 10.1039/B709809J. URL: http://dx.doi.org/10.1039/B709809J.

[SP08] J. Steidtner and B. Pettinger. "Tip-Enhanced Raman Spectroscopy and Microscopy on Single Dye Molecules with 15 nm Resolution". In: *Physical Review Letters* 100 (2008), pp. 2361011–2361014.

[SP18] Shreya Sarkar and Sebastian C. Peter. "An overview on Pd-based electrocatalysts for the hydrogen evolution reaction". In: *Inorganic Chemistry Frontiers* 5.9 (2018), pp. 2060–2080. DOI: 10.1039/C8QI00042E. URL: http://dx.doi.org/10.1039/C8QI00042E.

[Spu+20] P. M. Spurgeon et al. "Fundamentals of Au(111) Surface Dynamics: Coarsening of 2D Au islands". In: *Journal of Physical Chemistry C* 124 (2020), pp. 7492–7499.

[SSZ10] J. Stadler, T. Schmid, and R. Zenobi. "Nanoscale Chemical Imaging Using Top-Illumination Tip-Enhanced Raman Spectroscopy". In: *Nano Letters* 10 (2010), pp. 4514–4520.

[ST] National Institute of Standards and Gaithersburg MD Technology. *NIST X-ray Photoelectron Spectroscopy Database*. Online.

[Sta+78] G. Staikov et al. "Zum nachweis von nukleationseffekten bei der metallionenadsorption". In: *Electrochimica Acta* 23.4 (1978), pp. 305–313. DOI: https://doi.org/10.1016/0013-4686(78)80066-8. URL: https://www.sciencedirect.com/science/article/pii/0013468678800668.

[Sto+00] R. M. Stoeckle et al. "Nanoscale chemical analysis by tip-enhanced Raman spectroscopy". In: *Chemical Physics Letters* 318 (2000), p. 131.

[Str+13] Dusan Strmcnik et al. "Improving the hydrogen oxidation reaction rate by promotion of hydroxyl adsorption". In: *Nature Chemistry* 5.4 (2013), pp. 300–306. DOI: 10.1038/nchem.1574. URL: https://doi.org/10.1038/nchem.1574.

[Str+16] Dusan Strmcnik et al. "Design principles for hydrogen evolution reaction catalyst materials". In: *Nano Energy* 29 (2016), pp. 29–36.

[Tan+05] J. Tang et al. "Pd deposition onto Au(111) electrodes from sulphuric acid solution". In: *Electrochimica Acta* 51.1 (2005), pp. 125–132. DOI: https://doi.org/10.1016/j.electacta.2005.04.009. URL: https://www.sciencedirect.com/science/article/pii/S001346860500366X.

[The+14] Francois-Xavier Theillet et al. "Physicochemical Properties of Cells and Their Effects on Intrinsically Disordered Proteins (IDPs)". In: *Chemical Reviews* 114.13 (2014), pp. 6661–6714.

[TK13] M. R. Tarasevich and O. V. Korchagin. "Electrocatalysis and pH (a review)". In: *Russian Journal of Electrochemistry* 49.7 (2013), pp. 600–618. DOI: 10.1134/S102319351307015X. URL: https://doi.org/10.1134/S102319351307015X.

[Tra72] Sergio Trasatti. "Work function, electronegativity, and electrochemical behaviour of metals: III. Electrolytic hydrogen evolution in acid solutions". In: *Journal of Electroanalytical Chemistry and Interfacial Electrochemistry* 39.1 (1972), pp. 163–184. DOI: https://doi.org/10.1016/S0022-0728(72)80485-6. URL: https://www.sciencedirect.com/science/article/pii/S0022072872804856.

[Tri+02] Amalija V Tripković et al. "Methanol electrooxidation on supported Pt and PtRu catalysts in acid and alkaline solutions". In: *Electrochimica Acta* 47.22-23 (2002), pp. 3707–3714.

[Tue+90] M. Tueshaus et al. "Understanding the structure of high coverage CO adlayers". In: *Applied Physics A* 91 (1990).

[Tue90] M. Tueshaus. "Dissertation". PhD thesis. Freie Universitaet Berlin, 1990.

[UHW98] Hiroyuki Uchida, Masaki Hiei, and Masahiro Watanabe. "Electrochemical quartz crystal microbalance study of copper adatoms on Au(111) electrodes in solutions of perchloric and sulfuric acid". In: *Journal of Electroanalytical Chemistry* 452.1 (1998), pp. 97–106. DOI: https://doi.org/10.1016/S0022-0728(98)00112-0. URL: https://www.sciencedirect.com/science/article/pii/S0022072898001120.

[ULL09] S. Uhm, H. J. Lee, and J. Lee. "Understanding underlying processes in formic acid fuels cells". In: *Phys. Chem. Chem. Phys.* 11 (2009), pp. 9326–9336.

[Van13] P. Vandenabeele. *Practical Raman sprectroscopy - An introduction*. Vol. 1. Wiley, 2013.

[Ven10] A. S. Vengurlekar. "Extraordinary optical transmission through metal films with subwavelength holes and slits". In: 98.8 (2023/03/09/ 2010), pp. 1020–1032. URL: http://www.jstor.org/stable/24111757.

[Vij71] Ashok K. Vijh. "Crystal Structures of the Elements of the Periodic Table and the Mechanisms of Electrolytic Hydrogen Evolution". In: 118.2 (1971), p. 263. DOI: 10.1149/1.2407985. URL: http://dx.doi.org/10.1149/1.2407985.

[Voi15] B. Voigtlaender. *Scanning probe microscopes*. Springer, 2015.

[Wan+18a] F. Wang et al. "Fe_2P as novel efficient catalyst promoter in Pd/C system for formic acid electro-oxidation in fuel cells reaction". In: *Journal of Power Sources* 375 (2018), pp. 37–42.

[Wan+18b] Y.-H. Wang et al. "Probing Interfacial Electronic and Catalytic Properties on Well-Defined Surfaces by Using In Situ Raman Spectroscopy". In: *Angewandte Chemie Intl.* 57.35 (2018), pp. 11257–11261.

[Web+96] M. Weber et al. "Formic Acid Oxidation in a Polymer Electrolyte Fuel Cell: A Real-Time Mass-Spectrometry Study". In: *Journal of the Electrochemical Society* 143.7 (1996).

[Wei+82] D. A. Weitz et al. "Fluorescent lifetimes of molecules on silver-island films". In: *Opt. Lett.* 7.2 (Feb. 1982), pp. 89–91. DOI: 10.1364/OL.7.000089. URL: https://opg.optica.org/ol/abstract.cfm?URI=ol-7-2-89.

[Wes85] J. Wessel. "Surface-enhanced optical microscopy". In: *Journal of the Optical Society of America B* 2 (1985), p. 1538.

[Wol+98] K. Wolter et al. "Infrared study of CO adsorption on alumina supported palladium parti- cles". In: *Surface Science* (1998), pp. 428–432.

[WTS98] D. Woehrle, M. W. Tausch, and W.-D. Stohrer. *Photochemie: Konzepte, Methoden, Experimente*. Wiley-VCH, 1998.

[WXS13] Yingying Wang, Bing Xu, and Wanyi Shen. "Theoretical Study of CO Adsorption on Perfect and Defective Gold Surfaces". In: *Adsorption Science & Technology* 31.9 (2023/03/08 2013), pp. 823–828. DOI: 10.1260/0263-6174.31.9.823. URL: https://doi.org/10.1260/0263-6174.31.9.823.

[XGQ21] M. Xiong, Z. Gao, and Y. Qin. "Spillover in Heterogeneous Catalysis: New Insights and Opportunities". In: *ACS Catalysis* 11 (2021), pp. 3159–3172.

[Xin+18] J. Xin et al. "Bimetallic Ni-Co/SBA-15 catalysts prepared by urea co-precipitation for dry reforming of methane". In: *Applied Catalysis A* 554 (2018), pp. 95–104.

[Xu+04] Hongxing Xu et al. "Unified Treatment of Fluorescence and Raman Scattering Processes near Metal Surfaces". In: *Phys. Rev. Lett.* 93 (24 Dec. 2004), p. 243002. DOI: 10.1103/PhysRevLett.93.243002. URL: https://link.aps.org/doi/10.1103/PhysRevLett.93.243002.

[Yan+18] S.-C. Yang et al. "Synergy between Ceria Oxygen Vacancies and Cu Nanoparticles Faciliates the Catalytic Conversion of CO_2 to CO under Mild Conditions". In: *ACS Catalysis* 8.12 (2018), pp. 12056–12066.

[Yin+20] H Yin et al. "Nanometre-scale spectroscopic visualization of catalytic sites during a hydrogenation reaction on a Pd/Aubimetallic catalyst". In: *Nature Catalysis* 3 (2020), pp. 834–842.

[YP08] X. Yu and P. G. Pickup. "Recent advances in direct formic acid fuel cells (DFAFC)". In: *Journal of Power Sources* 182 (2008), pp. 124–132.

[YP09] X. Yu and P. G. Pickup. "Mechanistic study of the deactivation of carbon supported Pd during formic acid oxidation". In: *Electrochemistry Communications* 11 (2009), pp. 2012–2014.

[Zei+16] C. D. Zeinalipour-Yazdi et al. "CO adsorption over Pd nanoparticles: A general framework for IR simulations on nanoparticles". In: *Surface Science* 646 (2016), pp. 210–220.

[Zei+87] M. S. Zei et al. "The influence of anions on the structure of underpotentially deposited Cu on Au(111): A LEED, RHEED and AES study". In: *Berichte der Bunsengesellschaft für physikalische Chemie* 91.4 (2023/02/08 1987), pp. 349–353. DOI: https://doi.org/10.1002/bbpc.19870910423. URL: https://doi.org/10.1002/bbpc.19870910423.

[Zen+15] Z.-C. Zeng et al. "Electrochemical tip-enhanced Raman spectrsocopy". In: *Journal of the American Chemical Society* 137 (2015), p. 11928.

[Zha+13] R. Zhang et al. "Chemical mapping of a single molecule by plasmon-enhanced Raman scattering". In: *Nature* 498.7452 (2013), pp. 82–86. DOI: 10.1038/nature12151. URL: https://doi.org/10.1038/nature12151.

[Zha+17] Xingkai Zhang et al. "An improved galvanic replacement deposition method for synthesis of compact palladium coatings on copper substrates". In: *Materials Letters* 197 (2017), pp. 75–78. DOI: https://doi.org/10.1016/j.matlet.2017.03.119. URL: https://www.sciencedirect.com/science/article/pii/S0167577X17304615.

[Zha+20] L. Zhang et al. "Selective Hydrogenation over Supported Metal Catalysts: From Nanoparticles to Single Atoms". In: *Chemical Reviews* 120.2 (2020), pp. 683–733.

[Zha20] Z. Zhao. "Catalytic Conversion of Carbon Oxides in Confined Spaces: Status and Prospects". In: *ChemCatChem* 12 (2020), pp. 3960–3981.

[ZL07] Jian Zhang and Joseph R. Lakowicz. "Metal-enhanced fluorescence of an organic fluorophore using gold particles". In: *Opt. Express* 15.5 (Mar. 2007), pp. 2598–2606. DOI: 10.1364/OE.15.002598. URL: https://opg.optica.org/oe/abstract.cfm?URI=oe-15-5-2598.

[Zuo+18] Xia Qing Zuo et al. "pH effect on acetate adsorption at Pt(111) electrode". In: *Electrochemistry Communications* 89 (2018), pp. 6–9. ISSN: 1388-2481. DOI: https://doi.org/10.1016/j.elecom.2018.02.009. URL: https://www.sciencedirect.com/science/article/pii/S1388248118300377.

[ZW93] Y. Zhang and M. J. Weaver. "Application of surface-enhanced Raman spectroscopy to organic electrocatalytic systems: decomposition and electrooxidation of methanol and formic acid on gold and platinum film electrodes". In: *Langmuir* 9 (1993), pp. 1397–1403.

Part VI

Appendix

A

Appendix

A.1 EC-STM images in CO containing electrolyte

During the experiments discussed in chapter 4 we recorded EC-STM images of the Pd/Au(111) catalyst in CO containing electrolyte. An example of the resulting images is shown in figure A.1.

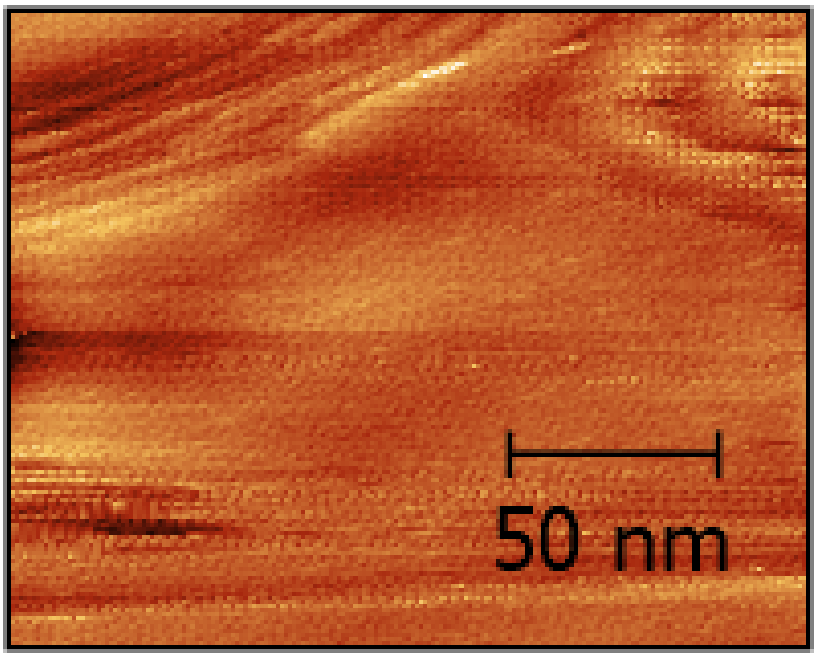

Figure A.1.: EC-STM image of Pd/Au(111) recorded in CO containing electrolyte. Setpoint 0.5 nA, 1.34 lines/s, bias 0.2 V.

The noise in all images acquired in CO containing electrolytes, independent of the time of the experiment, is too high to interpret the image in terms of the topography of the surface.
The same issue occured in trials to record surface maps correlated with TER spectra in CO containing electrolyte to study the 2192 cm^{-1} mode that is discussed in chapter 4.

A.2 Analysis of the fluorescence signal

The measured fluorescence signal during the experiments discussed in chapter 5 of this thesis is obtained as two-dimensional matrix of gray values that represent the fluorescence intensity of each pixel of the sCMOS camera. An example of such a matrix is represented as image in figure A.2.

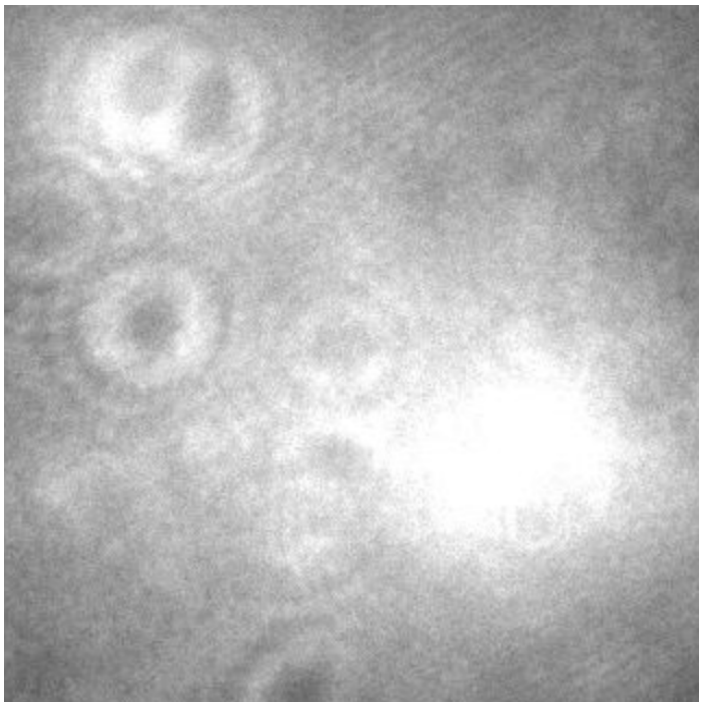

Figure A.2.: Representation of the two-dimensional matrix of fluorescence intensities corresponding to the pixels of the sCMOS camera as obtained during a EC-FM measurement.

The mean of the pixel intensities of each image of a time series of images, recorded at varying electrode potential is calculated and results in a fluorescence intensity vs time plot, that is shown as an example in figure A.3.

The signal of the fluorescence shows spikes that are arbitrary signals as result of the light of monitors reaching the objective during the experiment. These spikes are removed prior to further data processing. The outliers are automatically detected and removed by calculating the deviation from a moving mean of a specific width, here a width of 20 datapoints with the use of a built-in function of Matlab software. Figure A.4 show the original data with marked outliers in red (a) and the data with removed outliers (b).

After the outliers are removed from the data, the background signal is subtracted by applying an asymmetric least square baseline fit to the data and subtracting it. Figure A.5a shows the data with background (black) and the fitted baseline (red). Figure A.5b shows the dataset after background subtraction.

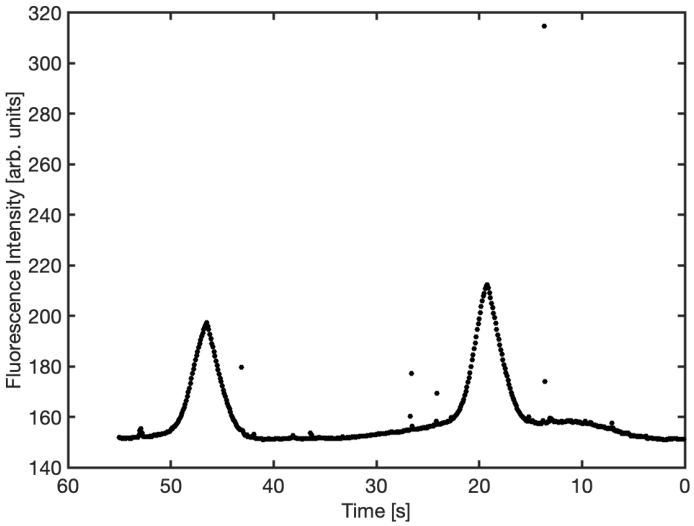

Figure A.3.: Fluorescence intensity as a function of time during 2 potential cycles in a CV measurement.

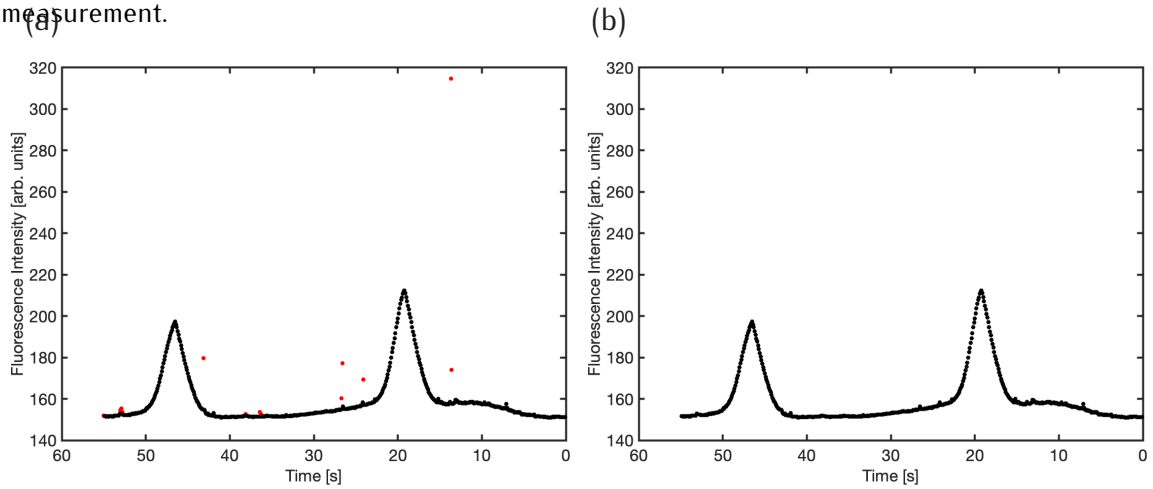

Figure A.4.: (a) Raw fluorescence time series without correction for outliers marked in red in the fluorescence signal. (b) Same dataset without the outliers.

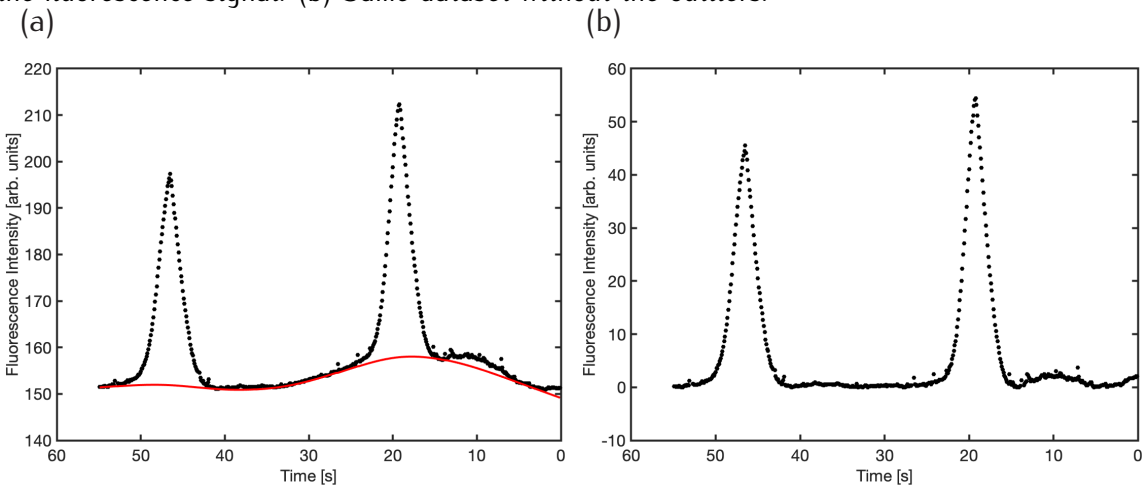

Figure A.5.: (a) Fluorescence signal with background signal (black) and the fitted baseline (red). (b) Same dataset with subtracted background signal.

Part VII

Acknowledgements

B

Acknowledgements

Part VIII

Resume